

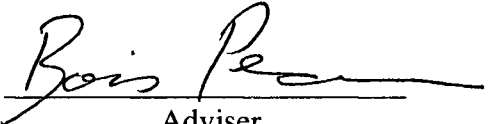
ORIGINAL ARCHIVAL COPY

**CARRIER PHASE GPS AUGMENTATION USING LASER SCANNERS
AND USING LOW EARTH ORBITING SATELLITES**

BY

MATHIEU JOERGER

Submitted in partial fulfillment of the
requirements for the degree of
Doctor of Philosophy in Mechanical and Aerospace Engineering
in the Graduate College of the
Illinois Institute of Technology

Approved 
Adviser

Chicago, Illinois
May 2009

UMI Number: 3370898

Copyright 2009 by
Joerger, Mathieu

INFORMATION TO USERS

The quality of this reproduction is dependent upon the quality of the copy submitted. Broken or indistinct print, colored or poor quality illustrations and photographs, print bleed-through, substandard margins, and improper alignment can adversely affect reproduction.

In the unlikely event that the author did not send a complete manuscript and there are missing pages, these will be noted. Also, if unauthorized copyright material had to be removed, a note will indicate the deletion.

UMI[®]

UMI Microform 3370898
Copyright 2009 by ProQuest LLC
All rights reserved. This microform edition is protected against
unauthorized copying under Title 17, United States Code.

ProQuest LLC
789 East Eisenhower Parkway
P.O. Box 1346
Ann Arbor, MI 48106-1346

© Copyright by
MATHIEU JOERGER
2009

ACKNOWLEDGMENT

I would like to thank my advisor, Professor Boris Pervan for entrusting me with pursuing this research. Beyond his clear guidance and comprehensive knowledge, I will keep his unwavering and uncompromising care for quality in analysis and writing as an inspiration throughout my career. I would also like to thank my defense and dissertation committee, including Professors Sudhakar Nair, Xiaoping Qian and Geoffrey Williamson. I gratefully acknowledge Professor Frank van Graas from Ohio University for the multiple discussions we had on autonomous robot navigation and on integrity monitoring.

Thanks are due to the Boeing Company for sponsoring the part of this research dedicated to Iridium-Augmented GPS. Special thanks go to Dr. Clark Cohen whose valuable insights provided guidance and understanding of the iGPS navigation system.

I would like to thank all of the Navigation and Guidance Lab students (including Elliot Barlow, Julien Eymard, Steven Langel and Jason Neale) for their friendship and assistance. I would especially like to express my gratitude to Fang C. Chan for sharing his expertise on hardware equipment, Livio Gratton for helping me start out my work on integrity monitors, Moon B. Heo for teaching me the basics of carrier phase measurement processing, Bartosz Kempny for his help in collecting experimental data and Samer Khanafseh who became indispensable for testing the autonomous robot.

To the people in my home country, who never stopped encouraging me (Muller and Weber families, Lithemboys association), I owe a great debt. I would like to thank my parents, Marie-Claire Forster and Fernand Joerger, and my brother, Thomas Joerger, for their wholehearted support. Most importantly, I want to thank Myriam, the woman of my life, for accompanying me through the daily joys and upsets of this adventure.

TABLE OF CONTENTS

	Page
ACKNOWLEDGMENT.....	iii
TABLE OF CONTENTS.....	iv
LIST OF TABLES.....	vii
LIST OF FIGURES.....	viii
ABSTRACT.....	x
 CHAPTER	
1. INTRODUCTION.....	1
1.1 GPS Background, Performance and Applications.....	1
1.2 Seamless GPS/Laser Navigation through GPS-Obstructed Environments.....	5
1.3 Cycle Ambiguity Estimation Using Iridium Satellite Signals.....	9
1.4 Global High-Integrity Carrier Phase Navigation.....	11
1.5 Dissertation Outline and Contributions.....	15
2. CARRIER PHASE GPS POSITIONING AND INTEGRITY MONITORING.....	18
2.1 GPS System Architecture.....	19
2.2 GPS Signal Design.....	23
2.3 GPS Measurement Error Sources.....	27
2.4 Differential GPS (DGPS).....	36
2.5 Integrity Monitoring.....	44
3. MEASUREMENT-LEVEL INTEGRATION OF CARRIER PHASE GPS WITH LASER SCANNER OBSERVATIONS.....	48
3.1 Laser-Based Simultaneous Localization and Mapping.....	48
3.2 Measurement-Level GPS/Laser Integration Algorithm.....	60
3.3 Covariance and Monte-Carlo Analyses.....	67
3.4 Experimental Testing.....	76
3.5 Summary of the GPS/Laser Integration.....	82

4. IGPS SYSTEM DESIGN, MEASUREMENT ERROR AND FAULT MODELS	84
4.1 Envisioned iGPS System Architecture	84
4.2 Nominal Measurement Error Models	93
4.3 Measurement Fault Models.....	105
4.4 Integrity Risk Allocation.....	111
5. IGPS POSITIONING AND FAULT-DETECTION ALGORITHM	118
5.1 iGPS Position and Cycle Ambiguity Estimation Algorithm.....	119
5.2 iGPS RAIM-type Detection Algorithm	126
5.3 Further RAIM-based Derivations: Minimum-Residual Fault and RRAIM.....	130
6. IGPS PERFORMANCE ANALYSIS.....	138
6.1 Framework for the Performance Analysis	139
6.2 Fault-Free Availability Analysis.....	146
6.3 Undetected Single-Satellite Fault Analysis	154
6.4 Complementary RAIM-based Analyses	157
6.5 Combined FF-SSF Availability Sensitivity Analysis	161
7. CONCLUSION.....	169
7.1 Carrier Phase GPS Augmentation Using Laser Scanners.....	169
7.2 Carrier Phase GPS Augmentation Using Low Earth Orbiting Satellites.....	170
7.3 Summary of Achievements.....	171
7.4 Future Work.....	174
7.5 Closing.....	176

APPENDIX

A. ADDED CONDITION FOR THE SEPARATE-STAGE CPDGPS ALGORITHM	177
B. IMPLEMENTATION OF THE FEATURE EXTRACTION AND DATA ASSOCIATION ALGORITHMS	182
C. LINEARIZED LASER MEASUREMENT EQUATIONS	186
D. ADDITIONAL STEPS IN THE DERIVATION OF THE MEASUREMENT DIFFERENCING FILTER	190
E. REDUCED-ORDER WEIGHTED LEAST SQUARES RESIDUAL EQUATION WITH PRIOR KNOWLEDGE.....	193

F. EQUATION OF CHANGE IN CARRIER PHASE MEASUREMENT FOR RRAIM.....	196
G. CURRENT-TIME STATE ESTIMATE ERROR COVARIANCE FOR RRAIM	199
BIBLIOGRAPHY	202

LIST OF TABLES

Table		Page
2.1.	Equations for the Cycle Ambiguity Estimation Process [Per97].....	39
2.2.	Equations for the Positioning Process.....	40
3.1.	Sensitivity Analysis: Cross-track Deviation Results (1 sigma, in m).....	71
4.1.	Summary of Error Parameter Values.....	105
4.2.	Fault Mode Inventory (Page 1 of 3).....	106
6.1.	Summary of Requirements	143
6.2.	Summary of Nominal Simulation Parameters	144

LIST OF FIGURES

Figure	Page
2.1. Nominal 24 GPS Satellite Constellation.....	20
2.2. Satellite Measurement Error Sources.....	28
2.3. Satellite Orbit Ephemeris and Clock Errors Over a 24hour Period.....	29
2.4. Ionospheric Error over a 24hour Period.....	31
2.5. Multipath and Receiver Noise	34
2.6. Carrier Phase Sample Autocorrelation Function	35
2.7. Overview of the WAAS Infrastructure and Ionospheric Corrections.....	43
3.1. Three-Stage SLAM Process Included in the GPS/Laser Integration Scheme.....	50
3.2. Laser Scanner Description	51
3.3. Feature Extraction Process.....	53
3.4. Raw Laser Scan Superimposed with a Satellite Picture of the Alley	53
3.5. Consequence of a Miss-Association in the Position-Domain Approach....	55
3.6. Vehicle and Landmark Model	56
3.7. Four-Step Covariance Analysis	59
3.8. Experimental Setup and Artificial Satellite Blockage Models	68
3.9. Direct Simulation of the GPS/Laser Algorithm in the ‘Forest Scenario’ ...	69
3.10. Performance Versus Length of the GPS-Outage	73
3.11. Comparison of Three Implementations for the Street Scenario.....	75
3.12. Experimental Result for the Forest Scenario	78
3.13. Experimental Result for the Miss-Association-Free Urban Canyon Scenario.....	79
3.14. Experimental Setup for the Testing in the Streets of Chicago.....	80

3.15.	Experimental Results for Tests Conducted in the Streets of Chicago	81
4.1.	Iridium Satellite Coverage	86
4.2.	Joint GPS and Iridium Constellations.....	88
4.3.	Conceptual Overview of the Assumed iGPS Architecture	90
4.4.	Iridium and GPS IPPs in an ECSF Frame over 10min	91
4.5.	Three Assumptions for the Ionospheric Error Model	97
4.6.	IPP Displacement.....	98
4.7.	Simplified Schematic of User and Ground Measurement Error Sources ...	113
4.8.	Preliminary Integrity Allocation Tree for Standalone RAIM.....	115
5.1.	Time Variables used in the Algorithms	120
5.2.	Failure Mode Plot	129
6.1.	Final Approach Simulation Description (Case ‘Standard’ in Figure 6.3) ..	140
6.2.	Determination of T_{AV}	145
6.3.	Fault-Free Availability Analysis.....	150
6.4.	Influence of Code Phase Measurements	154
6.5.	Worst Ramp-Type Fault and Minimum Residual Fault	157
6.6.	Impact of Ground Monitoring.....	160
6.7.	Performance Sensitivity to Measurement Error Model Parameters	163
6.8.	Combined FF-SSF Availability Maps for the Nominal Configuration	164
6.9.	Sensitivity to System Configurations (Longitude = -80deg).....	165
6.10.	Availability Sensitivity to Filtering Period and Ionospheric Corrections...	167
A.1	Comparison Between KF updates, WLS estimates, and System Using a GMP.....	181

ABSTRACT

Carrier phase measurements from the Global Positioning System (GPS) can potentially provide centimeter-level ranging accuracy for high-performance navigation. Unfortunately, positioning with carrier phase is only robustly achievable in open sky areas, within limited distance of another GPS receiver, and after substantial initialization time to estimate unknown cycle ambiguity biases. In response, in this research, two ranging augmentation systems are investigated to improve the availability of carrier phase positioning. First, GPS is integrated with laser scanners for precision navigation through GPS-obstructed environments. Second, GPS is augmented with carrier phase measurements from low-earth-orbit (LEO) Iridium telecommunication satellites for global high-integrity positioning.

In the first part of this work, carrier phase GPS and laser scanner measurements are combined for ground vehicle navigation in environments, such as forests and urban canyons, where GPS satellite signals can be blocked. Laser observations of nearby trees and buildings are available when GPS signals are not, and these obstacles serve as landmarks for laser-based navigation. Non-linear laser observations are integrated with time-correlated GPS signals in a measurement-differencing extended Kalman filter. The new navigation algorithm performs cycle ambiguity estimation and provides absolute vehicle positioning throughout GPS outages, without prior knowledge of surrounding landmark locations. Covariance analysis, Monte Carlo simulation, and experimental testing in Chicago city streets demonstrate that the integrated system not only achieves sub-meter precision over extended GPS-obstructed areas, but also improves the robustness of laser-based Simultaneous Localization and Mapping (SLAM).

The second augmentation system, named iGPS, combines carrier phase measurements from GPS and LEO Iridium telecommunication satellites. The addition of fast-moving Iridium satellites guarantees both large satellite geometry variations and signal redundancy, which enables rapid cycle ambiguity estimation and fault-detection using Receiver Autonomous Integrity Monitoring (RAIM). In this work, parametric models are defined for iGPS measurement error sources, and a new fixed-interval estimation algorithm is developed. The underlying observability mechanisms are investigated, and fault-free navigation performance is quantified by covariance analysis. In addition, a carrier phase RAIM detection method is introduced and quantitatively evaluated against known fault modes and theoretical worst-case faults. Performance sensitivity analysis explores the potential of iGPS to satisfy aircraft navigation integrity requirements globally.

CHAPTER 1

INTRODUCTION

The potential of carrier phase measurements from the Global Positioning System (GPS) to provide centimeter-level ranging precision makes it a strong candidate technology for high-accuracy and high-integrity navigation applications. Unfortunately, carrier phase-based positioning is not instantaneous, and can not be performed everywhere. It is only robustly achievable in open sky areas, within limited distance of another GPS receiver (most often, a differential reference station) and after substantial initialization time necessary to estimate unknown cycle ambiguity biases.

In this research, two ranging augmentation systems are devised to extend the availability of accurate carrier phase position fixes. First, GPS signals are integrated with laser scanner observations for seamless ground vehicle precision navigation through natural GPS-obstructed environments. Second, GPS is augmented with carrier phase measurements from fast moving low earth orbit (LEO) Iridium telecommunication satellites for rapid cycle ambiguity estimation. The combination of GPS and Iridium signals further opens the possibility for real-time, high-integrity carrier phase positioning and fault-detection over continental areas.

1.1 GPS Background, Performance and Applications

In less than two decades, GPS has established itself as the single most efficient and ubiquitous civilian navigation utility. It is currently serving a wide spectrum of applications, ranging from popular real-time automotive guidance systems to geodetic surveying of the slow, millimeter-level motion of tectonic plates. The universal interest

in GPS is best illustrated with an overview of emerging Global Navigation Satellite Systems (GNSS) and of satellite-based navigation technologies currently under development.

1.1.1 Historical Perspective on GNSS. Observations from the fast-moving LEO spacecraft Sputnik were at the origin of the first satellite radio-navigation system, the Navy Navigation Satellite System, more commonly known as Transit, which became operational in 1964 [Gui98]. The Transit constellation was comprised of 4-7 LEO space vehicles (SVs) in nearly circular, polar orbits, which broadcasted radiofrequency signals with encoded orbital parameters and time corrections. Users could determine their position by tracking the apparent compression and stretching of the carrier wavelength due to spacecraft motion over 10-20min passes. Each location in sight of the satellite observed a unique Doppler shift curve (defined as the time history of the difference between signal frequencies at the transmitter and at the receiver). As a result, Doppler-based position fixes were achievable several times a day (at 100min intervals at mid-latitudes) with better than 70 meters of accuracy, which met the requirements originally intended for slow moving military vessels and submarines [Dan98]. It was often used in conjunction with inertial navigation systems (INS), which were employed to correct for the added uncertainty due to user motion and to bridge gaps between infrequent position updates.

In the 1990s, Transit was superseded in both military and civilian applications by GPS, which directly utilizes range instead of range rate. Codes modulated on GPS signals provide instantaneous and absolute measurement of the travel time between

satellite transmitter and user receiver. In addition, the GPS medium-earth-orbit (MEO) constellation ensures that at least four SVs are continuously visible anywhere on earth. This enables real-time determination by trilateration of the user's receiver clock deviation and three-dimensional position within about 10m of accuracy [SPS01] [NST99]. In parallel, the Soviet Union developed the Global Navigation Satellite System (GLONASS), currently operated by Russia, but it has not always been fully operational.

More recently, regional augmentation systems have been devised throughout the world in the United States, Europe, Japan and India. They provide corrections for GPS measurement error sources, additional ranging signals from geostationary (GEO) satellites, and integrity information (i.e., measures of the data's trustworthiness). The Wide Area Augmentation System (WAAS) has been operational since 2003 and produces a 95% positioning accuracy better than 5m for single-frequency code-phase GPS users across the United States [NST03]. Regional satellite navigation systems are also being developed in Japan, China and India.

In the near future, GPS modernization efforts (detailed in Chapter 2) will produce increased positioning and timing performance [vDi05] [Mis06]. Within the next decade, Europe is planning to have an independent, fully operational GNSS named Galileo. It is designed for interoperability with both GPS and GLONASS, which is expected to generate unprecedented levels of navigation integrity [Pul04]. Finally, the Compass program aims at extending China's regional satellite navigation system to a global system.

1.1.2 Carrier Phase GPS Positioning Performance and Applications. GPS was originally designed for standalone (i.e., non-differential) receivers using code phase

observations, but the ultimate positioning performance is obtained using carrier phase differential GPS (CPDGPS). Indeed, differential GPS measurements between the user and a nearby reference station are free of spatially-correlated atmospheric disturbances and shared satellite errors, which cause most of the uncertainty in GPS signals. Also, the carrier phase tracking error is lower than the code's by two to three orders of magnitude; however, it requires that an unknown constant cycle ambiguity be determined (receivers can only track the carrier phase modulus 2π) [Mis06]. If these integer cycle ambiguities are correctly resolved, centimeter-level positioning accuracy is achievable.

CPDGPS performance is particularly beneficial for precision navigation applications involving outdoor autonomous ground vehicles (AGVs). AGVs can support missions that are unsafe or too difficult for human operation. In 1997, O'Connor [OCo97] and Bell [Bel00], set the path for the development and expansion of GPS-based automated vehicle navigation and control techniques in practical applications. They successfully realized the automated control of a tractor for unmanned agricultural field plowing. Since then, in less than a decade, precision-controlled AGVs have been successfully implemented in outdoor applications such as grooming of ski runs [Ops00], surveillance missions [Hir04] or intelligent traffic management [Far03]. More recently, the multiple successes at the "DARPA Grand Challenge" [Thr06] (a several-kilometer-long race between fully automated vehicles in natural and urban environments) have placed AGV navigation in the forefront and further widened the scope of their potential applications.

Air transportation may also benefit from the precision of carrier phase measurements. In civilian aviation, it is customary to consider performance metrics other

than accuracy, namely integrity, continuity and availability. For life-critical applications, integrity is of the utmost importance, meaning that the navigation system must be protected against rare-event faults such as satellite failures and unusual atmospheric phenomena. In this context, carrier phase-based fault-detection algorithms [Per96] ensure the highest levels of integrity by allowing for extremely low detection thresholds while maximizing continuity and availability. In the early 1990's, CPDGPS-based navigation systems have been successfully tested for automatic landing of aircraft [Pai93] [vGr93] [Coh95]. Since then, they have been employed in a variety of related applications including shipboard landing of aircraft [Heo04], and autonomous airborne refueling [Kha08].

1.2 Seamless GPS/Laser Navigation through GPS-Obstructed Environments

GPS operates at extremely low power levels (below the background radiofrequency noise), so that satellite signals can be significantly attenuated or blocked by buildings, trees, and rugged terrain. In response in this work, carrier phase GPS and laser scanner measurements are combined for AGV navigation in unstructured outdoor environments such as forests or urban canyons. Laser observations to nearby obstacles are available when GPS is not, and provide in addition, a means for obstacle detection.

1.2.1 Laser-Based Navigation and Sensor Integration. Over the past 30 years, a variety of non-contact ranging sensors have been developed for obstacle detection in robotic applications. Sonar is the most affordable and probably the most widely implemented technology [Leo92] [Thr03]. It is usually preferred for indoor use because

it is limited in range (no more than a few meters) and is severely affected by dust, fog and rain. Cameras and stereo-vision equipment make use of colors and brightness [Bay05], but changing outdoor lighting and atmospheric conditions in unstructured natural environments require extensive image processing and calibration. On the other hand, millimeter wave radars (operating in the 30-80GHz frequency band) operate in harsh visibility conditions [Foe99] (including darkness and fog) and their larger-than-100m range is adequate for outdoor applications [Dis01]. Laser scanners (or laser radars) produced within the past ten years provide similar performance at a lower price, with sub-decimeter ranging accuracy and update rates of 5Hz or more [SIC06]. Emerging technologies include three-dimensional laser scanners, but they have lower update rates and are more expensive. Alternatively, laser cameras output ranging measurements for arrays of pixels targeting obstacles within a limited field of vision [Cam06].

The idea of position estimation relative to static obstacles used as landmarks was formalized in the late 1980's for autonomous vehicle navigation with the Simultaneous Localization and Mapping (SLAM) algorithm [Dis01] or Concurrent Mapping and Localization [Leo00]. SLAM provides vehicle positioning using previously unknown features in the environment. Originally designed for indoor applications, SLAM is typically performed in conjunction with dead-reckoning sensors such as INS, encoders or magnetometers (e.g., [Dis01] [Mad02] [Bay05]).

Few implementations use both SLAM and GPS, and only in loosely integrated approaches (in the position domain) [Kim04]. In contrast, there is no shortage of publications describing inertial navigation instruments as a way to bridge gaps in GPS satellite availability (e.g., [Far03] [Gre96]). Interestingly, inertial sensors drift over time

whereas SLAM-based positioning error increases with distance – as earlier landmarks get out of the sensor’s range and new landmarks come in sight. Ranging source devices such as lasers can maintain sub-meter accuracy over several hundreds of meters, which, at land-vehicle speeds, is rarely the case even for tactical grade INS. Occasional absolute GPS updates can then be used to correct the laser-based positioning drift.

Alternative solutions to the non-linear laser-based SLAM problem include Extended Kalman Filter (EKF)-based algorithms [Thr03] which can be performed iteratively for real-time operations. In practice, two intermediary procedures are carried out to select the few raw laser measurements originating from consistently identifiable landmarks (feature extraction) and to assign them to the corresponding landmark states in the EKF (data association). Integration with absolute GPS measurements will provide much needed robustness for successful implementation of these procedures.

1.2.2 Measurement-Level Integration of CPDGPS and Laser Measurements. An intuitive way to determine the user’s location based on CPDGPS and laser scanner information is simply to combine the individual positioning outputs of each sensor. However in partially obstructed GPS environments, such as urban canyons and forest roads, there are often less than four satellite signals available, which with this position-domain approach are left unused (four SVs are normally required to solve for the three-dimensional position and receiver clock deviation). In contrast, integration at the measurement level (also referred to as range-domain integration) makes use of these few satellite signals with clear lines of sight by utilizing additional laser observations.

GPS carrier phase cycle ambiguities can take several tens of minutes of filtering to be reliably estimated. Their resolution is generally treated as an initialization step (for geodesy and surveying [Rem90]) or as a separate procedure from actual instantaneous positioning (for dynamic applications such as aircraft automatic approach and landing [Hat94] [Law96]). Nevertheless for an AGV passing through GPS obstructions, it is essential that cycle ambiguities be immediately updated with vehicle position, as soon as satellites come back in sight. With laser-based augmentation, the estimator keeps track of the rover's absolute location. Thus, information on carrier phase cycle ambiguities for re-acquired satellites is readily available at the exit of the GPS-denied area, and is automatically exploited in the measurement-level implementation. Although the accuracy of the laser-based position solution is typically insufficient to resolve the cycle ambiguities as specific integers, real-valued (floating) estimates can be efficiently exploited to mitigate further drift in positioning error from that point on.

In this research, the range-domain GPS/laser integration architecture is realized using a unified and compact measurement differencing EKF capable of handling angular and ranging laser observations as well as time-correlated GPS signals. The real-time algorithm simultaneously performs vehicle positioning, landmark mapping, and on-the-fly carrier phase cycle ambiguity estimation. The proposed approach is optimal in that it automatically combines all available information (differential GPS code and carrier, and also laser measurements) to achieve a maximum likelihood state estimation of position and cycle ambiguities.

Performance analyses are structured around two benchmark scenarios: first, a 'forest scenario' where the vehicle roves across a GPS-unavailable area using tree trunks

as landmarks in order to maintain a precise position estimate; second, an ‘urban canyon scenario’ describing the decisive contribution of a few GPS satellites to the integrated system, as compared to a position-domain implementation, which only uses laser measurements to buildings’ edges. Covariance analyses quantify the performance of the state estimator whereas Monte-Carlo simulations expose the added impact of the data extraction and association. Finally, two separate sets of experiments are carried out, first in a structured environment where landmarks are clearly recognizable, and then in the streets of Chicago, which ultimately provides an assessment of the total system performance in a natural environment.

1.3 Cycle Ambiguity Estimation Using Iridium Satellite Signals

Centimeter-level carrier phase positioning is contingent upon correct resolution of cycle ambiguities. The latter remain constant as long as they are continuously tracked by the receiver. A costless yet efficient solution for their estimation is to exploit the bias observability provided by redundant satellite motion (redundancy exists when five or more SVs are visible). Unfortunately, the large amount of time for GPS spacecraft to achieve significant changes in line of sight (LOS) precludes its use in real-time applications that require immediate position fixes.

In contrast, range variations from LEO satellites quickly become substantial. Therefore in a second part of this research, the geometric diversity of GPS ranging sources is enhanced using carrier phase measurements from fast moving Iridium satellites. In fact, carrier phase observations are equal to integrated Doppler shift, so that the underlying concepts of utilizing spacecraft motion to resolve cycle ambiguities and of

Transit's Doppler positioning are equivalent. Combined with GPS, real-time unambiguous carrier-phase based trilateration is possible without restriction on the user's motion.

1.3.1 Related Work. The Integrity Beacon Landing System (IBLS), devised in the early 1990's for aircraft precision approach and landing, was an explicit implementation of the principle of bias estimation using geometric diversity [Coh95] [Per96]. GPS signal transmitters serving as pseudo-satellites ('pseudolites') placed on the ground along the airplane's trajectory provided additional ranging sources and a large geometry change as the receiver's downward-looking antenna flew over the installation. The efficiency of IBLS was demonstrated in 1994 as it enabled 110 successful automatic landings of a Boeing 737 [Coh95]. However, pseudolite placement constraints, maintenance cost and elaborate signal design (to avoid jamming GPS satellite measurements) prevented wider use of the system.

By 2000, Rabinowitz et al. designed a receiver capable of tracking carrier-phase measurements from GPS and from GlobalStar (another LEO telecommunication constellation) [Rab98]. Using GlobalStar satellites' rapid geometry variations, precise cycle ambiguity resolution and positioning was achieved within 5min. Numerous practical issues relative to the synchronization of GPS and GlobalStar data (without modification of the SV payload) had to be overcome to obtain experimental validation results. Such considerations are outside the scope of this thesis, but Rabinowitz's prior work is a compelling proof of concept for the Iridium/GPS system.

1.3.2 Combined GPS and Iridium Satellite Measurements. In this work, carrier-phase ranging measurements from GPS and LEO Iridium satellites are integrated in a high-integrity precision navigation and communication system named iGPS. iGPS opens the possibility for rapid, robust and accurate carrier-phase positioning over wide areas. The resulting system's real-time high-integrity positioning performance makes it a potential navigation solution for demanding precision applications such as autonomous terrestrial and aerial transportation.

Iridium satellites were arranged in near polar orbits for communication purposes. The constellation presents peculiar characteristics when used for navigation. For example, higher SV densities near the poles generate better performance at high latitudes than around the equator. Moreover, the North-South directionality of satellite motion causes heterogeneous horizontal positioning performance at the user location along the local East and North directions. These considerations, as well as augmentation with other spacecraft constellations (e.g., including GlobalStar) are examined as part of this research.

1.4 Global High-Integrity Carrier Phase Navigation

The primary motivation for the addition of fast-moving LEO Iridium spacecraft stems from two core principles: large changes in redundant satellite geometry for rapid cycle ambiguity resolution, and incidentally, satellite redundancy for high-integrity fault-detection. In addition, when designing iGPS for wide area service coverage, the user's proximity to a local differential reference station is no longer guaranteed. Residual measurement errors become significant, especially for single-frequency civilian

applications that are affected by disturbances from the ionosphere, which is the largest source of SV measurement error.

1.4.1 iGPS Measurement Error Models. The treatment of measurement errors plays a central part in the design of the iGPS navigation system. Error sources include uncertainties in satellite clocks and positions, signal propagation delays in the ionosphere and troposphere, user receiver noise and multipath (unwanted signal reflections reaching the user antenna). As mentioned earlier, differential corrections can help mitigate satellite-dependent and spatially-correlated atmospheric errors. In differential GPS, measurements collected at ground reference stations are compared with the known distance between these stations and the satellites. The resulting correction accuracy varies with user-to-ground-station separation distance.

In the GPS/laser integration system as well as in the aforementioned pseudolite and GlobalStar-augmented GPS research, the short baseline-distance from the differential reference station to the user (1-5km) is instrumental in achieving high performance. In Rabinowitz's work in particular, residual measurement errors over short baselines could be modeled reliably enough to allow for integer cycle ambiguities to be fixed.

However, the envisaged iGPS architecture aims at servicing wide-areas with minimal ground infrastructure and therefore relies on long-range corrections similar to the ones generated by WAAS. When using long-range corrections, the unpredictability of atmospheric effects makes it impossible to capture residual errors with high levels of confidence.

Hence a conservative approach is adopted for the derivation of new parametric measurement error models. They account for the instantaneous uncertainty at signal acquisition (absolute measurement error) as well as variations over the signal tracking duration (relative error with respect to initialization). Unlike existing GPS measurement models used in WAAS [MOP01] and in the Local Area Augmentation System (LAAS) [McG00], iGPS error models deal with large drifts in ranging accuracy for LEO satellite signals moving across wide sections of the atmosphere. The models assumptions are based upon a literature review of ionosphere (e.g., [Han00a]) and troposphere-related research [Hua08]. Furthermore, published data on satellite clock and orbit ephemeris errors [War03] as well as preliminary experimental results help establish an initial knowledge of the measurement error probability distributions. They also show that the dynamics of the errors can be reliably modeled over short time periods [Oly02].

1.4.2 iGPS Positioning and Fault-Detection. Thus, two conflicting considerations are shaping the carrier-phase iGPS estimation and detection processes: ranging measurements must be tracked for as long as possible to draw maximum benefit from changes in satellite geometry, but as this filtering duration increases, the robustness of the measurement error model decreases. To circumvent this problem, a fixed-interval filtering algorithm is developed for the simultaneous estimation of user position and floating carrier-phase cycle ambiguities.

In addition, Iridium and GPS code and carrier-phase observations collected within the filtering interval are all vulnerable to rare-event integrity threats such as user equipment and satellite failures. In this regard, the augmentation of GPS with Iridium

offers a decisive advantage in guaranteeing redundant measurements, which enables Receiver Autonomous Integrity Monitoring (RAIM) [Stu88] [Bro92]. Indeed, if five or more satellites are available, the self-consistency of the over-determined position solution is verifiable. The accuracy of carrier-phase observations further allows for an extremely tight detection threshold while still ensuring a very low false-alarm probability [Per96]. To protect the system against faults that may affect successive measurements, a batch residual-based detection method is developed. Complementary RAIM-based analyses include the derivation of ‘worst-case’ faults that minimize the residuals, and of a position-domain relative RAIM (RRAIM) method, which provides an additional level of integrity monitoring relative to previously RAIM-validated position fixes.

Potential applications for iGPS are investigated, including ground and aerial transportation. Target requirements are inspired from the most stringent standards in the civilian aviation community for the benchmark mission of aircraft precision approach. Hence, a 10m vertical alert limit (VAL) at touch-down is specified [MAS04], which is much tighter than what continental-scale navigation systems such as WAAS are currently able to fulfill [MOP01] [NST03]. Since transportation involves safety of lives, special emphasis is placed on integrity: when the aircraft’s pilot has near-zero visibility to the runway, requirements specify that no more than one undetected hazardous navigation system failure is allowed in a billion approaches [MAS04].

Performance evaluations are structured around these requirements. Fault-free (FF) integrity is measured by covariance analysis, and residual-based detection is tested against canonical step and ramp-type single-satellite faults (SSF) of all magnitudes and start-times. The multidimensionality of the algorithm and the multiplicity of system

parameters make the design of the envisioned navigation architecture particularly complicated. A sensitivity analysis is conducted to compare the relative influence of individual system parameters on the overall end-user output. The methodology singles out system components likely to bring about substantial performance improvement and establishes recommendations on possible orientations for future design iterations. Finally, the combined FF and SSF performance evaluation places dominant system parameters in the foreground, investigates alternative system configurations, and assesses the potential of iGPS to provide global high-integrity positioning in the near-term future.

1.5 Dissertation Outline and Contributions

Chapter 2 of this dissertation introduces the basics of GPS, including system design, signal structure, measurement error sources, differential architectures and integrity monitoring. An example CPDGPS algorithm based on separate cycle ambiguity and position estimation processes is described. It is the starting point of this research in terms of carrier phase navigation algorithms, both for the laser and for the Iridium ranging augmentation systems.

Chapter 3 is dedicated to the measurement-level GPS/laser integration, whereas Chapters 4 to 6 present the iGPS navigation system design and analysis. The dissertation was written in such a manner that Chapter 3 and Chapters 4-6 can be read independently from each other while most of their shared references are given in Chapter 2. Closing remarks are given in Chapter 7. The specific contributions associated with this research are discussed in the following subsections.

1.5.1 GPS/Laser Measurement-level Integration. A novel navigation system that integrates carrier phase GPS and laser scanner observations in the measurement domain was designed and analyzed for seamless precision positioning through GPS-obstructed environments. Quantitative performance evaluation of the integrated navigation algorithm was conducted for a benchmark AGV trajectory-tracking problem. (Chapter 3)

1.5.2 Experimental Validation of the GPS/Laser System. Experimental testing of CPDGPS-augmented SLAM procedures was carried out and demonstrated robust feature extraction and data-association, hence enabling precision navigation in realistic forested and urban outdoor environments. (Chapter 3)

1.5.3 iGPS Measurement Errors and Fault Modes. Realistic stochastic models were created and implemented for nominal ionosphere, troposphere, multipath and satellite orbit ephemeris and clock errors, as well as for single-satellite fault modes affecting sequences of satellite measurements over time. In parallel, a conceptual Iridium/GPS navigation system architecture was established, including integrity requirement allocation between system components, for wide-area high-integrity precision positioning in civilian applications. (Chapter 4)

1.5.4 iGPS Position Estimation. A fixed-interval positioning and cycle-ambiguity resolution algorithm was devised based on combined GPS and low-earth-orbit satellite measurements. The underlying estimation and observability mechanisms for Iridium were investigated using covariance analysis results. (Chapters 5 and 6)

1.5.5 iGPS Fault-Detection. A Receiver Autonomous Integrity Monitoring (RAIM) fault-detection method was developed to protect the Iridium-augmented GPS system against single-satellite faults. A relative RAIM algorithm was also derived to provide an additional layer of integrity monitoring. A detailed analysis of undetected fault modes was conducted to identify problematic integrity threats. (Chapters 5 and 6)

1.5.6 iGPS Performance Analysis Methodology. A methodology was defined to analyze and quantify the accuracy, integrity, continuity, and availability of Iridium/GPS positioning solutions under both fault-free and faulted conditions. Sensitivity to navigation system parameters was assessed over continental areas, for various space, ground and user segment architectures. (Chapter 6)

CHAPTER 2

CARRIER PHASE GPS POSITIONING AND INTEGRITY MONITORING

The GPS Standard Positioning Service ensures real-time continuous three-dimensional positioning with approximately 10 meters of accuracy (95% of the time) [NST99]. These estimates are available to an unlimited number of dynamic users located anywhere on earth, with near-zero initialization time. Carrier phase ranging signals combined with differential architectures, sensor integration, and augmentation systems have widened the scope of GPS-based applications so that it is becoming a core technology for outdoor navigation operations that require the highest levels of accuracy, integrity, continuity and availability.

This chapter describes founding principles of GPS with emphasis on material relevant to the dissertation's topics. Section 2.1 outlines the three segments of the GPS system design (space, ground and user segments). Section 2.2 discusses the GPS code and carrier phase measurements, and the navigation message that contains spacecraft position and synchronization information. An overview of the measurement error sources is provided in Section 2.3, with experimental illustrations of their impact on satellite ranging observations. Measurement errors can be efficiently mitigated in differential GPS (DGPS) architectures, which have been developed in a variety of forms as explained in Section 2.4. Finally, Section 2.5 introduces GPS measurement integrity monitoring.

2.1 GPS System Architecture

GPS positioning is based on the concept of trilateration: the user's position is determined using ranging observations from three or more beacons (satellites) at known locations. The distance between satellite transmitter and user receiver is derived from one-way time-of-arrival measurements of ultra-high-frequency radio waves that propagate at the speed of light ($c = 299,792,458\text{m/s}$). This passive architecture, where user receivers are in listen-only mode, requires time-synchronization with satellites. The receiver clock deviation constitutes a fourth unknown that can be solved for if enough satellites are available.

The GPS constellation was therefore designed to provide continuous global coverage by four or more satellites. Spacecraft are monitored by a ground segment, which computes and uplinks satellite positions and clock corrections to the spacecraft, which are then broadcast to user receivers. The space, ground and user segments are described next.

2.1.1 GPS Space Segment. Fundamentals of orbital mechanics provide the basis and terminology for the description of the GPS constellation (and of LEO constellations presented in Chapter 4). In idealized conditions, where the only acting force is the gravitational field of a spherical earth with uniformly distributed mass, the satellite orbit is an ellipse. This ellipse is fixed in an earth-centered inertial frame (whose axes are fixed with respect to the stars), with the center of the earth at one of its foci. In this case, the spacecraft trajectory is fully described by six Keplerian elements (for details, see for

example reference [Bat71]). The specification of the actual GPS orbits is more complex, as will be discussed shortly.

The GPS medium earth orbit constellation ensures that at least four space vehicles (SVs) are visible at anytime, anywhere on earth. A baseline GPS constellation comprises 24 satellites (pictured in Figure 2.1, with dashed lines for LOS at the Chicago location) following near-circular geosynchronous orbits at about 20,000km of altitude [SPS01]. In fact, the orbital period T_{GPS} of one half sidereal day defines the orbit's semi-major axis (from Kepler's second law) and was selected such that SV ground tracks repeat themselves daily, every two revolutions. Satellites are arranged in six equally separated orbital planes, with 55deg inclination angles. Each orbital plane contains four spacecraft, unevenly spaced to minimize loss of accuracy in case of satellite outage. The total number of SVs actually varies between 24 and 30 with the addition of spare satellites (ideally one in each orbital plane).

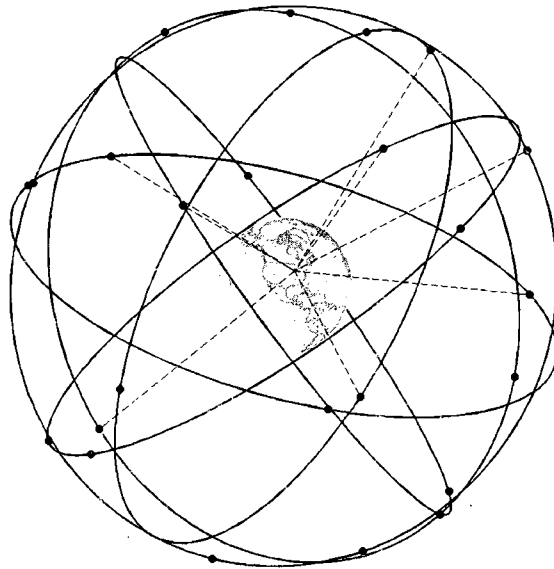


Figure 2.1. Nominal 24 GPS Satellite Constellation

One distinctive feature of GPS satellites is that they are equipped with highly-stable atomic cesium and rubidium clocks (long-term stability on the order of 10^{-13} [Mis06]), which are essential to the system's precise synchronization on a common time-reference for direct transit time measurements.

Another essential characteristic is that satellite positions can be predicted to within a few meters of accuracy, using measurements collected at ground reference stations 24 to 48 hours earlier. In this regard, GPS benefited from decades of research (in part motivated by Transit [Yio98]), which aimed at modeling perturbations from the earth oblateness, from the lunar and solar gravitational fields, and from the pressure of the sun's radiation. A total of 16 parameters based on a modified Kepler model constitute the GPS ephemeris (including six quasi-Keplerian elements at one reference epoch, plus rates of change and sinusoidal correction terms). These ephemeris parameters were also designed to minimize the user receiver's computational load, which was essential at the time they were selected, more than 30 years ago. They are computed by the ground segment.

2.1.2 GPS Ground Control Segment. The GPS ground-based Operational Control Segment (OCS) makes satellite position and time synchronization information available to users. Spacecraft dynamics are modeled using observations from twelve ground monitoring stations spread around the world (six of them were recently added in 2005 so that all SVs are continuously tracked by at least two stations [Mis06]). Orbit ephemeris parameter predictions are computed at a master control station, uploaded to the spacecraft (at least once a day), and broadcast to users as part of the navigation message modulated

on the GPS signal. The twelve monitoring stations are equipped with atomic clocks to establish satellite clock offset, drift, and drift rate corrections also transmitted in the navigation message. Additional functions fulfilled by the OCS include monitoring and maintaining satellite health, and commanding occasional SV station-keeping maneuvers and relocations to compensate for failures.

2.1.3 GPS User Segment. The user segment is composed of all GPS receivers and their antennas. Receivers are typically equipped with low-cost quartz oscillator clocks that are unstable over long durations (10^{-6} - 10^{-9} over a day [Mis06]). The deviation from GPS time (noted τ_k in subsequent equations) introduces a nuisance parameter that can be solved for if four or more satellites are available.

GPS was designed by the US Department of Defense to service both military and civilian users. Civilian users can collect single-frequency L1 (for link 1, centered at f_{L1} , $f_{L1} = 1575.4\text{MHz}$) coarse acquisition (C/A) code and carrier phase ranging observations. Users also have access to the navigation message (described in Section 2.2.3).

The GPS receiver used in the experiments of Chapter 3 is also capable of exploiting measurements at the L2 frequency ($f_{L2} = 1227.6\text{MHz}$). The C/A code is not modulated on L2, but a precision code is, which is encrypted when the GPS anti-spoofing function is turned on (reserved for military purposes). Multiple techniques have been developed to track L2 signals without actually knowing the encrypted precision code; however these operate at the cost of a lower signal-to-noise ratio [Woo99]. In Chapter 3, L2-frequency observations are used to speed up the carrier phase cycle ambiguity estimation process.

GPS modernization is underway. Among other enhancements, including extension of the ground segment, signal structure modifications and improved ephemerides, the modernization plans to provide L1, L2 and L5 ($f_{L5} = 1176\text{MHz}$) signals to civilians within the next 10-15 years [VDi05] [Mis06]. Long-term future implementations of the Iridium-augmented GPS navigation system are simulated in Chapter 6 and consider dual-frequency GPS measurements.

2.2 GPS Signal Design

Despite limitations in satellite broadcast signal power and in frequency bandwidth, the GPS signal design enables data transmission as well as simultaneous ranging from up to 30 identifiable transmitters located more than 20,000km away from the receiver. This section describes advances in communication theory at the origin of such remarkable achievement, and alludes to the issues that motivated this dissertation: absolute carrier phase measurements provide centimeter-level ranging precision but are only available in open-sky areas, and require initialization times that are too long for most real time applications.

2.2.1 Code Phase Measurements. The link between satellite and user can be established because the receiver knows and is expecting the code that is being broadcast. GPS codes are described as binary pseudo-random noise (PRN) codes, which are bit sequences of zeros and ones that appear random but that actually have two main special properties [Mis06].

- *Near-zero cross-correlation:* The codes are said to be orthogonal, and can be recognized from each other. This principle called code division multiple access (CDMA) allows for multiple identifiable signals to be tracked at the same frequency.
- *Peak of zero-offset autocorrelation:* This property is used by the receiver to align its internally generated code with the satellite signal. The measured time offset between generated and received codes provides instantaneous ranging information.

Each one of the 36 C/A codes is a unique sequence of 1023 bits repeated every 1ms (each bit or chip lasts about 1 μ s) and modulated on the carrier using binary phase shift keying: the phase of the carrier is shifted by 180deg if the bit is a one and remains unchanged if the bit is zero. As a result of the modulation, the signal energy is spread over a wide 2MHz frequency band, and the power spectral density is reduced to well below that of the background radiofrequency noise. In fact the signal power received by a user on earth is on the order of 10^{-16} watts for a typical antenna [ICD93].

The GPS codes were designed to be tracked at very low power levels, but obstructions in the satellite LOS such as building walls or foliage are enough to block the signal. In recent years, hyper-sensitive receivers and antennas have been developed to make GPS positioning available indoors [Mit06], with unavoidable deterioration in precision and robustness. The alternative approach to navigate in GPS-denied environments consists in integrating multiple sensors, which is explored in Chapter 3.

Finally, code phase observations are referred to as pseudoranges, because their measure of the true range between a satellite s and the user at epoch k (noted $^s r_k$) is

offset by the receiver clock deviation τ_k and altered by errors ${}^s\mathcal{E}_{\rho,k}$ that are detailed in Section 2.3. The code phase pseudorange equation is expressed as:

$${}^s\rho_k = {}^s r_k + \tau_k + {}^s\mathcal{E}_{\rho,k}.$$

2.2.2 Carrier Phase Measurements. The ultimate in GPS performance is obtained using measurements of the signal's carrier phase. Once the code has been identified, it can be removed from the signal, leaving the carrier, whose tracking error is lower than the code's by two to three orders of magnitude.

The code's 300m chip-length (for a total code length of 300km) makes it easy to determine the correct number of times that the code is entirely repeated between emission and reception (instantaneously if an approximate a priori user position is known to within 100km [Ash88]). Therefore, code is said to provide absolute ranging measurements. In contrast, the much shorter wavelength of the carrier phase ($\lambda_{L1} = c / f_{L1} = 19\text{cm}$ for L1) makes resolution of the unknown integer number of cycles, called cycle ambiguities, one of the major challenges of carrier phase-based positioning.

Cycle ambiguities are constant in time as long as the carrier signals are continuously tracked by the receiver. They become observable when the LOS to redundant satellites changes over time (redundancy is defined when more than four satellites are visible). LOS variations from GPS spacecraft take several tens of minutes to provide significant cycle ambiguity observability. For this reason, the carrier phase navigation system described in Chapters 4 to 6 makes compelling use of fast moving LEO satellite signals to augment GPS.

The highest level of ranging accuracy is achieved when the integer nature of the unknown carrier phase bias can be exploited, in other words, when cycle ambiguities can be fixed. Fixing requires that measurement errors be modeled with high levels of integrity, and is usually restricted to differential architectures (Section 2.4.1) where the reference station is within a few kilometers at most.

Similar to code, the carrier phase observation ${}^s\phi_k$ for a satellite s at epoch k is a measure of the true range ${}^s r_k$ that is offset (by τ_k), noisy (due to carrier measurement noise ${}^s\epsilon_{\phi,k}$) but also biased by the constant cycle ambiguity ${}^s N$. The carrier phase equation, written here in units of meters (in this case, ${}^s N$ is not an integer), is:

$${}^s\phi_k = {}^s r_k + \tau_k + {}^s N + {}^s\epsilon_{\phi,k}.$$

2.2.3 GPS Navigation Message. The navigation message contains the satellite position and synchronization information necessary for users to locate themselves. It is a 50 bit-per-second (bps) stream of data modulated on the GPS code (it is synchronized with C/A code, which helps resolve the code-phase ambiguity if needed [Ash88]). Under normal circumstances, navigation messages that are valid for overlapping periods of four hours are uploaded once a day from the ground segment to individual spacecraft. Messages are then broadcast from satellite to users and usually updated every two hours [Par96].

The navigation message is subdivided into frames and sub-frames [ICD93]. The first three sub-frames, repeated every 30s, provide mostly information on the transmitting satellite, including:

- the 16 ephemeris parameters mentioned in Section 2.1.1,

- three coefficients of a second order polynomial and a reference time for the satellite clock corrections, and
- indexes of satellite health and estimated ranging accuracy.

The data in the last two sub-frames is spread over multiple frames that take up to 12.5min to be completely broadcast. It includes:

- a set of simplified ephemeris, clock and health parameters for the entire satellite constellation, referred to as the almanac, and
- eight parameters for the ionospheric delay model developed by Klobuchar (a half cosine approximation applied as a function of time and location) [Klo87].

Thus, the GPS navigation message provides satellite position, velocity and clock data and ionospheric corrections. Their precision is severely limited by the low 50bps data rate, but higher rates would increase the signal's tracking error. Before addressing how to further improve ranging accuracy, Section 2.3 presents an overview of the most influential error sources.

2.3 GPS Measurement Error Sources

The GPS ranging accuracy is altered by error sources including uncertainties in satellite clocks and positions ${}^s\mathcal{E}_{SV,k}$, signal propagation delays in the ionosphere ${}^s\mathcal{E}_{I,k}$ and troposphere ${}^s\mathcal{E}_{T,k}$, user receiver noise and multipath ${}^s\mathcal{E}_{RNM-\phi,k}$. The first three sources of error are spatially correlated, meaning that receivers located within close distance to each other (a few kilometers) experience the same satellite-related and atmospheric errors. The latter are eliminated in DGPS (discussed in Section 2.4) by differencing measurements from two nearby receivers. Error sources, summarized in Figure 2.2, are

briefly introduced in this section. Experimental data, processed using known estimation methods, illustrate their impact on GPS observations. The carrier phase equation is rewritten as:

$${}^s\phi_k = {}^s r_k + \tau_k + {}^s N + {}^s \epsilon_{SV,k} - {}^s \epsilon_{I,k} + {}^s \epsilon_{T,k} + {}^s \epsilon_{RNM-\phi,k}. \quad (2.1)$$

The treatment of measurement error sources is a central part in the designs of the laser-augmented and of the Iridium-augmented GPS navigation algorithms.

2.3.1 Satellite Clock and Orbit Ephemeris Errors. The accuracy of the GPS ephemeris and clock model parameters is limited by the number of ground reference stations used for their estimation, by the update frequency of the navigation message and by its data rate. Accurate satellite positions and clock deviations from true GPS system time can be obtained using more sophisticated models and using observations from a denser network of ground reference stations.

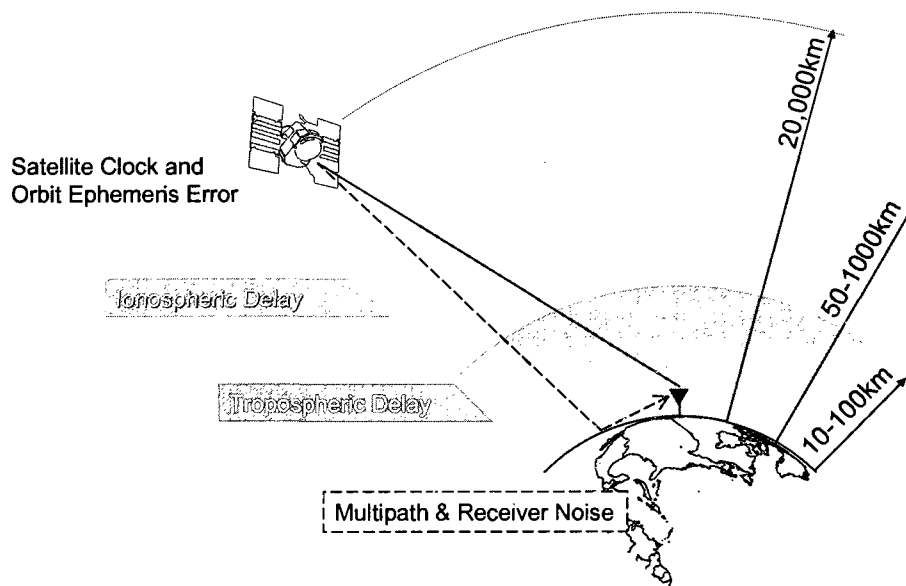


Figure 2.2. Satellite Measurement Error Sources

Precise post-processed satellite orbit and clock solutions are available online (e.g., on the website of the International GNSS Service or IGS) and achieve better than decimeter-level spacecraft positioning and clock-deviation estimation performances. They are often used as truth solutions when evaluating the accuracy of GPS broadcast ephemerides [Oly02] [War03].

The difference between IGS and GPS broadcast satellite positions is plotted in Figure 2.3 over 24 hours (on 1/1/2006) for two satellites (labeled PRN#1 and PRN#24). The reference frame used to express position coordinates is oriented relative to the SV trajectory. The deviation for the in-track coordinate is the largest. Because of the constellation's altitude, the ranging error for a user on earth is mostly affected by the radial component, which varies periodically with amplitude of approximately 1m. Broadcast ephemeris updates are indicated by grey vertical lines, and generate abrupt changes in the curves.

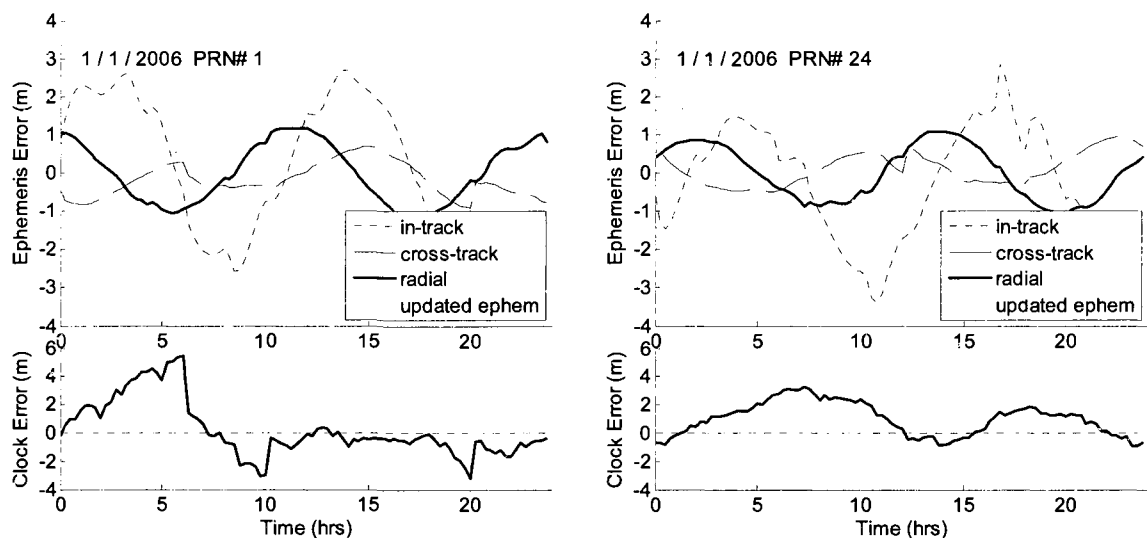


Figure 2.3. Satellite Orbit Ephemeris and Clock Errors Over a 24hour Period

Residual satellite clock deviations were computed using truth data from the Center for Orbit Determination in Europe (because IGS is referenced to a time system different from GPS time). The resulting ranging errors are presented in the lower graphs. They are noisier for the older satellite labeled PRN#1, which has since been decommissioned, but do not exceed 5m. Overall, GPS satellite clock and ephemeris errors each cause ranging errors on the order of 1.5m (root-mean-square or rms) [Mis06].

2.3.2 Signal Propagation Path Errors. The ionosphere is a layer of the atmosphere extending from an altitude of 50km to 1000km above the earth. It is composed of charged particles of gases that get excited by solar ultraviolet radiation. The resulting non-uniform density of electrons causes changes in the satellite signal propagation speed that vary with geomagnetic latitude, time of day, season, and level of activity in the 11-year long solar cycle.

The ionosphere is the largest source of uncertainty in SV ranging observations. It generates a delay in code measurements and an advance of equal magnitude in carrier phase data (hence the negative sign on the ionospheric term in equation 2.1), which are proportional to the total electron content in the path of the signal, and to the inverse square of the carrier's frequency. This frequency-dependence is exploited in dual-frequency implementations to effectively eliminate ionospheric disturbances.

This characteristic of dispersive media can also be used to evaluate the impact of the ionosphere on ranging measurements (e.g., [Han00a]), as illustrated in Figure 2.4. Dual-frequency observations were collected during one winter day and one summer day in Chicago (on 11/30/2006 and 7/12/2007). A biased, scaled and noisy measure of the

vertical ionospheric delay on L1 frequency is measured using the difference of carrier phase observations at L1 and L2 frequencies [Mis06]. The centimeter-level measurement noise is negligible. The constant bias (including cycle ambiguities) is estimated using code measurements averaged over 20min around the SV elevation peak. Finally, a frequency coefficient and an obliquity factor are applied to obtain estimates of the vertical ionospheric delay [Mis06] (more on ionosphere modeling in Chapter 4).

Figure 2.4 presents measured ionospheric delay variations over two 24-hour periods. The numerous curves correspond to measurements from different SVs. They are spread vertically because at any one epoch in user local time, the satellite's lines of sight were piercing distant parts of the ionosphere. Still, the figure clearly shows increasing ionospheric delay during daylight hours, and lower values at night time. The data was collected at one of the quietest periods in the solar cycle, which explains why the highest value barely reaches 2.5m.

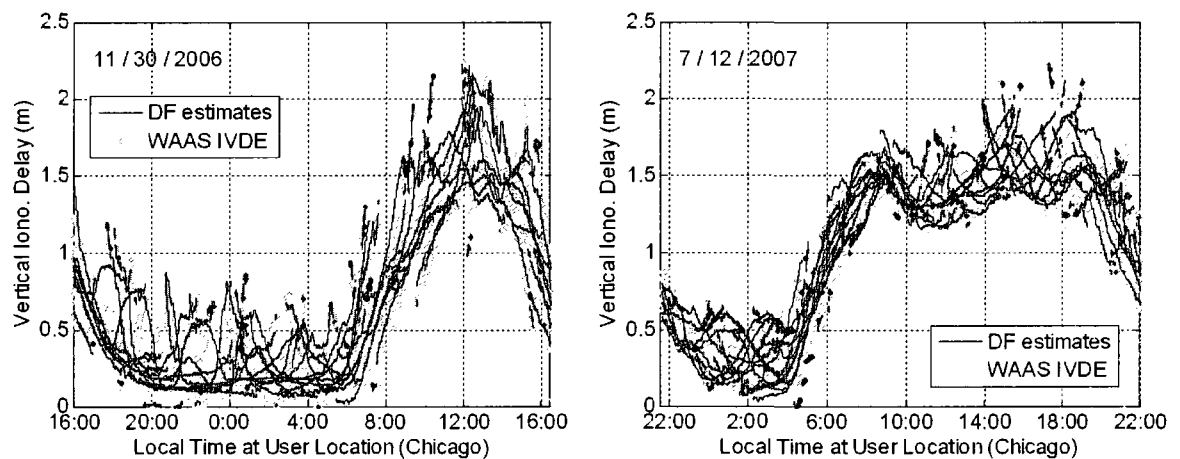


Figure 2.4. Ionospheric Error over a 24hour Period

In general, the ionosphere causes unpredictable errors often exceeding three meters (evaluated to be about 5m rms in [Mis06]), and reaching tens of meters during ionospheric storms. Dual-frequency implementations won't be widely available for civilian applications before 2020. In the meantime, approximately 50% of the error for single-frequency users can be removed using Klobuchar's empirical model mentioned in Section 2.2.3.

Finally, signal refraction in the troposphere, the lower part of the earth's atmosphere, delays the transmission of SV measurements. The troposphere is made of electrically neutral gases not uniform in composition, including dry gases whose behavior is largely predictable, and water vapor, which is random but represents a much smaller fraction of the error. The majority of the delay can therefore be removed by troposphere modeling (e.g., using the WAAS model [MOP01]). The residual error does not exceed a few decimeters.

2.3.3 Receiver Signal Tracking Error. The receiver noise depends on the signal structure, signal to noise ratio, antenna design and receiver electronics. A signal can typically be tracked to within about 1% of a cycle [Mis06], which explains the difference of two orders of magnitude for the receiver measurement noise of code (meter-level) and carrier phase (centimeter-level). In addition, multipath error, caused by unwanted signal reflections reaching the user receiver, will depend on the satellite geometry, on the environment surrounding the antenna, and on the antenna technology.

The effects of receiver noise and multipath can be evaluated using the aforementioned founding principle of DGPS: differencing observations from two nearby

receivers eliminates satellite-related and atmospheric errors (${}^s\mathcal{E}_{SV,k}$, ${}^s\mathcal{E}_{I,k}$ and ${}^s\mathcal{E}_{T,k}$ in equation 2.1). The differential true range and cycle ambiguities (corresponding to r_k and N after differencing) can then be computed using the precisely surveyed baseline vector between the two static antennas and the estimation algorithm of Section 2.4.1. A second difference between measurements from two satellites gets rid of the differential receiver clock deviation (corresponding to τ_k) so that a scaled version of the signal tracking error term ${}^s\mathcal{E}_{RNM-\phi,k}$ may be isolated. Furthermore, a measure of the receiver noise is obtained if the two receivers are connected to a single antenna (using a device called a splitter), in which case multipath effects cancel out.

These well-established methods were applied to a set of data collected in March 2005, with a sampling period T_p of 1s, for two satellites simultaneously in view over more than six hours (PRN#1 and PRN#25). The first and third plots of Figure 2.5 display the carrier and code phase receiver noise (measured with zero baseline, labeled ZB). The amplitude decreases as the satellites' elevation increases (bottom plot), and is much higher for code than for carrier observations.

The receiver noise is uncorrelated in time. The raw carrier phase receiver noise ${}^s\mathcal{V}_{RN-\phi,k}$ is well modeled as a normally distributed random variable, with zero mean and a bounding variance $\sigma_{RN-\phi}^2$ (sometimes scaled by a coefficient function of the elevation).

The following notation is used in the rest of the dissertation:

$${}^s\mathcal{V}_{RN-\phi,k} \sim \mathbf{N}(0, \sigma_{RN-\phi}^2). \quad (2.2)$$

The same model may be used for raw code receiver noise ${}^s\mathcal{V}_{RN-\rho,k}$, whose variance $\sigma_{RN-\rho}^2$ is much larger. In order to get a measure of the raw data amplitude, a scaling factor of

1/4 must be applied to the variances of the double-difference measurements in Figure 2.5 (assuming that signals from two SVs and two receivers are independent).

The second and fourth graphs of Figure 2.5 were established with a 25m baseline distance between antennas. In this case, both receiver noise and multipath are observed with the double-difference measurements. Periodic variations with centimeter-level amplitude in the carrier phase data are typical of multipath effects.

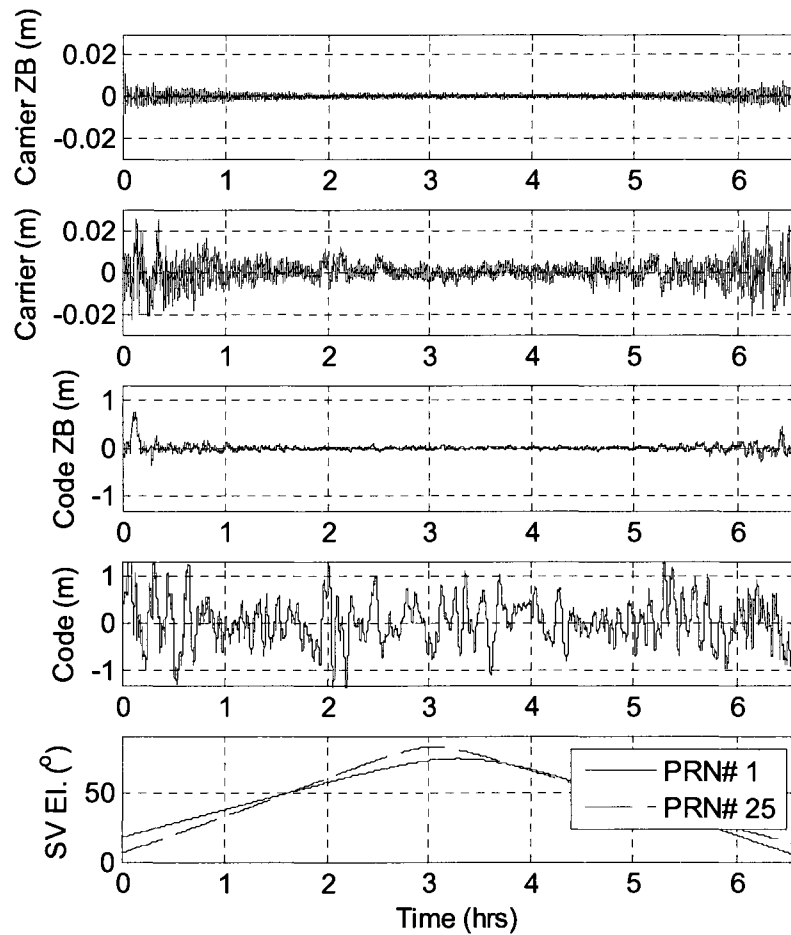


Figure 2.5. Multipath and Receiver Noise

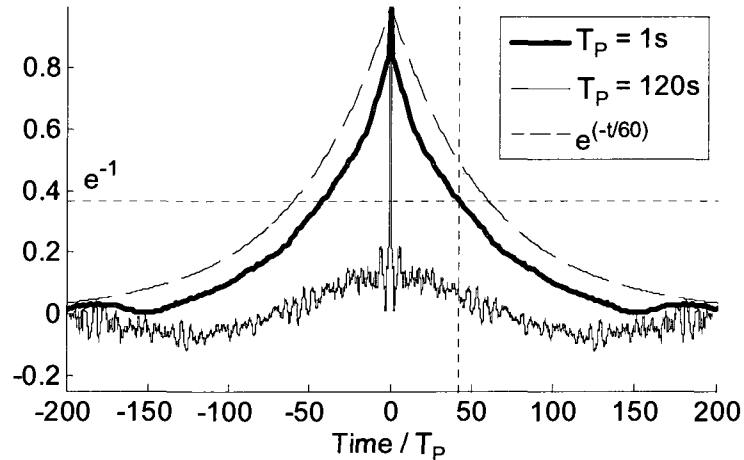


Figure 2.6. Carrier Phase Sample Autocorrelation Function

Multipath time correlation is further analyzed by plotting the sample autocorrelation function of the carrier phase double-difference observations in Figure 2.6 (after normalization by the sample variance). The thick solid curve (labeled $T_p = 1s$) shows the autocorrelation for the first 200 samples (at low SV elevation). On the x-axis, time was normalized by the sampling interval T_p (i.e., units are in number of samples) for upcoming comparisons with larger values of T_p (the thin solid curve labeled $T_p = 120s$ is discussed in Section 2.4.1).

The sample autocorrelation ($T_p = 1s$) can be compared to the autocorrelation function of a Markov process defined as: $\varepsilon_{k+1} = e^{-t_k/T} \cdot \varepsilon_k$, where T is the Markov process time constant and t_k is the time at epoch k ($t_k = k \cdot T_p$). The thick solid curve is bounded by a Markov process with $T = 60s$ (dashed curve), which suggests that the time constant T_M of the measured multipath is lower than 60s. In addition, an approximation of T_M is given by the value for which the autocorrelation peak reaches the e^{-1} line

(dotted horizontal line). In this experiment with two static antennas, T_M equals 42s. Lower values are expected in dynamic environments [Kha08].

This section has demonstrated that GPS ranging accuracy was severely limited by satellite-related and atmospheric errors. The latter errors amount to several meters, which erases the benefits that could be drawn from carrier phase centimeter-level tracking precision. The largest part of the measurement error can be removed using differential corrections. They come in various forms described in the following section.

2.4 Differential GPS (DGPS)

Differential corrections help mitigate most of the satellite-dependent and spatially-correlated atmospheric errors. In DGPS, measurements collected at ground reference stations are compared with the known distance between these stations and the satellites. The resulting correction accuracy varies with user-to-ground-station separation distance. Differential architectures can be classified relative to this baseline separation distance.

2.4.1 Short-Baseline Carrier Phase DGPS (CPDGPS). The most straightforward and most efficient DGPS approach consists in directly subtracting measurements from the user and from a nearby reference station (located no more than few kilometers away), thereby eliminating errors that are simultaneously experienced by the two receivers (method used earlier to measure the multipath error). Equation 2.1 becomes:

$${}^s\Delta\phi_k = {}^s\Delta r_k + \Delta\tau_k + {}^s\Delta N + {}^s\epsilon_{RNM-\Delta\phi,k}, \quad (2.3)$$

where Δ indicates the difference between receivers (e.g., ${}^s\Delta r_k$ is the differential true

range). User and reference station must be equipped with a robust data-link to achieve real-time relative positioning. In addition, carrier phase DGPS (CPDGPS) requires that the unknown differential cycle ambiguity ${}^s\Delta N$ be estimated.

Practical implementation of real-time CPDGPS was first achieved in the early 1990's (e.g., [Pai93] [vGr93]). The example algorithm presented in this section has proven its efficiency in various aircraft precision final approach applications [Law96] [Per97] [Heo04]. It was adapted for ground vehicle navigation [Joe06a] and successfully implemented in autonomous lawn mowing applications [Joe04] [vGr04] [Dal05]. This measurement processing procedure is not flexible enough for integration with laser observations, nor with Iridium data, but it is the starting point for this research and preludes to the challenges of the upcoming chapters.

First, some notation is defined for use in the remainder of the thesis. Let $\mathbf{x}_{ENU,k}$ be the three-dimensional reference-to-user position vector at epoch k (bold face are used to distinguish vectors and matrices from scalars) in a local reference frame (for example, in an East-North-Up or ENU frame, whose origin can be chosen at the reference antenna): $\mathbf{x}_{ENU,k} = [x_E \quad x_N \quad x_U]_k^T$. The differential true range ${}^s\Delta r_k$ can be expressed, in terms of $\mathbf{x}_{ENU,k}$ and the LOS vector ${}^s\mathbf{e}_k$ (vector of direction cosines) from user to satellite s , as: ${}^s\Delta r_k = -{}^s\mathbf{e}_k^T \mathbf{x}_{ENU,k}$. This equation is satisfied for user-to-reference distances of up to a few tens of kilometers, where there is no significant difference in LOS vectors between the two receivers. The user's absolute position in a global reference frame is easily deduced if the reference antenna location is known.

The differential carrier phase equation 2.3 becomes:

$${}^s \Delta \phi_k = -{}^s \mathbf{e}_k^T \mathbf{x}_{ENU,k} + \Delta \tau_k + {}^s \Delta N + {}^s \mathcal{E}_{RNM-\Delta \phi,k}, \quad (2.4)$$

and for code:
$${}^s \Delta \rho_k = -{}^s \mathbf{e}_k^T \mathbf{x}_{ENU,k} + \Delta \tau_k + {}^s \mathcal{E}_{RNM-\Delta \rho,k}. \quad (2.5)$$

For clarity of notation, the vectors \mathbf{u}_k and the geometry vector ${}^s \mathbf{g}_k^T$ are defined as:

$$\mathbf{u}_k = [\mathbf{x}_{ENU} \quad \Delta \tau]_k^T, \quad \text{and} \quad {}^s \mathbf{g}_k^T = [-{}^s \mathbf{e}_k^T \quad 1] \quad (2.6)$$

so that:
$${}^s \Delta \phi_k = {}^s \mathbf{g}_k^T \mathbf{u}_k + {}^s \Delta N + {}^s \mathcal{E}_{RNM-\Delta \phi,k}.$$

Measurements are stacked together and written in vector form: $\Delta \boldsymbol{\phi}_k = [{}^1 \Delta \phi \quad \dots \quad {}^{n_s} \Delta \phi]_k^T$,

for a total number of visible satellites noted n_s . Vectors of code measurements ($\Delta \boldsymbol{\rho}_k$)

and of cycle ambiguities (ΔN) are constructed in the same manner. The geometry matrix

\mathbf{G}_k is defined as: $\mathbf{G}_k = [{}^1 \mathbf{g} \quad \dots \quad {}^{n_s} \mathbf{g}]_k^T$.

Real-time cycle ambiguity estimation is performed using Kalman filter (KF), which recursively provides state estimates in a way that minimizes the mean of the squared errors. As noted in Section 2.2.2, the CPDGPS algorithm exploits the fact that the cycle ambiguity ${}^s \Delta N$ is the only term in equation 2.4 that does not vary with time. When inputting carrier phase measurements into the KF, both measurement redundancy ($n_s > 4$) and changes in satellite geometry, \mathbf{G}_k , contribute to the simultaneous estimation of cycle ambiguities and user position. Unambiguous code phase measurements also contribute to the process.

An additional complication stems from the time correlation in GPS signals due to multipath. The practical solution proposed in the aforementioned publications is to carry out two separate processes summarized in Tables 2.1 and 2.2 and described below.

Table 2.1. Equations for the Cycle Ambiguity Estimation Process [Per97]

Description	Equation
Process equation*	$\begin{bmatrix} \Delta \mathbf{u}_{k+1} \\ \Delta \mathbf{N} \end{bmatrix} = \begin{bmatrix} \mathbf{u}_k \\ \Delta \mathbf{N} \end{bmatrix} + \begin{bmatrix} \mathbf{w}_{\mathbf{u},k} \\ \mathbf{0} \end{bmatrix}, \quad \text{with } \mathbf{w}_{\mathbf{u}} \sim N\left(0, \lim_{\mu \rightarrow \infty} (\mu \cdot \mathbf{I}_4)\right)$
Measurement equation*	$\begin{bmatrix} \Delta \rho \\ \Delta \phi \end{bmatrix}_k = \begin{bmatrix} \mathbf{G} & \mathbf{0} \\ \mathbf{G} & \mathbf{I}_{n_s} \end{bmatrix}_k \begin{bmatrix} \mathbf{u}_k \\ \Delta \mathbf{N} \end{bmatrix} + \begin{bmatrix} \mathbf{v}_{\Delta \rho} \\ \mathbf{v}_{\Delta \phi} \end{bmatrix}_k, \quad \text{with } \begin{matrix} \mathbf{v}_{\Delta \rho} \sim N(0, 2\sigma_{RNM-\rho}^2 \cdot \mathbf{I}_{n_s}) \\ \mathbf{v}_{\Delta \phi} \sim N(0, 2\sigma_{RNM-\phi}^2 \cdot \mathbf{I}_{n_s}) \end{matrix}$
Using the notation:	$\hat{\mathbf{P}}_k = \begin{bmatrix} \hat{\mathbf{P}}_{\mathbf{u}} & \hat{\mathbf{P}}_{\mathbf{uN}} \\ \hat{\mathbf{P}}_{\mathbf{uN}}^T & \hat{\mathbf{P}}_{\mathbf{N}} \end{bmatrix}_k$
KF time and measurement info. update*	${}^{KF} \hat{\mathbf{P}}_k^{-1} = \begin{bmatrix} \mathbf{0} & \mathbf{0} \\ \mathbf{0} & \hat{\mathbf{P}}_{\mathbf{N}}^{-1} \end{bmatrix}_{k-1} + \begin{bmatrix} \mathbf{G} & \mathbf{0} \\ \mathbf{G} & \mathbf{I}_{n_s} \end{bmatrix}_k^T \begin{bmatrix} \mathbf{V}_{\Delta \rho}^{-1} & \mathbf{0} \\ \mathbf{0} & \mathbf{V}_{\Delta \phi}^{-1} \end{bmatrix} \begin{bmatrix} \mathbf{G} & \mathbf{0} \\ \mathbf{G} & \mathbf{I}_{n_s} \end{bmatrix}_k$

* at epoch k corresponding to time t_k , such that $t_{k+1} - t_k = 2T_M$ ($T_M \geq 1 \text{ min}$)

First, the cycle ambiguity estimation procedure is a KF measurement update performed at regular intervals equal to $2T_M$ (selecting a multipath time constant T_M of 60s is conservative). Measurements collected at these intervals are assumed uncorrelated. This assumption is verified in Figure 2.6 with the autocorrelation function of sample measurements taken at 120s intervals (thin solid curve labeled $T_p = 120 \text{ s}$). It shows a very sharp peak, crossing the e^{-1} line even before the second sample. In this case, the differential code and carrier phase single-difference measurement noise vectors are no longer correlated in time. They are respectively defined as $\mathbf{v}_{\Delta \rho}$ and $\mathbf{v}_{\Delta \phi}$ in Table 2.1, where \mathbf{I}_n designates a $n \times n$ identity matrix and $\sigma_{RNM-\rho}^2$ and $\sigma_{RNM-\phi}^2$ are the variances of the raw receiver noise and multipath. The measurement equation takes the form:

$$\mathbf{z}_k = \mathbf{H}_{GPS,k} \mathbf{x}_k + \mathbf{v}_k, \quad (2.7)$$

where $\mathbf{v}_k = \begin{bmatrix} \mathbf{v}_{\Delta \rho}^T & \mathbf{v}_{\Delta \phi}^T \end{bmatrix}_k^T$ and

$$\mathbf{z}_k = \begin{bmatrix} \Delta \boldsymbol{\rho}^T & \Delta \boldsymbol{\varphi}^T \end{bmatrix}_k^T. \quad (2.8)$$

$\mathbf{H}_{GPS,k}$ is the observation matrix and \mathbf{x}_k is the state vector (of length $n_x = 4 + n_s$):

$$\mathbf{H}_{GPS,k} = \begin{bmatrix} \mathbf{G} & \mathbf{0} \\ \mathbf{G} & \mathbf{I}_{n_s} \end{bmatrix}_k \quad \text{and} \quad \mathbf{x}_k = \begin{bmatrix} \mathbf{u}_k \\ \Delta \mathbf{N} \end{bmatrix}. \quad (2.9)$$

Besides, the process equation expresses the constancy of $\Delta \mathbf{N}$ and the total lack of knowledge on the states \mathbf{u}_k . It is written in the form:

$$\mathbf{x}_{k+1} = \boldsymbol{\Phi}_{GPS} \mathbf{x}_k + \mathbf{w}_k,$$

where $\boldsymbol{\Phi}_{GPS} = \mathbf{I}_{n_x}$ and $\mathbf{w}_k = [\mathbf{w}_{\mathbf{u},k}^T \quad \mathbf{0}]^T$. (2.10)

The KF covariance measurement and time updates, written in the information form, are combined into a single equation [Per97].

Then, in a separate stage (Table 2.2), a weighted least squares (WLS) solution provides position estimation at regular sampling intervals T_p (e.g., $T_p = 1$ s), using the incoming measurements and the cycle ambiguity estimates output by the KF. The WLS does not propagate information in time, so that multipath correlation is not an issue. Code measurements bring minimal information and can be left aside.

Table 2.2. Equations for the Positioning Process

Description	Equation
Measurement equation*	$\Delta \boldsymbol{\varphi}_j - \Delta \hat{\mathbf{N}}_{k-1} = \mathbf{G}_j \mathbf{u}_j + \mathbf{v}_{\Delta \boldsymbol{\varphi},j}$
WLS covariance*	${}^{LS} \hat{\mathbf{P}}_{\mathbf{u},j} = \left(\mathbf{G}_j^T (\mathbf{V}_{\Delta \boldsymbol{\varphi}} + \hat{\mathbf{P}}_{\mathbf{N},k-1})^{-1} \mathbf{G}_j \right)^{-1}$

*: at any epoch j between times t_k and t_{k+1} (with $t_{k+1} = t_k + 2T_M$)

In this work, one important clarification is added. It is worth noticing as preamble that whereas $\Delta\mathbf{N}$ is constant, its estimate $\Delta\hat{\mathbf{N}}_k$ improves at each KF update. In Table 2.2, the WLS measurement is not based on the most recent cycle ambiguity estimate, but on the preceding one $\Delta\hat{\mathbf{N}}_{k-1}$. This additional condition, far from being obvious, ensures that the period between KF and WLS measurements ($\Delta\phi_{k-1}$ and $\Delta\phi_j$, respectively) used to estimate \mathbf{u}_j is never smaller than $2T_M$, so that the assumption of uncorrelated observations remains satisfied. Incidentally, it requires an initialization period between the first two KF updates (e.g. using code). A detailed explanation based on analytical derivations of the covariance matrices is given in Appendix A.

This algorithm was coded in the C programming language, on a Linux-based embedded platform [Joe04]. It was used in Section 2.3.3 as well as in the experiments of Chapter 3 to determine the truth vehicle trajectory. Experience shows that in the best case of a stationary user collecting dual-frequency data, robust fixing of integer cycle ambiguities takes upwards of 15min, depending on satellite geometry (the program uses the LAMBDA method [Teu98] with a value for the probability of incorrect fix defined in [Per03]). Reducing this initialization period is part of the issues tackled in Chapters 4-6.

2.4.2 Local and Wide Area Augmentation Systems (LAAS and WAAS). The main limitation regarding CPDGPS is that single-difference measurement equations 2.4 and 2.5 are only applicable within a few kilometers of the reference station at most. Beyond this point, satellite clock and orbit ephemeris and atmospheric errors must be accounted for. Fortunately, differential errors grow slowly with time and with distance to the reference station. In other words, the temporal and spatial decorrelation can be modeled.

A large number of publications have been dedicated to this problem, and are a major resource for navigation system design and residual error modeling in Chapter 4. In this regard, the Federal Aviation Administration (FAA) has developed two DGPS architectures that have motivated particularly thorough error analyses due to their intended life-critical aircraft navigation applications: the Local Area Augmentation System (LAAS) and the Wide Area Augmentation System (WAAS).

LAAS aims at providing corrections (and integrity information, addressed in Section 2.5) within a limited broadcast radius around selected airport locations (tens of kilometers). Carrier-smoothed code measurements are used to establish ground corrections and aircraft position. In order to minimize the amount of transmitted data, corrections are sent in the form of pseudorange error estimates (additional details are found in [MAS04]). Measurement smoothing in LAAS requires that residual errors be modeled over time. The same challenge is faced in Chapter 4 for the GPS/Iridium system.

The differential concept in WAAS aims at servicing continental areas with minimal ground infrastructure. Satellite LOS between user and ground stations are no longer the same. As a result, vector corrections are employed instead of scalar corrections used in LAAS. For example, WAAS ephemeris corrections come in the form of three-dimensional satellite position (and velocity) error estimates.

The ionosphere, the largest and most unpredictable source of error, is sampled using dual-frequency measurements from a network of 38 wide-area reference stations (WRS) spread across North America (ionosphere sampling resolution is determined by WRS density). The WRS are mapped in Figure 2.7a. These observations are then used at wide-area master stations (WMS - in San Diego, CA and Herndon, VA) to compute

ionospheric vertical delay estimates (IVDE) for a 5deg×5deg latitude-longitude grid of locations [MOP01]. According to the algorithm described in [Wal00] and [Bla03], the IVDE at each ionospheric grid point (IGP) location is determined by applying a planar fit to all WRS measurements contained within a certain radius. Figure 2.7b presents a map of IVDEs during one of these experiments. The precision of these estimates decreases in coastal areas due to depleted ground station coverage.

IVDEs, along with estimated satellite positions, clock offsets and drifts, are broadcast at a 250bps data rate via geostationary (GEO) spacecraft to users who can compute corrections for the location of interest. It is worth noticing that because of the low 250bps data rate, IVDE values at each IGP location are discretized with a 0.125m resolution. For example, Figure 2.4 compares ionospheric delays computed using dual-frequency measurements (collected in Chicago) versus WAAS estimates. Each GEO satellite also provides an additional GPS-like ranging measurement.

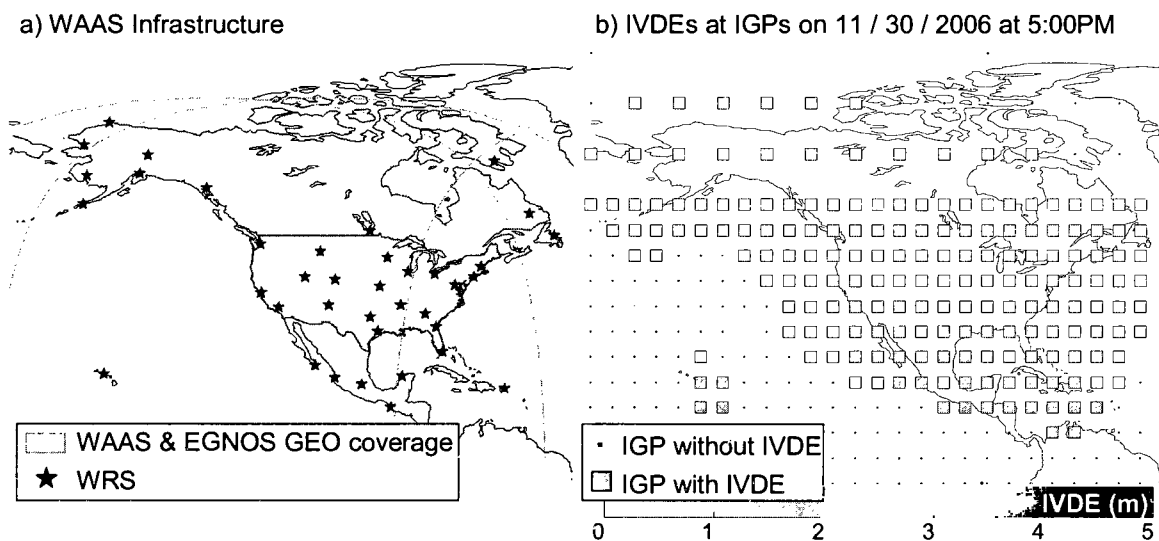


Figure 2.7. Overview of the WAAS Infrastructure and Ionospheric Corrections

WAAS has been operational since 2003 and produces a 95% positioning accuracy of better than 5m for single-frequency code-phase GPS users across the United States [NST03]. Similar satellite-based augmentation systems (SBAS) are under development elsewhere for example in Europe (the European Geostationary Navigation Overlay Service, or EGNOS), and in Japan (Multi-functional Satellite Augmentation System, or MSAS).

Both LAAS and WAAS also provide information on the estimated quality of the transmitted corrections. In fact, in the context of safety critical applications, providing accurate corrections is not as demanding a requirement as ensuring their robustness. In the case of WAAS, the aforementioned ionospheric and satellite-related long-term corrections are only updated approximately every 2min. In contrast, the update period for fast corrections, 'do not use' flags and error bounds is lower than 10s. Fast-transmitted data aim at protecting the user in case of excessively large errors such as satellite failures or ionospheric storms. The subject of measurement integrity monitoring is treated next.

2.5 Integrity Monitoring

So far in this chapter, the performance of GPS-based positioning has been described in terms of spatial availability (GPS is limited to open-sky areas), initialization time (several tens of minutes for CPDGPS), and accuracy (deteriorated by measurement errors). Positioning accuracy is often defined as the 95% output deviation from truth in the absence of system failures. It is the most intuitive performance metric, but it is insufficient to evaluate a navigation system subjected to faults that could have life-

threatening consequences. This section provides a concise introductory description of navigation requirements and fault detection methods implemented in Chapters 4 to 6.

2.5.1 Navigation Requirements. Four fundamental metrics, originating from aviation applications, are employed to assess the navigation system's performance [MAS04]. *Accuracy* has been discussed above. *Integrity* is defined as the ability of a system to provide timely warnings in case of hazardous navigation error. *Continuity* is the likelihood that the system meets accuracy and integrity requirements over the entire mission duration (e.g., over an aircraft approach), with no unscheduled interruption. *Availability* (or time availability) is the fraction of time that accuracy, integrity and continuity requirements are fulfilled. Accuracy, integrity and continuity are instantaneous measures of mission safety, whereas availability is evaluated over multiple operations.

Detection algorithms are implemented to mitigate the impact of faults. An undetected fault is an integrity threat, whereas a detected but unscheduled failure causes loss of continuity. Therefore, continuity and integrity are competing requirements when defining the sensitivity of the detection algorithm. A quantitative definition of inter-relationships between the four performance metrics is given in [Per96].

2.5.2 Background on Fault Detection. The integrity monitoring functions conducted by the GPS OCS aim at keeping track of the constellation's health and at minimizing the probability of user exposure to multiple simultaneous spacecraft faults. WAAS provides additional protection against all signal-in-space threats including satellite-related faults

and ionospheric anomalies: warnings transmitted through the ground integrity channel (via GEO satellite) must fulfill the demanding time-to-alarm requirement and reach the user within 6s. As an alternative, or as a complement, fault detection may be conducted onboard the user receiver (this point is further discussed in Section 4.4).

Self-contained fault-detection at the user receiver is achieved by verifying the consistency of the over-determined positioning solution using redundant measurements, which is only possible if five or more satellites are visible (six SVs are needed for fault isolation, which is not treated here). This concept was formalized in the late 1980's with a methodology named receiver autonomous integrity monitoring (RAIM). Multiple approaches toward RAIM have emerged over the past two decades [Bro96]. In this work, a well-established least-squares-residuals RAIM method has been selected [Stu88]. It provides a twofold solution to a subtle problem that aims at optimizing service availability: on the one hand, the algorithm must detect all hazardous faults, whereas on the other hand, it can not be too conservative when triggering alarms for fear of making the system needlessly unavailable (errors that have a low impact on the positioning solution must be tolerated).

Most existing implementations of RAIM are snapshot detection schemes that assume redundant observations at one epoch of interest. Existing sequential RAIM algorithms are often complex, make assumptions on user motion, or only target specific fault modes [Bro86] [Bak99] [Clo06]. Recent publications show that fault detection is an active area of research and efforts are ongoing to improve and even optimize the RAIM methodology [Hwa06] [Lee07].

In this research, the GPS/Iridium navigation system exploits past and current measurements, which are all vulnerable to faults. The detection process devised in Chapter 5 is a direct extension of snapshot RAIM, but it is applied to finite windows of successive observations, whose error time-correlation is carefully modeled. The process is implemented using carrier phase observations rather than code data, which allow for a tighter detection threshold while still ensuring a very low false-alarm probability [Per96].

CHAPTER 3

MEASUREMENT-LEVEL INTEGRATION OF CARRIER PHASE GPS WITH LASER SCANNER OBSERVATIONS

The CPDGPS algorithm presented in Section 2.4.1 can achieve real-time centimeter-level positioning accuracy and can be used in a variety of applications including autonomous outdoor ground vehicle navigation [Joe04] [vGr04]. However, robust CPDGPS is restricted to open-sky areas because GPS satellite signals can be significantly attenuated or blocked by buildings, trees, and rugged terrain. In response in this chapter, GPS is augmented with two-dimensional laser scanner measurements from surrounding static obstacles, which are used as landmarks. Laser observations are available when GPS is not, and provide in addition, a means for obstacle detection.

Section 3.1 introduces and analyzes a widely implemented laser-based navigation algorithm known as Simultaneous Localization and Mapping (SLAM). Non-linear laser observations as well as time-correlated GPS code and carrier phase measurements are then combined in a unified measurement differencing extended Kalman filter derived in Section 3.2. The improved performance of this measurement-level GPS/laser integration over a simpler position-domain implementation is quantified by covariance analysis and Monte-Carlo simulations (in Section 3.3), and experimentally validated both in a structured environment and in actual urban canyons (in Section 3.4).

3.1 Laser-Based Simultaneous Localization and Mapping

Over the past two decades, abundant research on robots equipped with non-contact ranging sensors has been dedicated to the reciprocal problems of:

- robotic mapping (i.e., determining obstacle locations knowing the robot's position and orientation) and
- robot localization (i.e., estimating the robot's position using landmarks at known locations) [Thr03].

The simultaneous solution to both problems has been formalized in an algorithm called SLAM [Dis01] or Concurrent Mapping and Localization (CML) [Leo00]. In the perspective of GPS-augmentation, SLAM enables vehicle positioning using previously unknown features in the environment, which in this work are assumed stationary.

In recent years, practical implementations of SLAM were made possible by advances in embedded computer and sensor technology, in particular with the development of affordable, high-update-rate, precise laser scanners described in Section 3.1.1. When using laser scanners to sense the surrounding environment, the complete solution to the SLAM problem can be subdivided into three tasks represented in Figure 3.1. The first two tasks of feature extraction and data association are concisely addressed in Sections 3.1.2 and 3.1.3. An extended Kalman filter (EKF) approach is selected for the third task of simultaneous vehicle and landmark positioning (Section 3.1.4). The EKF handles the non-linearity of the laser's polar measurements for Cartesian position coordinate estimation, and provides an incremental solution for real time implementations.

3.1.1 Laser Scanner: Functioning and Implementation. The term LASER is an acronym for Light Amplification by Stimulated Emission of Radiation. Laser light refers to electromagnetic radiations that are both spatially coherent (emitted in a narrow, low-

divergence beam) and temporally coherent (whose phase does not vary randomly with time), which is distinctive from most other light emissions including outdoor ambient light.

A laser scanner (or laser radar) emits pulsed infrared laser beams that are reflected from surfaces of nearby objects and returned to the scanner's receiver. Signal time-to-return measurements are used to determine distances to the reflecting objects. The precision of the ranging measurement is affected by target surface properties (color, material reflectivity) and by the angle of incidence of the laser on the target surface [Ye02]. The pulsed laser beam is deflected with a rotating mirror to enable two-dimensional scanning [SIC06]. As a result, a raw laser scan is made of hundreds of ranging measurements at regular angular intervals (depicted in Figure 3.2).

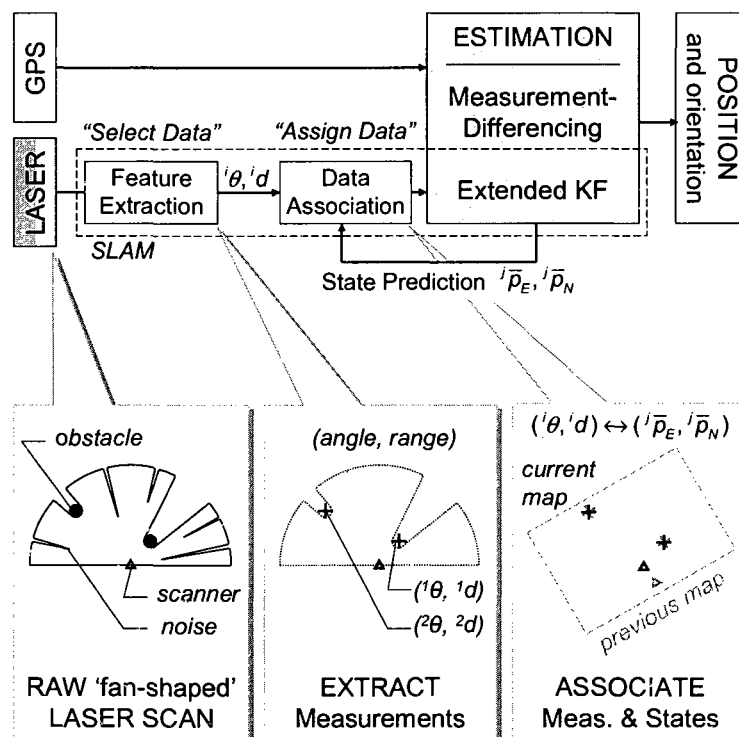


Figure 3.1. Three-Stage SLAM Process Included in the GPS/Laser Integration Scheme

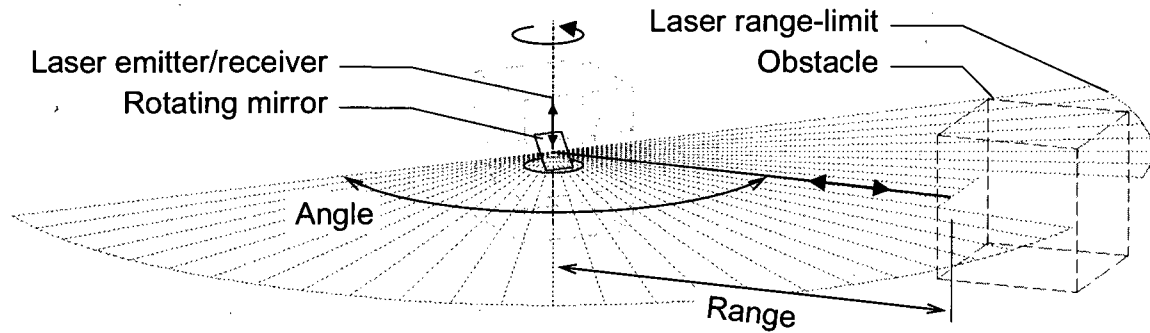


Figure 3.2. Laser Scanner Description

Using hundreds of observations as direct inputs to the EKF for vehicle and landmark positioning would be cumbersome. Besides, not all data in a laser scan is useful because few obstacles in the environment are actually reliable landmark candidates. Therefore, two intermediary procedures are implemented: *feature extraction* aims at selecting the few measurements originating from consistently identifiable landmarks, and *data association* assigns these extracted observations to the corresponding landmark states in the EKF.

Extensive research has been dedicated to these two problems (e.g. [Ten01] [Mad02] [Tan04]), which are especially challenging in natural environments (assuming no prior knowledge on the shape and nature of the landmarks). In order to keep the focus of this work on the measurement-level integration of GPS and laser observations, simple but efficient environment-specific procedures are selected. Rather than explaining the details of their implementation (see Appendix B), the following two sub-sections describe the interactions between feature extraction, data association and position estimation.

3.1.2 Feature Extraction. The goal of the feature extraction algorithm, which here includes impulse-noise rejection, segmentation, and data selection (illustrated in Figure 3.3 for data collected in an alley in Chicago), is to find features in the raw laser scan that can be repeatedly and consistently identified while the laser's viewpoint is changing due to vehicle motion. The difficulty resides in distinguishing such reliable landmark candidates from noise in the measurements and from other unwanted viewpoint-variant obstacles in the surroundings. Failure to do so results in fewer measurements for the desired landmarks, or in observations originating from unwanted objects, therefore degrading the vehicle positioning accuracy.

With regard to the number of extracted point-features, the extraction routine should take the following tradeoff into account: on the one hand, more measurements generate better position estimates using an EKF, while on the other hand, more extracted measurements increase the risk of failures in the data association process (landmarks that are closer together are easier to confuse). Because faults in the association have much more dramatic effects on the final position solution than the use of a few additional measurements in the EKF, the feature extraction algorithm is calibrated so that only the few easiest to identify landmarks are considered.

In forests and urban canyons, centers of tree trunks and buildings' edges meet the above selection criteria: they are few within the range of the laser and can be consistently extracted. A laser scan taken on the site of one of the experiments (in a back alley in Chicago), is presented in Figure 3.4. The data is very noisy because of the wide variety of materials found in the street (wood, brick, glass, metal, vegetation) and the complex and cluttered structure of the surroundings (trees, cars, garbage cans, traffic signs). Also,

walls, doors and fences often obstruct gaps between buildings so that the building's edges are no longer visible on the laser scan. Therefore, poles, edges of garage doors and other wall discontinuities are sometimes used as landmarks.

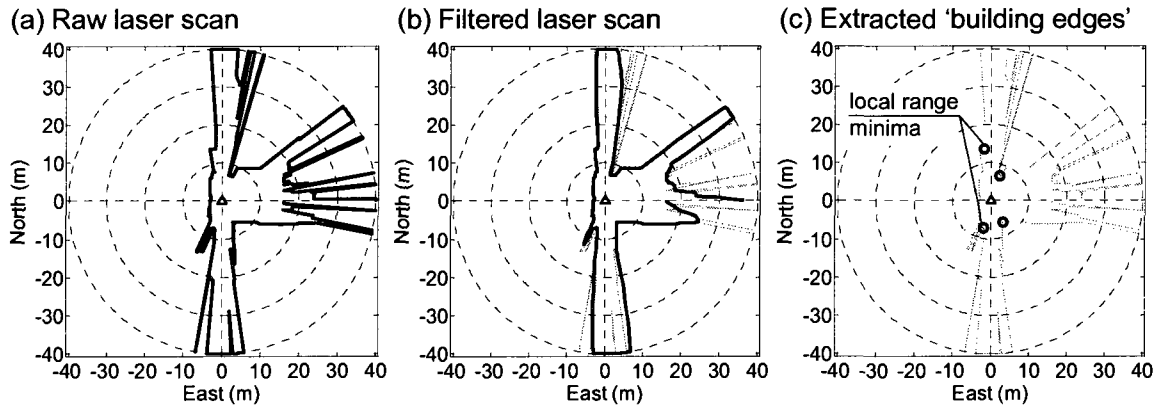


Figure 3.3. Feature Extraction Process

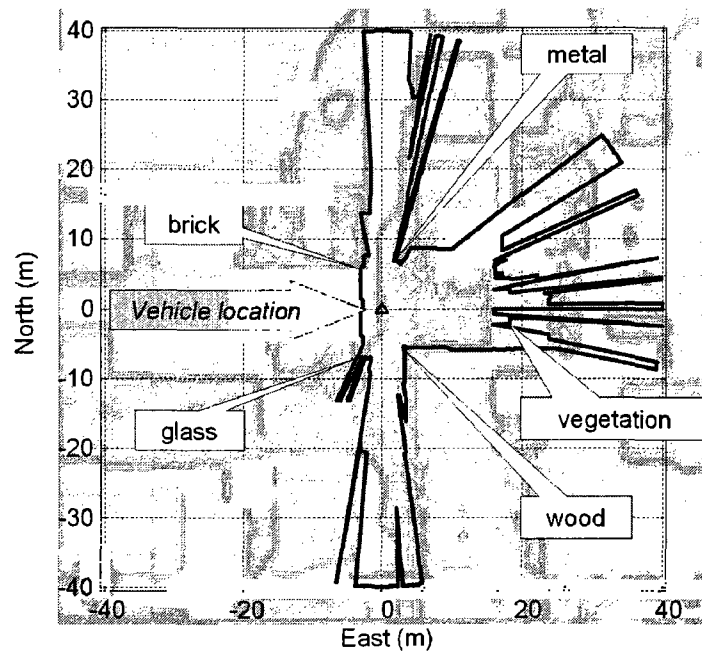


Figure 3.4. Raw Laser Scan Superimposed with a Satellite Picture of the Alley

3.1.3 Data-Association. The data association process establishes correspondences between consecutive sets of measurements and a continuously updated map of landmarks. More precisely, current extracted measurements (resulting from feature extraction) are matched with projected measurement estimates to previously observed landmarks. In this work, measurement prediction is obtained after projection in time of the EKF state estimates using a simple vehicle dynamic model. A nearest neighbor approach based on the normalized innovation square is employed to perform the association (see [Bar88] and Appendix B for details). More elaborate variants of this process can be found in the literature [Dis01] [Mak95].

A failure in the data association process, also called miss-association, can lead to the following outcomes:

- the measurement is not associated with its corresponding landmark, and is therefore assumed to correspond to a new landmark (usually nearby the former landmark), or
- the measurement is associated with the wrong landmark.

In the first case, the consequence for the estimation process is that there are fewer observations for this given landmark. The second case however can have catastrophic effects on the estimation process, as illustrated in Figure 3.5 for the position-domain integration. In this example, due to erroneous vehicle position and orientation estimates, the system confused a landmark on the right of its trajectory for one on its left. In the following time steps, because the map of landmarks is built incrementally, the vehicle and landmark position errors accumulate and grow without bound.

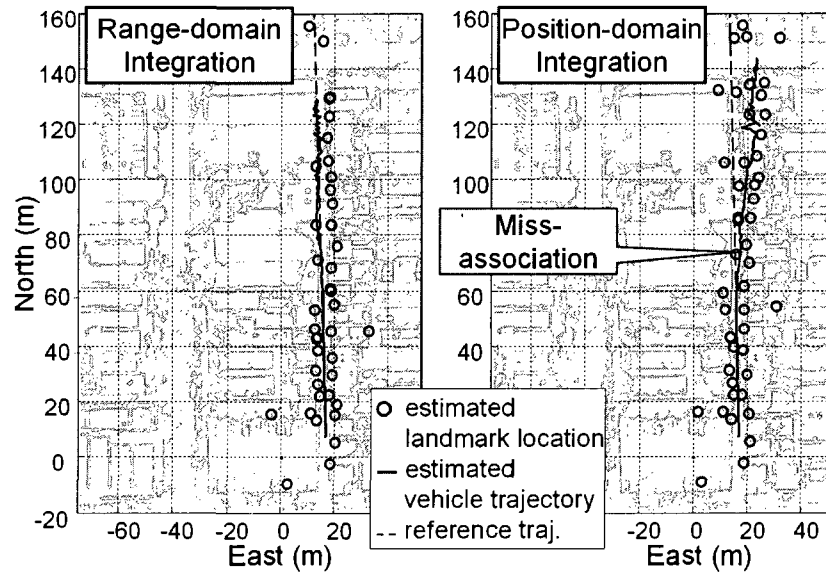


Figure 3.5. Consequence of a Miss-Association in the Position-Domain Approach

Fortunately, other correctly associated measurements can mitigate the effects of such miss-associations. Experimental testing in urban canyons (Section 3.4.2) will demonstrate that additional *absolute* GPS ranging signals, made exploitable by the measurement-level integration, are instrumental in recovering from data association failures.

3.1.4 EKF-based Vehicle and Landmark Localization. The laser-based estimation process can be summarized as follows: given an initial position estimate (e.g., provided by GPS), the vehicle trajectory can be determined by keeping track of its relative distance with respect to surrounding landmarks using laser measurements. Because landmark locations are not known in advance, the state vector to be estimated in the EKF includes both vehicle states (composed of the two dimensional position coordinates x_E and x_N in a local reference frame – for example ENU – and of the attitude or heading angle ψ) and

landmark states (i.e., position coordinates ${}^i p_E$ and ${}^i p_N$ for $i=1\dots n_L$ with n_L being the number of landmarks under consideration). The two-dimensional vehicle and landmark model is shown in Figure 3.6.

For the upcoming covariance analysis, in order to study the navigation performance based exclusively on sensor information (without a vehicle dynamic model), the covariance of the vehicle states process noise \mathbf{w}_{EN} and \mathbf{w}_ψ (a Gaussian purely random vector) is inflated. Landmarks are assumed stationary, hence the discrete-time process equation is:

$$\begin{bmatrix} \mathbf{x}_{EN} \\ \psi \\ \mathbf{p} \end{bmatrix}_{k+1} = \begin{bmatrix} \mathbf{I}_2 & \mathbf{0} \\ & 1 \\ \mathbf{0} & \mathbf{I}_{n_L} \end{bmatrix} \begin{bmatrix} \mathbf{x}_{EN} \\ \psi \\ \mathbf{p} \end{bmatrix}_k + \begin{bmatrix} \mathbf{w}_{EN} \\ \mathbf{w}_\psi \\ \mathbf{0} \end{bmatrix}_k \quad (3.1)$$

where

$$\mathbf{x}_{EN} = [x_E \quad x_N]^T,$$

$$\mathbf{p} = [{}^1 p_E \quad {}^1 p_N \quad \dots \quad {}^{n_L} p_E \quad {}^{n_L} p_N]^T$$

and \mathbf{I}_n is a $n \times n$ identity matrix.

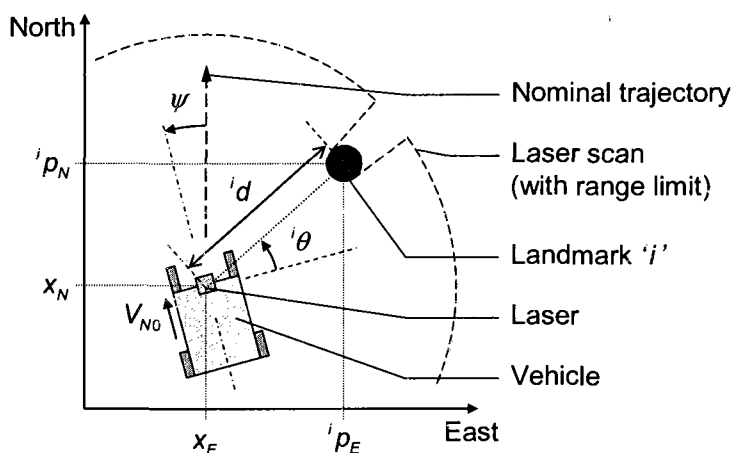


Figure 3.6. Vehicle and Landmark Model

The vehicle is assumed equipped with a 360deg laser scanner. In practice (Section 3.4), two back-to-back 180deg laser scanners are implemented. Successful implementation of the extraction and association procedures results in one ranging and one angular measurement per landmark i , respectively:

$${}^i d = \sqrt{({}^i p_E - x_E)^2 + ({}^i p_N - x_N)^2} + v_d. \quad (3.2)$$

$${}^i \theta = \arctan\left(\frac{{}^i p_N - x_N}{{}^i p_E - x_E}\right) - \psi + v_\theta \quad (3.3)$$

The measurement noise variables v_d and v_θ are assumed normally distributed with zero mean. Their standard deviations ($\sigma_d = 0.01\text{m}$ and $\sigma_\theta = 0.5^\circ$) are determined based on manufacturer specifications and on experimental data.

Equations 3.2 and 3.3 are linearized using an iterative Newton-Raphson method. The linearization about approximate user and landmark positions based on first order terms of the measurements' Taylor expansions is explained in Appendix C. Linearized observations (${}^i d_L$ and ${}^i \theta_L$) for all n_L visible landmarks are stacked together in measurement vectors:

$$\mathbf{d}_L = [{}^1 d_L \quad \dots \quad {}^i d_L \quad \dots \quad {}^{n_L} d_L]^T \quad \text{and} \quad \boldsymbol{\theta}_L = [{}^1 \theta_L \quad \dots \quad {}^i \theta_L \quad \dots \quad {}^{n_L} \theta_L]^T.$$

Thus, the matrix form of the linearized angular and ranging measurement equation is:

$$\begin{bmatrix} \mathbf{d}_L \\ \boldsymbol{\theta}_L \end{bmatrix} = \begin{bmatrix} \mathbf{F}_{d,x} & \mathbf{0} & \mathbf{F}_{d,p} \\ \mathbf{F}_{\theta,x} & -\mathbf{1}_{n_L} & \mathbf{F}_{\theta,p} \end{bmatrix} \begin{bmatrix} \mathbf{x}_{EN} \\ \psi \\ \mathbf{p} \end{bmatrix} + \begin{bmatrix} \mathbf{v}_d \\ \mathbf{v}_\theta \end{bmatrix} \quad (3.4)$$

where $\mathbf{1}_{n_L}$ is a $n_L \times 1$ column vector filled with 1's. The coefficient matrices $\mathbf{F}_{d,x}$, $\mathbf{F}_{\theta,x}$,

$\mathbf{F}_{d,p}$ and $\mathbf{F}_{\theta,p}$ are also defined in Appendix C. Equations 3.1 to 3.4 provide a mathematical description of the laser-based SLAM measurement and dynamic models.

In an effort to understand the drift in positioning error observed using SLAM (e.g., in [Leo92]), an example covariance analysis in four steps is carried out. Figure 3.7 shows the individual effects of (a) the joint angular and ranging measurements, (b) the combination of measurements from multiple landmarks, (c) the correlation between vehicle and landmark position estimates, and (d) the uncertainty on the vehicle's heading angle. For all cases, the vehicle starts with an initial position estimate and passes by landmarks while roving along the North-axis. Covariance ellipses represent vehicle and landmark positioning errors at consecutive sample updates, assuming successful data extraction and association.

Figures 3.7a and 3.7b where landmark position and vehicle azimuth are known, illustrate the task of robotic localization. The elongated shape of the ellipses reflects the values given to the angular and ranging measurement noise covariance. The combined solution in Figure 3.7b coincides with the intersection of the dashed ellipses (for individual landmarks) because measurements from different landmarks are independent.

In Figure 3.7c, the heading angle is still known, but landmark locations are not and must be simultaneously estimated with vehicle trajectory. Both measurement averaging and geometry change due to the vehicle motion contribute to the estimation process so that the positioning error on stationary landmarks decreases steadily.

Finally in Figure 3.7d, the vehicle attitude also becomes an unknown. The performance is dramatically poorer. The absence of absolute information after the initial filter update prevents improvement of the landmark position estimates. Thus, the vehicle

positioning performance across the two-dimensional plane is fully determined by the landmark geometry and initial AGV position uncertainty. In fact, the point that minimizes vehicle positioning error is the initial position, as suggested by lines of constant easting deviation (dashed), which illustrate the laser-based positioning drift with vehicle travel distance. In this case, position estimation simplifies to a problem of dilution of precision for a fixed geometry (determined by the number and location of landmarks relative to initial AGV position).

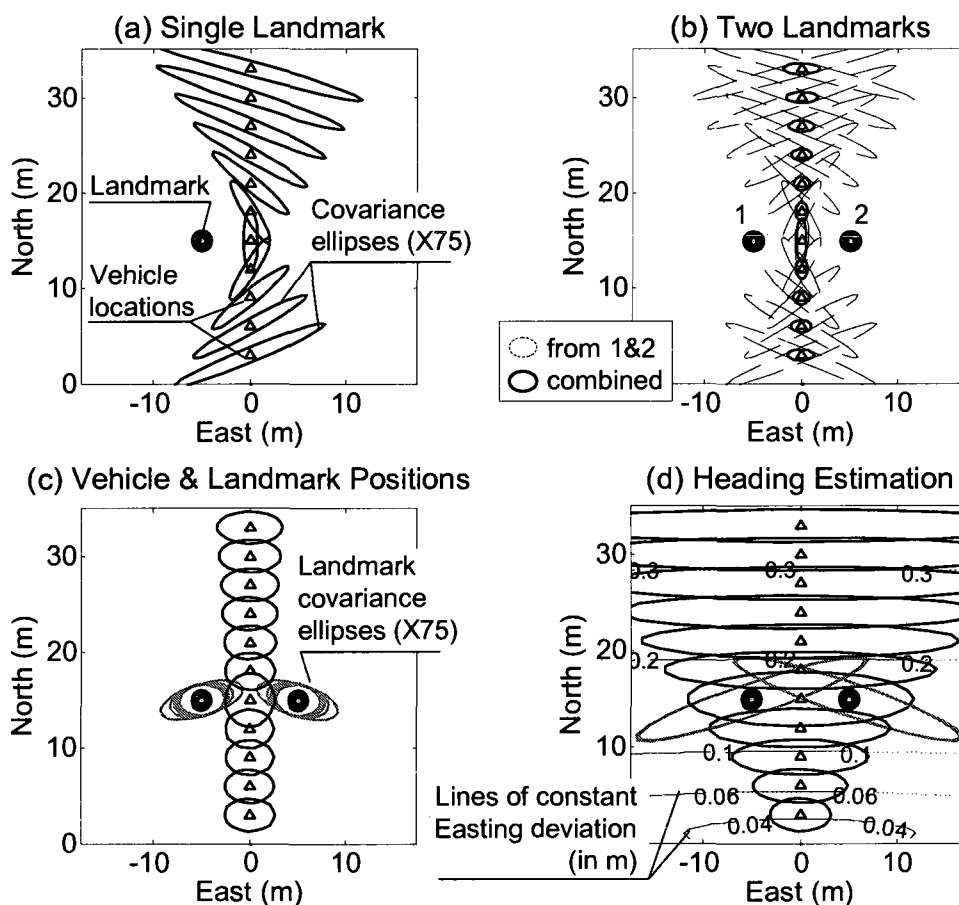


Figure 3.7. Four-Step Covariance Analysis

For straight-line vehicle trajectories, the uncertainty on the cross-track state usually drifts more rapidly than on the in-track coordinate. Also, cross-track requirements in AGV applications are often more stringent. For these reasons, in the remainder of this chapter, the vehicle cross-track position estimate is used as navigation performance criterion.

In the literature, the increase in positioning error over distance is often mitigated using additional attitude information (e.g., [Bay05] [Dis01] [Mad02]), hence generating results better than in the extreme case of Figure 3.7d (no external heading data), but worse than in Figure 3.7c (known heading). Vehicle attitude may be derived from a dynamic model, or from sensors such as inertial systems, encoders or magnetometers, whose output errors unfortunately accumulate with time. In this work, no external attitude information is exploited (worst case of Figure 3.7d). Instead, in the next sections, laser data are combined with GPS. The measurement-level integration aims at optimizing the use of *absolute* GPS ranging signals to limit the laser-based positioning drift (in addition to preventing miss-associations mentioned in Section 3.1.2).

3.2 Measurement-Level GPS/Laser Integration Algorithm

A combined GPS carrier phase cycle ambiguity and position estimation process is derived in a compact formulation in Section 3.2.1. The mathematical backbone of the GPS/laser range-domain integration is presented in Section 3.2.2. A more intuitive description of the system, which is based on qualitative and quantitative performance analyses, is provided in Sections 3.3 and 3.4.

3.2.1 Single-Stage GPS Positioning and Cycle-Ambiguity Estimation Algorithm.

In this subsection, a single-stage carrier phase GPS positioning and cycle ambiguity estimation algorithm is derived, which is later integrated with laser measurements in Section 3.2.2. GPS signals are correlated in time because of multipath reflections. Section 2.4.1 describes a method for real-time CPDGPS positioning in two separate processes [Law96].

- Cycle ambiguity estimation is performed at infrequent intervals (equal to $2T_M$, T_M being the anticipated multipath time constant), using a Kalman Filter (KF). Measurements taken at these intervals are assumed to be uncorrelated.
- A weighted least squares (WLS) solution provides position estimation at each sample time (in this case, the sampling interval T_p is 0.5s) using incoming measurements and cycle ambiguity estimates output by the KF.

This solution is not practical for integration with laser observations. Indeed, landmark and cycle ambiguity states must be updated as soon as new obstacles and satellites come in sight (not only at infrequent intervals), and the WLS process does not propagate prior information.

Equations 2.4 and 2.5 of Section 2.4.1 are expressions of the differential measurements (between user and a nearby reference station) of GPS code and carrier phase signals for a satellite s at epoch k :

$${}^s\Delta\rho_k = -{}^s\mathbf{e}_k^T \mathbf{x}_{ENU,k} + \Delta\tau_k + {}^s\mathcal{E}_{M-\Delta\rho,k} + {}^s\mathcal{V}_{RN-\Delta\rho,k}$$

$${}^s\Delta\phi_k = -{}^s\mathbf{e}_k^T \mathbf{x}_{ENU,k} + \Delta\tau_k + {}^s\Delta N + {}^s\mathcal{E}_{M-\Delta\phi,k} + {}^s\mathcal{V}_{RN-\Delta\phi,k}.$$

The differential code phase receiver noise ${}^s\mathcal{V}_{RN-\Delta\rho,k}$ is normally distributed with zero

mean and standard deviation $\sigma_{RN-\Delta\rho}$ (idem for the carrier, with $\sigma_{RN-\Delta\phi}$). The terms ${}^s\mathcal{E}_{M-\Delta\rho,k}$ and ${}^s\mathcal{E}_{M-\Delta\phi,k}$ are the differential code and carrier phase time-correlated multipath noises (with standard deviations $\sigma_{M-\Delta\rho}$ and $\sigma_{M-\Delta\phi}$ respectively, and time constant T_M). These quantities have been analyzed in Section 2.3.3.

In order to implement frequent GPS filtering updates, the colored multipath noise is modeled as a first order Gauss Markov process:

$$\begin{aligned} {}^s\mathcal{E}_{M-\Delta\rho,k+1} &= e^{(-T_p/T_M)} \cdot {}^s\mathcal{E}_{M-\Delta\rho,k} + {}^s\mathcal{V}_{M-\Delta\rho,k} \\ {}^s\mathcal{E}_{M-\Delta\phi,k+1} &= e^{(-T_p/T_M)} \cdot {}^s\mathcal{E}_{M-\Delta\phi,k} + {}^s\mathcal{V}_{M-\Delta\phi,k} \end{aligned} \quad (3.5)$$

where ${}^s\mathcal{V}_{M-\Delta\rho,k}$ and ${}^s\mathcal{V}_{M-\Delta\phi,k}$ are zero-mean, purely random sequences with respective variances:

$$\left(1 - e^{-2(T_p/T_M)}\right) \sigma_{M-\Delta\rho}^2 \quad \text{and} \quad \left(1 - e^{-2(T_p/T_M)}\right) \sigma_{M-\Delta\phi}^2.$$

Code and carrier measurements for all satellites are stacked together in a measurement vector \mathbf{z}_k (equation 2.8). Let n_s be the number of visible satellites: \mathbf{z}_k is a $2n_s \times 1$ vector. Equation 3.5 becomes:

$$\boldsymbol{\varepsilon}_{M,k+1} = \boldsymbol{\Psi}_{GPS} \boldsymbol{\varepsilon}_{M,k} + \mathbf{v}_{M,k}$$

where $\boldsymbol{\Psi}_{GPS}$ is called the correlation matrix:

$$\boldsymbol{\Psi}_{GPS} = e^{(-T_p/T_M)} \cdot \mathbf{I}_{2n_s}.$$

The GPS measurement vector \mathbf{z}_k is written in the form:

$$\mathbf{z}_k = \mathbf{H}_{GPS,k} \mathbf{x}_k + \boldsymbol{\varepsilon}_{M,k} + \mathbf{v}_{RN,k},$$

where the state vector \mathbf{x}_k and the GPS observation matrix $\mathbf{H}_{GPS,k}$ are expressed in equation 2.9.

A measurement differencing filter can be implemented for computational efficiency. This filter was first introduced in 1968 by Bryson and Henrikson as a way to model correlated measurement noise in a state space representation [Bry68]. It is an efficient alternative to state augmentation because the number of states remains unchanged and the measurement noise matrix is no longer singular. The core idea defining this filter is the elimination of time-correlated measurement noise terms using a pseudo-measurement ${}^r \mathbf{z}_k$ (the superscript r identifies elements of the reduced-order filter):

$$\begin{aligned} {}^r \mathbf{z}_k &= \mathbf{z}_{k+1} - \Psi_{GPS} \mathbf{z}_k \\ {}^r \mathbf{z}_k &= (\mathbf{H}_{GPS,k+1} \Phi_{GPS} - \Psi_{GPS} \mathbf{H}_{GPS,k}) \mathbf{x}_k + \mathbf{H}_{GPS,k+1} \mathbf{w}_k + \mathbf{v}_{M,k} + \mathbf{v}_{RN,k+1} - \Psi_{GPS} \mathbf{v}_{RN,k} \\ {}^r \mathbf{z}_k &= {}^r \mathbf{H}_{GPS,k} \mathbf{x}_k + {}^r \mathbf{v}_k \end{aligned} \quad (3.6)$$

where \mathbf{w}_k is the process noise vector, and Φ_{GPS} is the system matrix (also defined in Section 2.4.1). The following notations were used:

$${}^r \mathbf{v}_k = \mathbf{H}_{GPS,k+1} \mathbf{w}_k + \mathbf{v}_{M,k} + \mathbf{v}_{RN,k+1} - \Psi_{GPS} \mathbf{v}_{RN,k} \quad (3.7)$$

and

$${}^r \mathbf{H}_{GPS,k} = \mathbf{H}_{GPS,k+1} \Phi_{GPS} - \Psi_{GPS} \mathbf{H}_{GPS,k} \quad (3.8)$$

The correlated noise vector $\boldsymbol{\varepsilon}_{M,k}$ cancels out in the pseudo-observation equation 3.6, thus ${}^r \mathbf{v}_k$ is a white sequence. All four terms on the right-hand-side of equation 3.7 are independent, which makes covariance computations straightforward.

Further calculations are necessary to eliminate the correlation that now exists between the pseudo-measurement noise ${}^r \mathbf{v}_k$ and the process noise \mathbf{w}_k . A pseudo-process equation is derived in Appendix D. Important practical details on the

interpretation of the filter's solution with respect either to the pseudo-measurement $r \mathbf{z}_k$ or to the actual measurement \mathbf{z}_k are also included in Appendix D.

Finally, when compared to a more traditional state augmentation method, the state efficiency of the measurement differencing filter is well worth the cost of a few complications in the implementation (storage of \mathbf{z}_{k-1} and $\mathbf{H}_{GPS,k-1}$ and initialization procedure [Bry68]). Indeed, when processing code and carrier phase measurements from a 12-channel dual-frequency receiver, a state augmented filter requires 48 extra states (which is the total number of potential GPS measurements). The proposed GPS algorithm has potential applications beyond this work since it performs the combined estimation of both position and cycle ambiguities at any update rate.

3.2.2 GPS/Laser Measurement Differencing EKF. For consistency, a measurement differencing equation akin to equation 3.6 is applied to the laser scanner data (for which $\Psi_{LAS} = \mathbf{0}$). With regard to state management routines, landmark states are treated differently than cycle-ambiguity states [Per97] because their value after landmark reacquisition does not change. Cycle ambiguity states are removed as soon as the corresponding satellite is out of sight, whereas landmark states remain in the system as long as the landmarks are within reach of the laser – a landmark can be temporarily hidden in noise or behind another landmark.

In summary, differential code and carrier phase measurements (respectively $\Delta \mathbf{p}$ and $\Delta \mathbf{\phi}$) as well as ranging and angular laser data (\mathbf{d} and $\mathbf{\theta}$) are fed into a unified measurement differencing EKF to simultaneously estimate the vehicle three-dimensional

position \mathbf{x}_{ENU} and its heading angle ψ , the differential GPS receiver clock bias $\Delta\tau$ and cycle ambiguities $\Delta\mathbf{N}$, and the landmark locations \mathbf{p} . The complete linearized laser-augmented GPS navigation system in matrix form is:

$$\begin{bmatrix} \mathbf{x}_v \\ \Delta\mathbf{N} \\ \mathbf{p} \end{bmatrix}_{k+1} = \begin{bmatrix} \Phi_v & \mathbf{0} \\ & \mathbf{I}_{n_s} \\ \mathbf{0} & & \mathbf{I}_{n_L} \end{bmatrix} \begin{bmatrix} \mathbf{x}_v \\ \Delta\mathbf{N} \\ \mathbf{p} \end{bmatrix}_k + \begin{bmatrix} \mathbf{u}_v \\ \mathbf{0} \\ \mathbf{0} \end{bmatrix}_k + \begin{bmatrix} \mathbf{w}_v \\ \mathbf{0} \\ \mathbf{0} \end{bmatrix}_k \quad (3.9)$$

where $\mathbf{x}_v = [\mathbf{x}_{ENU}^T \ \psi \ \Delta\tau]^T$, and

$$\begin{bmatrix} \Delta\mathbf{p} \\ \Delta\varphi \\ \mathbf{d}_L \\ \boldsymbol{\theta}_L \end{bmatrix}_k = \begin{bmatrix} \mathbf{E} & \mathbf{0} & \mathbf{1}_{n_s} & \mathbf{0} & \mathbf{0} \\ \mathbf{E} & \mathbf{0} & \mathbf{1}_{n_s} & \mathbf{I}_{n_s} & \mathbf{0} \\ \mathbf{F}_{d,x} & \mathbf{0} & \mathbf{0} & \mathbf{0} & \mathbf{F}_{d,p} \\ \mathbf{F}_{\theta,x} & -\mathbf{1}_{n_L} & \mathbf{0} & \mathbf{0} & \mathbf{F}_{\theta,p} \end{bmatrix}_k \begin{bmatrix} \mathbf{x}_{ENU} \\ \psi \\ \Delta\tau \\ \Delta\mathbf{N} \\ \mathbf{p} \end{bmatrix}_k + \begin{bmatrix} \boldsymbol{\varepsilon}_{M-\Delta\mathbf{p}} + \mathbf{v}_{RN-\Delta\mathbf{p}} \\ \boldsymbol{\varepsilon}_{M-\Delta\varphi} + \mathbf{v}_{RN-\Delta\varphi} \\ \mathbf{v}_d \\ \mathbf{v}_\theta \end{bmatrix}_k \quad (3.10)$$

where $\mathbf{E} = [-\mathbf{1}_e \ \dots \ -n_s \mathbf{e}]^T$.

The altitude x_U is assumed unknown but constant. The vehicle state transition matrix Φ_v is based on a straightforward kinematic model:

$$\dot{x}_E = -V_{N0} \sin(\psi), \quad \dot{x}_N = V_{N0} \cos(\psi).$$

Assuming a straight-line vehicle trajectory at a constant velocity V_{N0} , the model is linearized for small values of ψ , and discretized such that:

$$x_{E,k+1} = x_{E,k} - V_{N0} T_P \psi_k \quad \text{and} \quad x_{N,k+1} = x_{N,k} + u_{x_{N,k}}.$$

A deterministic constant reference input vector \mathbf{u}_v on the vehicle states is included in the process equation 3.9 to simulate the vehicle's displacement, so that:

$$u_{x_N,k} = V_{N0} \cdot T_p,$$

and the other elements of \mathbf{u}_v are zero. Due to the simple nature of this dynamic model, values for the vehicle process disturbances \mathbf{w}_v are large (the lack of knowledge on the time propagation of $\Delta\tau$ is also modeled by a very large process noise). Therefore, in this work, the role of the vehicle model is minimal, and the estimation process is based primarily on sensor information. The upcoming algorithm analysis will point out that as satellites and landmarks get in and out of sight, absolute position information is stored over time via constant parameters ΔN and \mathbf{p} , whose process noise in the state propagation equation (3.9) is zero.

Equations 3.9 and 3.10 constitute a state-space representation written in the form:

$$\mathbf{x}_{k+1} = \Phi \mathbf{x}_k + \mathbf{u}_k + \mathbf{w}_k \quad \text{and} \quad \mathbf{z}_k = \mathbf{H}_k \mathbf{x}_k + \mathbf{v}_k, \quad (3.11)$$

where the elements of \mathbf{v}_k corresponding to GPS measurements are time-correlated.

The non-linear measurement equations 3.2 and 3.3 are used in the estimation process. As a result, the measurement differencing EKF equations can be written in the form:

$$\begin{aligned} \hat{\mathbf{x}}_{k-1|k} &= \hat{\mathbf{x}}_{k-1|k-1} + \mathbf{K}_k \left({}^r \mathbf{z}_k - {}^r \mathbf{h}(\hat{\mathbf{x}}_{k-1|k-1}, \hat{\mathbf{x}}_{k|k-1}) \right) \\ \hat{\mathbf{x}}_{k|k} &= \Phi \hat{\mathbf{x}}_{k-1|k} + \mathbf{D}_k \left({}^r \mathbf{z}_k - {}^r \mathbf{h}(\hat{\mathbf{x}}_{k-1|k}, \Phi \hat{\mathbf{x}}_{k-1|k} + \mathbf{u}_k) \right) + \mathbf{u}_k \\ \hat{\mathbf{x}}_{k+1|k} &= \Phi \hat{\mathbf{x}}_{k|k} + \mathbf{u}_k \end{aligned} \quad (3.12)$$

where $\hat{\mathbf{x}}_{k|j}$ designates the best estimate of \mathbf{x}_k knowing \mathbf{z}_j , the matrix \mathbf{D}_k is defined in Appendix D when deriving the pseudo-process equation ($\mathbf{D}_k = \mathbf{W} \mathbf{H}_k^T {}^r \mathbf{V}^{-1}$), and:

$${}^r \mathbf{h}(\hat{\mathbf{x}}_{k-1|k-1}, \hat{\mathbf{x}}_{k|k-1}) = \left[\left({}^r \mathbf{H}_{GPS,k} \hat{\mathbf{x}}_{k-1|k-1} + \mathbf{H}_{GPS,k} \mathbf{u}_k \right)^T \quad \left(\mathbf{h}_{LAS}(\hat{\mathbf{x}}_{k|k-1}) \right)^T \right]^T.$$

The elements of $\mathbf{h}_{LAS}(\hat{\mathbf{x}}_{k|k-1})$ are the right hand side terms of equations 3.2 and 3.3, and \mathbf{H}_{GPS} and \mathbf{H}_{GPS} are the rows of the pseudo-observation and observation matrices corresponding to GPS measurements (derived using equations 3.7, 3.8 and 3.10). This non-linear state-space representation is implemented in direct simulations and in experiments to update and propagate the state vector in the estimation process as well as in the data association procedure.

3.3 Covariance and Monte-Carlo Analyses

Performance analyses for two scenarios shed light on different aspects of the GPS/laser navigation system. Models for the two scenarios are pictured in Figure 3.8 (they are later tested in this structured environment). In the forest scenario, the two sensors essentially relay each other with seamless transitions from open-sky through GPS-denied areas where tree trunks serve as landmarks. In urban canyons, the full extent of the measurement-level integration is exploited since both GPS and laser measurements simultaneously contribute to generate trajectory estimates, while individually, neither sensor might be capable of providing a precise position fix.

The use of a two-dimensional laser scanner requires that altitude be assumed constant. In this case, three GPS signals are necessary to solve for the horizontal position and GPS receiver clock bias $\Delta\tau$. When less than three satellites are available and more than one (due to the undetermined $\Delta\tau$), the output of a position-domain algorithm is based solely on laser observations. Therefore, differences between the measurement and position-domain implementations appear when two satellites are in view, which occurs frequently in urban canyons as discussed in the upcoming Section 3.3.2.

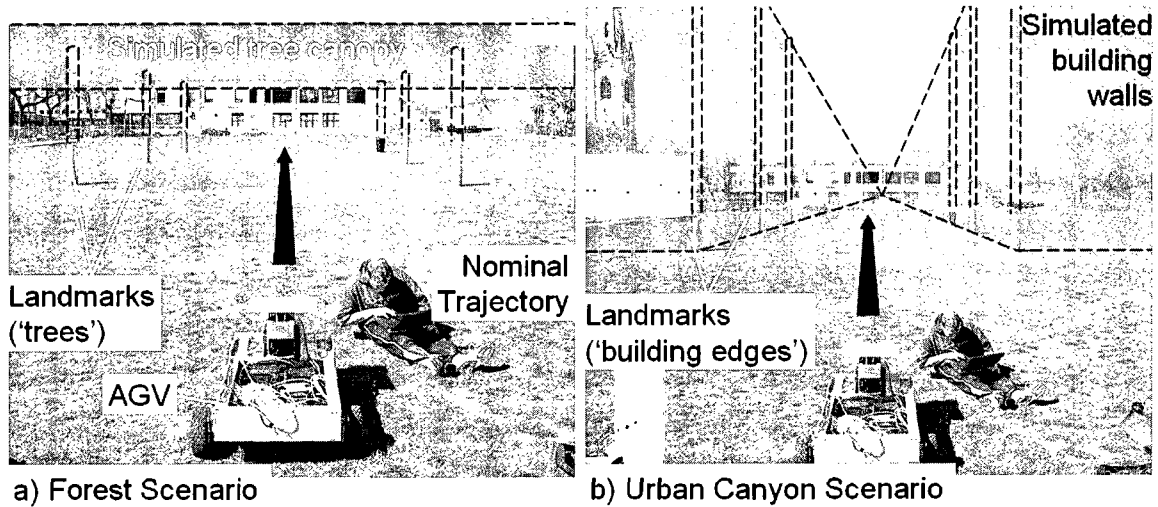


Figure 3.8. Experimental Setup and Artificial Satellite Blockage Models

Performance results are highly dependent on landmark and satellite geometry. The analysis methodology therefore relies on comparisons for fixed geometries, between range-domain and position-domain approaches, and between covariance and Monte-Carlo analyses. Covariance results are directly obtained using the linearized model of equations 3.9 and 3.10. They quantify the performance of the estimation process, assuming successful feature extraction and data association. Thus, covariance results are a measure of the best-case system performance. In order to include the effects of the extraction and association procedures, the non-linearity of the measurement equation and the uniformly distributed impulse noise present in raw laser scans, direct simulations of the entire system are performed over numerous trials using equation 3.12.

3.3.1 Roving Across GPS-Denied Areas: The ‘Forest Scenario’. Autonomous ground vehicles (AGV) are particularly well suited for landmine detection and removal because of the dangerous, tedious and repetitive nature of the task [Bos04]. Minefields

include wooded environments in which GPS is unavailable, hence this ‘forest scenario’. For this simulation, tree trunks are assumed to be vertical cylinders. The GPS satellite blockage due to the tree canopy is modeled using a horizontal plane on top of these cylinders. Low-elevation satellite signals penetrating inside the forest are rejected because such observations would be affected by multipath reflections on tree trunks.

The example in Figure 3.9 illustrates the interactions between the two sensors during the mission. Three successive snap-shots (a, b, and c) of a direct simulation show the vehicle roving across a forest. On the upper part, azimuth-elevation plots and simulated laser scans present respectively the GPS satellite sky blockage due to the forest, and the trees within range of the laser. The result of the estimation process is given on the lower part. Covariance ellipses represent the positioning error on the vehicle and landmarks.

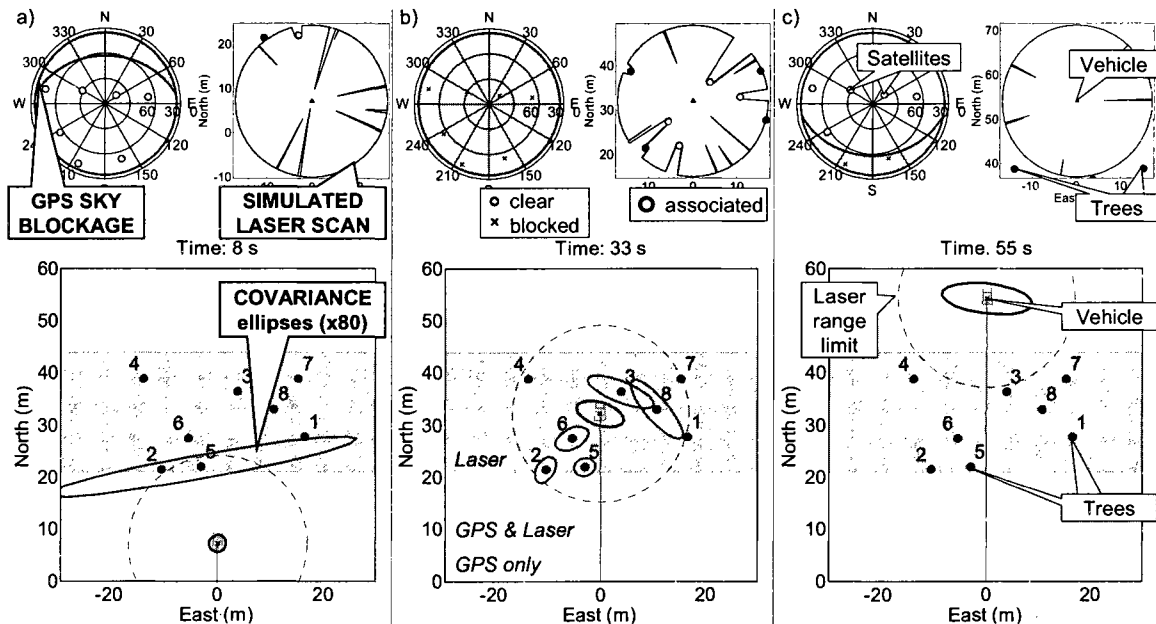


Figure 3.9. Direct Simulation of the GPS/Laser Algorithm in the ‘Forest Scenario’

The mission starts with the AGV operating in a GPS available area. The many satellite signals available during this initialization enable accurate estimation of cycle ambiguities, so that the vehicle positioning uncertainty does not exceed a few centimeters.

In Figure 3.9a, the vehicle enters the transitional GPS-and-laser-available area (fair-shaded). There are still more than three satellites available, so that the vehicle's position is accurately determined. A first landmark is within range of the laser scanner. Using GPS only (in the absence of a reliable dynamic model or heading sensor), the vehicle's attitude is unknown. This is why the laser's angular measurement is of little use for the tree's absolute position estimation, and it explains the shape of the ellipse. Over time, as the system collects redundant observations for this landmark together with absolute GPS measurements, the landmark position estimate improves steadily (similar to case (c) in Figure 3.7, but here external information is provided by GPS).

In Figure 3.9b, the vehicle is in the middle of the forest. Once the AGV has reached the dark-shaded area where no satellite signals are available, the rover's cross-track deviation (resulting from laser-based SLAM) increases with distance (case (d) in Figure 3.7). However, in this case, tree trunks at the entrance of the forest could be precisely located using both CPDGPS and lasers while the AGV was passing through the transitional area. Therefore in the dark-shaded area, measurement redundancy and changes in geometry due to rover motion help improve the relative position estimates between landmarks, and therefore the transmission of the absolute positioning information. The latter propagates in time through constant landmark coordinate states, as previous landmarks get out of laser range and new ones become available.

Finally, in Figure 3.9c, the vehicle is back into a GPS available area, and the cross-track deviation drift is stopped. The positioning performance results from a combination of (1) unambiguous GPS code measurements and (2) the remainder of the pre-obstruction absolute positioning solution, propagated via constant landmark states to constant carrier phase cycle ambiguities within the second transitional area. Subsequent filtering of GPS measurements over time will bring the cycle ambiguities and vehicle position estimates back to their initial accuracy, before originally entering the forest.

To further investigate the individual effects of the model's parameters, we conduct a sensitivity analysis with respect to a nominal configuration (given at the bottom of Table 3.1). The performance criterion is the cross-track deviation at the exit of the laser-only (dark-shaded) area where the value of the estimated error is usually close to its maximum. Covariance analysis assuming flawless extraction and association, and Monte-Carlo simulations over 100 trials are carried out to respectively evaluate the effectiveness of the estimator, and the added error due to the extraction and association.

Table 3.1. Sensitivity Analysis: Cross-track Deviation Results (1 sigma, in m)

Configuration	Covariance	Monte-Carlo
Nominal*	0.095	0.175
Laser range Limit = 20m	0.057	0.148
AGV velocity: $V_{N0} = 3\text{m/s}$	0.139	0.394
Tree density = 0.003 tree/m^2	0.123	0.198
Sample time: $T_p = 1.5\text{s}$	0.172	0.372
Using a magnetometer	0.076	0.083
Tree height = 5m	0.0924	0.147

* range limit = 15m, tree density = 0.015 tree/m^2 , $V_{N0} = 1\text{m/s}$, $T_p = 0.5\text{s}$, forest depth = 100m, no magnetometer, tree height = 10m

Results listed in Table 3.1 show that a larger laser range-limit generates more measurements hence better positioning accuracy. A higher vehicle velocity, a lower tree density and a lower sampling rate have the opposite effect. Significant improvement is gained from the use of an example magnetic compass with a 1deg standard deviation (commercially available), especially in limiting extraction and association failures (most of the improvement in the Monte-Carlo results). As mentioned earlier, SLAM is usually performed in conjunction with dead-reckoning sensors; they are left aside in this work to emphasize the benefits and limitations of GPS-augmentation. Although the performance values for the Monte-Carlo simulation are expectedly worse because of the added errors in the extraction and association, the trends highlighted with the covariance analysis are all confirmed.

In Figure 3.10, the performance is evaluated against the length of the GPS outage. Monte-Carlo simulations exhibit a sharp increase in cross-track error for forest-lengths larger than 300 meters. This is to be anticipated because, as explained in Appendix B, failures in the innovation-based nearest-neighbor data association process are more likely to occur when the vehicle position error increases. Still, the laser/GPS navigation system extends the availability of sub-meter navigation solutions hundreds of meters beyond non-laser-augmented systems.

Finally, the explanation of Figure 3.9b pointed out that the uncertainty on the position of trees when entering the laser-only area determines the vehicle positioning accuracy throughout the GPS outage. Now, the tree height defines the GPS elevation mask, and hence the frontiers of the transitional GPS-and-laser-available area. The larger the transitional area, the lower the uncertainty on the trees locations. Therefore better

results are obtained in forests with lower trees and using lasers with a larger range-limit. To further study the navigation performance in this transitional area where both GPS and laser measurements are available, an ‘urban canyon scenario’ is considered.

3.3.2 Exploiting Additional Satellite Signals: The ‘Urban Canyon Scenario’.

Accurate GPS position solutions are rarely available in urban canyons or forest roads because of the severe sky-blockage caused by bordering buildings and trees. The distinctive advantage of the measurement-level integration is best illustrated here since the estimation process makes use of GPS signals that alone would be too few to generate a position fix. This sub-section aims at quantifying the navigation improvement brought by two additional GPS signals as compared to a position-domain integration.

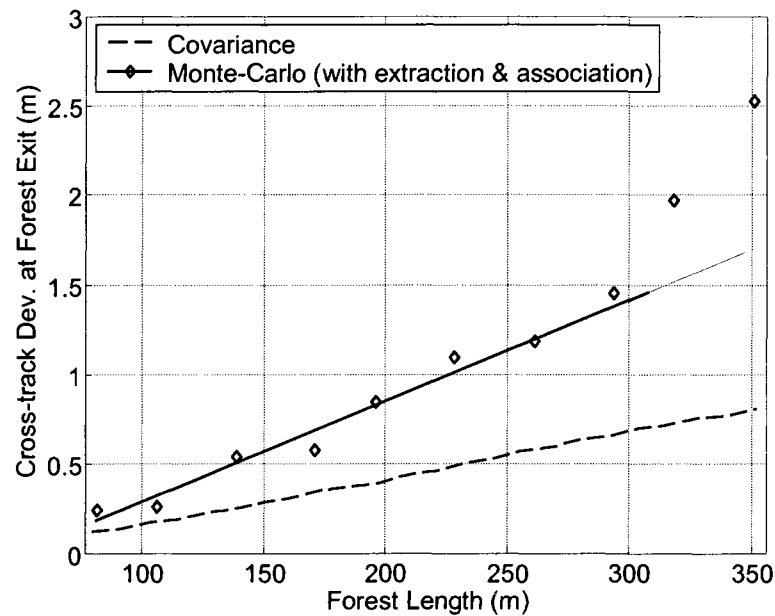


Figure 3.10. Performance Versus Length of the GPS-Outage

Buildings are modeled as regularly spaced blocks along the vehicle trajectory. They generate sky blockage for GPS observations, and laser measurements are extracted at their edges. The assumption is made that signals with a clear line of sight are not corrupted despite potential multipath interferences in real-life situations.

First, a satellite visibility analysis is performed. It quantifies for an urban environment the likelihood of having only two satellites in view (in which case the measurement-level integration makes a decisive difference). The number of visible satellites for a stationary AGV is determined at one minute intervals over a 24 hour period (period over which the GPS satellite geometry repeats itself). The selected location is Chicago. The operation is repeated for different street orientations (in increments of 45deg), and for five different positions with respect to the center of the street (to recreate different traffic lanes).

The resulting composite satellite availability reveals for example, that for a street width of 30 m and building heights of 50 m, GPS position fixes (based on three or more satellite signals) are available in only 15% of the cases. In 40% of cases, there are two satellites available: these are left unused with non-augmented GPS and with position-domain implementations, but can be exploited in the measurement-level integration. GPS does not contribute for the remaining 45% of cases where one or no signal is available (more detailed results are reported in [Joe06b]). Even in this last case, and for a moving vehicle, frequent opportunities may arise where a second satellite comes in sight (e.g., at crossroads), which can be exploited with the measurement-level algorithm to enhance the overall positioning performance.

Next, a Monte-Carlo simulation is carried out for a nominal urban canyon scenario: the rover starts in an open-sky area, and advances northwards at a 3m/s constant velocity (slightly faster than 10km/hr) in the center of a 30-meter wide street surrounded by 50-meter tall buildings, whose edges are regularly spaced in 25-meter intervals along the trajectory. For simplicity, the sky-blockage conservatively assumes continuous walls (no intersections). In the example shown in Figure 3.11, the number of satellites in view quickly drops to two and remains so for the rest of the mission, but laser measurements to buildings' edges become available.

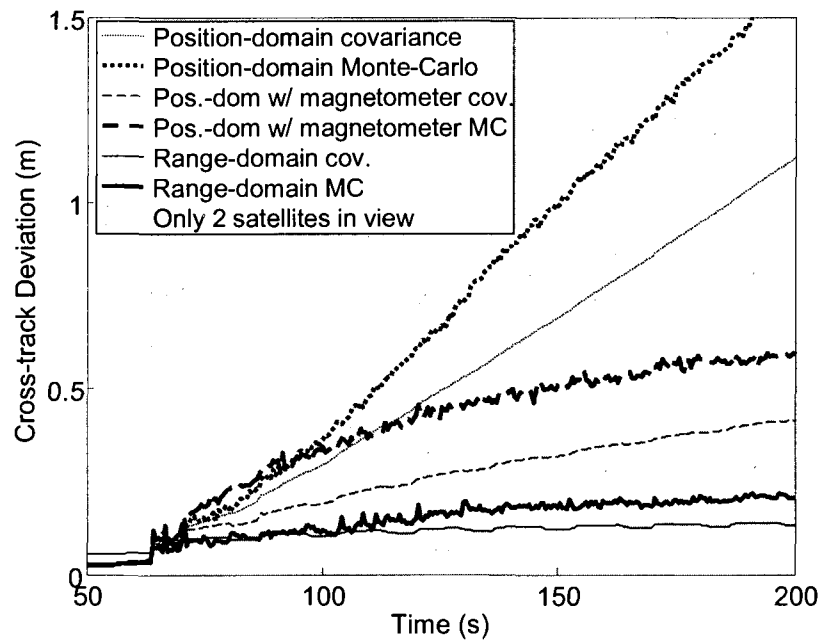


Figure 3.11. Comparison of Three Implementations for the Street Scenario

Results over 100 trials establish the positioning performance versus time for three types of implementations. For the position-domain approach, the laser-based solution drifts very rapidly (similarly to case (d) in Figure 3.7), even with added magnetometer data. In the case of the measurement-level integration however (and without using a magnetometer), the two absolute GPS signals available are enough to limit the drift, hence enabling to sustain precise absolute positioning. Covariance results exhibit the same trends, demonstrating that this difference in performance is not to be attributed to the selected extraction and association routines. The dramatic change in results illustrates the significant advantage of the range-domain integration over position-domain algorithms, which is further investigated using experimental data.

3.4 Experimental Testing

Experiments are carried out first, in a structured environment to evaluate the performance of the estimator, and then in actual urban canyons to assess the overall system efficiency under high risk of miss-association.

3.4.1 Miss-Association-Free Testing in a Structured Environment. The first set of data is collected in a structured environment (shown in Figure 3.8). Static simple-shaped landmarks are located at locations sparse enough to ensure successful outcomes for the extraction and association. Because the results presented here are free of miss-associations, they describe the estimation process.

In order to obtain a full 360deg laser scan, two 180deg laser scanners are assembled back-to-back, with a specified 15-80 m range limit, a 0.5deg angular

resolution, a 5 Hz update rate and a ranging accuracy of 1-5 cm (1 sigma) [SIC06]. The GPS antenna is mounted on top of the front laser. The lever-arm distance between the two lasers is included in the measurement model. The two lasers and the GPS antenna are mounted on an existing AGV platform equipped with a dual-frequency GPS receiver. An embedded computer onboard the vehicle records all measurements including the raw GPS data from the reference station transmitted via wireless spread-spectrum data-link. Synchronization and measurement projections on a common reference sample time of 0.5s are realized using the computer's clock. Truth vehicle trajectory and landmark locations are obtained using a fixed CPDGPS solution. Because there is actually no physical obstruction to the sky, satellite masking for the GPS/laser integration system is performed artificially using the same model as in the previous direct simulation (represented in Figure 3.8). Tree trunks or building edges are reproduced using five cardboard columns and one dark plastic garbage can.

Results for the miss-association-free forest scenario are given in Figure 3.12. Figures 3.12b and 3.12c expose the complementary availability of the sensors' observations: landmarks become available as space vehicles (SVs) go out of sight. As a consequence, smooth transitions between open-sky and GPS-unavailable areas are achieved. The position error does not exceed 15 cm in spite of 35 meters of GPS outage (average vehicle speed was 0.8 m/s). Covariance envelopes are now dependent on feature extraction. It is interesting to note that, in spite of its larger diameter, the dark plastic garbage can was tracked by the laser scanners over a significantly shorter period of time than the cardboard columns. This is explained by the difference in materials and colors [Ye02]. The performance of the measurement-level integration (Figure 3.12a)

differs only slightly from the position-domain implementation because in this scenario, the system transitions quickly from an open-sky area to complete GPS-signal blockage.

Greater differences emerge in the urban canyon scenario, which is tested using the same set of data. Instead of artificially performing the satellite masking corresponding to a forest, the blockage model representative of an urban canyon is implemented. The results shown in Figure 3.13 demonstrate that as soon as there are fewer than three satellites in view, the range-domain integration surpasses the position-domain implementation. In spite of 30 meters of GPS outage, the position error for the measurement-level algorithm does not exceed 10 cm.

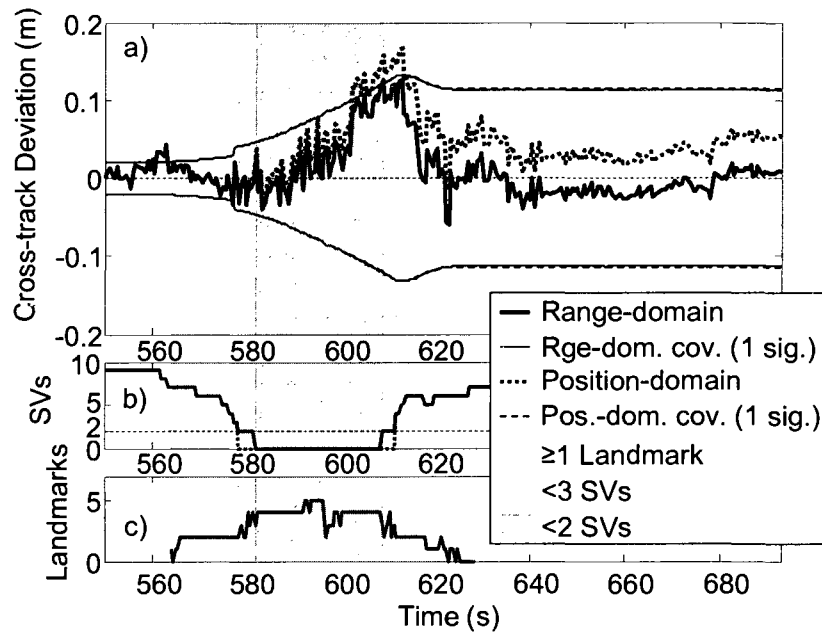


Figure 3.12. Experimental Result for the Forest Scenario

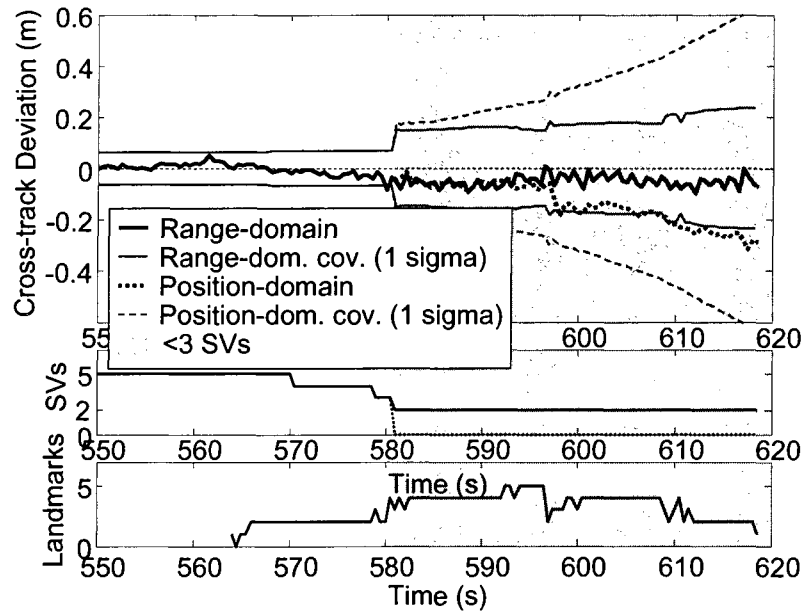


Figure 3.13. Experimental Result for the Miss-Association-Free Urban Canyon Scenario

3.4.2 Testing in a Natural Environment, in the Streets of Chicago. Experiments in a natural environment serve two main purposes: (1) they provide a measure of the system performance when implemented in a realistic mission; (2) they help quantify the improvement brought by two additional GPS signals when miss-extraction and miss-association of laser measurements are occurring.

In the two experiments presented here, the laser scanners and GPS antenna are mounted on a car, which is driven into an alley or a street (Figure 3.14). The first test takes place in a narrow alley, in one of Chicago's oldest neighborhoods. As pictured earlier in Figure 3.4, the diversity and geometry of the landmarks make extraction and association extremely challenging. All but two GPS signals were actually blocked during most of the experiment, so that the precise fixed CPDGPS position solution could not be used to generate the truth trajectory. Instead, interpolation between occasional GPS position fixes was achieved using the vehicle kinematic model described in Section 3.2.2.

A second set of data was collected in a wider street bordered by better-defined, newly constructed buildings, in which fixed CPDGPS truth position updates were available. In that case, satellite masking due to 50-meter high buildings was artificially introduced.

The estimated landmark locations for the first set of data are superimposed with a satellite image of the alley in Figure 3.5. Unlike for the position domain implementation, the vehicle trajectory established using the range-domain algorithm remains within the narrow alley, and landmarks match buildings' edges and edges of garage doors.

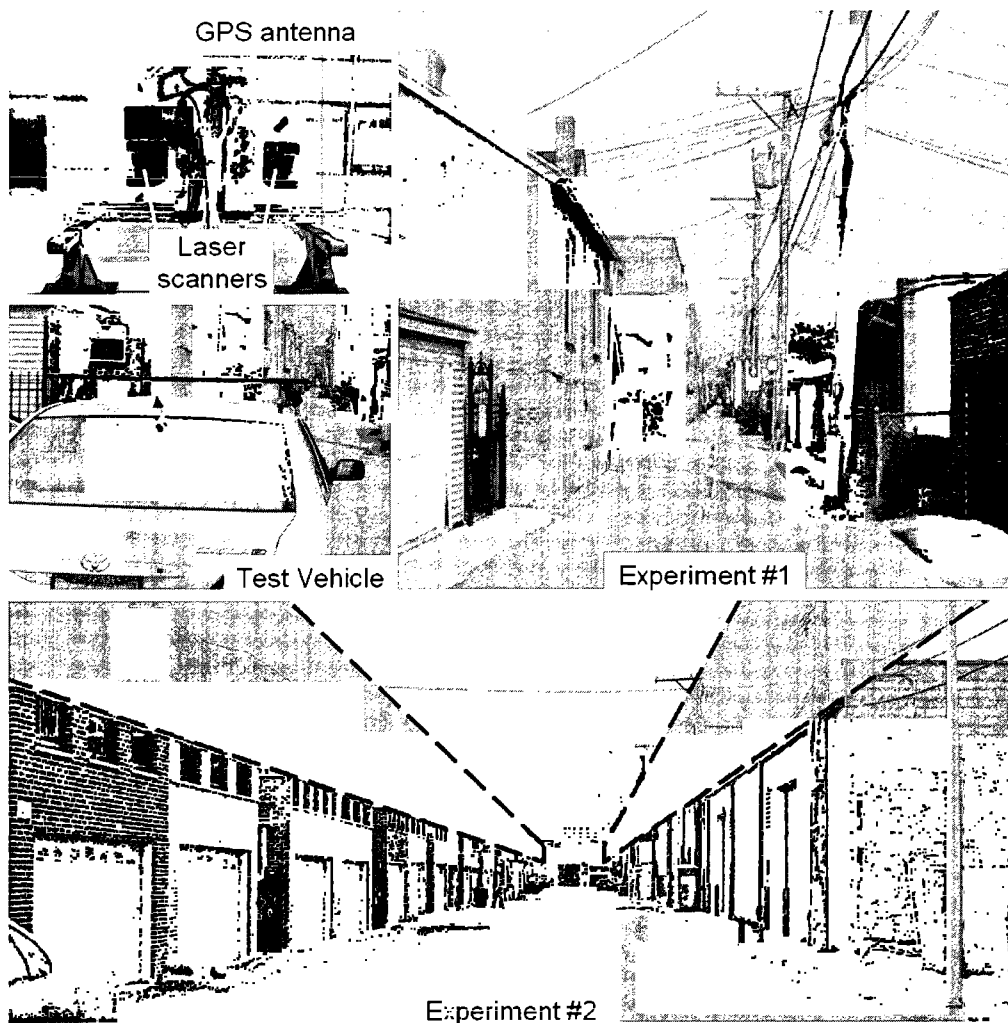


Figure 3.14. Experimental Setup for the Testing in the Streets of Chicago

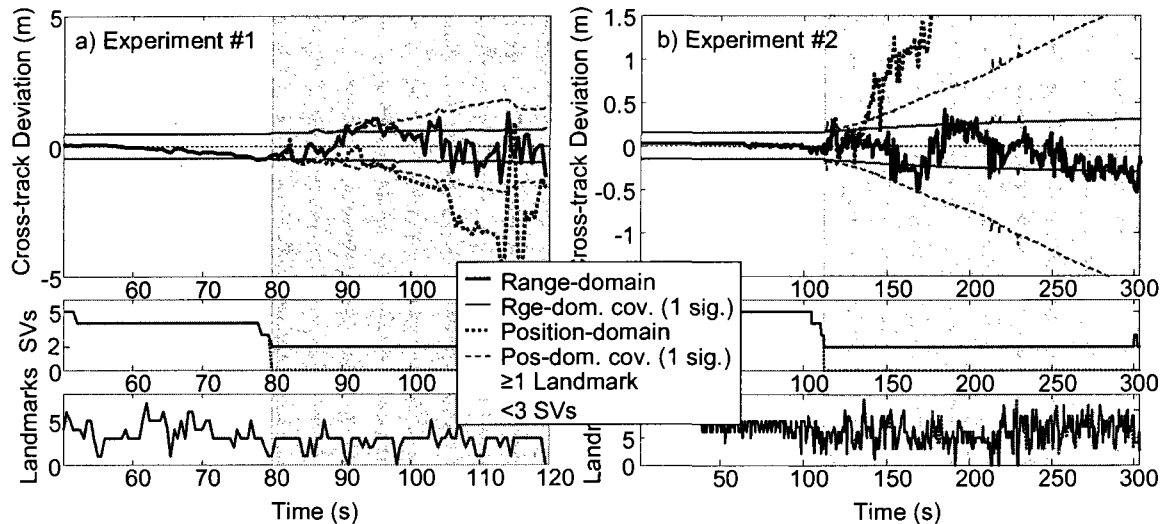


Figure 3.15. Experimental Results for Tests Conducted in the Streets of Chicago

Lateral errors for both experiments are plotted in Figures 3.15. For the position-domain implementation, cross-track position errors do not match the covariance envelopes: they quickly grow without bound which is a clear indication of catastrophic navigation errors due to miss-associations. In contrast, position deviations and covariance results are fairly consistent for the range-domain algorithm, although landmarks can not always be identified (miss-extractions and non-catastrophic miss-associations). There are even occurrences where the number of associated landmarks drops to zero. In these cases, poor performance is expected because the vehicle position estimate is based on the straightforward linearized kinematic model included in the algorithm.

In spite of these conditions, the two absolute GPS ranging observations exploited with the measurement-level integration provide robustness to recover from failures in the extraction and association routines. As a result, in the first experiment, the absolute positioning error does not exceed 1.5 m over 70 meters of travel distance without a GPS

position fix, for an average vehicle speed of 1.5 m/s. Better than 0.5 m of cross-track deviation is achieved in the second case, in spite of 3 min without GPS position fix.

3.5 Summary of the GPS/Laser Integration

Laser-augmented CPDGPS greatly increases the availability of accurate navigation solutions for outdoor ground vehicles. The proposed algorithm integrates the two sensors at the measurement level and enables simultaneous estimation of vehicle and obstacle locations, as well as GPS carrier phase cycle ambiguities. This approach optimizes the transmission of *absolute* positioning information for continuous seamless high-accuracy navigation across GPS-denied environments. Also, in partially obstructed GPS areas, the measurement-level integration exploits satellite signals that are not usable in other implementations, by utilizing additional laser observations. The enhanced positioning performance has been consistently quantified using covariance analysis, Monte-Carlo simulations and experimental testing.

Laser-based navigation in natural environments is extremely difficult because it depends on the outcome of the challenging data association problem. Experimental data collected in both a structured environment and in actual urban canyons demonstrate that the use of two additional absolute satellite signals not only improves the estimation process, but also helps recover from miss-associations. Thus, measurement-level augmentation of laser-based positioning using GPS improves the robustness of SLAM procedures and alleviates the need for elaborate extraction and association algorithms.

Overall, the reciprocal benefits of the two sensors are employed in the integrated system to achieve considerable increases in accuracy, continuity and availability of the final navigation solution.

In the next chapters of this dissertation, a LEO satellite-augmented GPS system named iGPS is investigated. It aims at fulfilling some of the most severe navigation requirements specified for civilian transportation applications. For such life-critical missions, integrity requirements are particularly demanding. The predominant concern for integrity impacts every stage of the system design, starting with the navigation system infrastructure, which determines the measurement errors.

CHAPTER 4

IGPS SYSTEM DESIGN, MEASUREMENT ERROR AND FAULT MODELS

CPDGPS applications investigated and referenced in Chapters 2 and 3 repeatedly demonstrated high-accuracy positioning performance. However, this performance was limited to the area surrounding the differential reference station and was conditioned upon correct cycle ambiguity resolution, which could take several tens of minutes. In contrast, the following Chapters 4 to 6 will show that the combination of ranging measurements from GPS and from fast-moving LEO Iridium satellites makes real-time high-integrity carrier phase navigation achievable within a few minutes, and at global scales.

Chapter 4 introduces assumptions on the iGPS system architecture that serve as bases for the algorithms and analyses of Chapters 5 and 6. Section 4.1 describes the existing Iridium constellation and presents the envisioned ground and user segments designed to enable reliable precision navigation. Models for the residual measurement errors (after ground corrections) are then established under normal fault-free (FF) conditions in Section 4.2, and for single satellite faults (SSF) in Section 4.3. Finally in Section 4.4, both ground and user measurement monitoring systems are discussed, and the overall system integrity requirement is allocated between FF and SSF hypotheses for fault-detection at the user receiver.

4.1 Envisioned iGPS System Architecture

iGPS is intended for single-frequency civilian applications and aims at servicing wide-areas with minimal ground infrastructure. As part of this work, a nominal

navigation system configuration is proposed that was iteratively refined as a result of simulated performance sensitivity analyses (Chapter 6).

4.1.1 Space Segment: Joint GPS and Iridium Constellation. The GPS constellation is described in Section 2.1.1.

The Iridium telecommunication satellite constellation owes its name to the 77th element of the periodic table because it was originally designed to include 77 SVs. The number was decreased to 66 in order to optimize spacecraft coverage and to reduce cost. A full Iridium constellation was first deployed in 1998 [Fos98]. Telecommunication satellite clocks don't meet the atomic standard, but it has been demonstrated that their clock drift can be effectively modeled and corrected using GPS measurements at the user receiver [Rab00].

Iridium's primary function is to provide telecommunication capabilities to users worldwide, particularly in remote places where other communication means are unavailable. Messages are exchanged between users and satellites and satellite-to-satellite cross-links enable uninterrupted communications so that any two points on the globe are connected. Continuous global coverage is realized using spacecraft orbiting at an altitude of 780km, which is much lower than the 20,000km GPS orbit altitude. As a result, a spacecraft spends on average 10min in view of a given location on the surface of the earth, and circles the earth in a period T_{IRI} of 100min 28s [Kid04]. As illustrated in Figure 4.1, the 66 satellites are distributed among 6 planes in near-circular orbits at 86.4deg inclination. A 31.6deg angle separates each co-rotating orbital plane, and the remaining 22deg angle separates the two planes at the seam of the constellation, where

spacecraft are counter-rotating [ICA07]. Each plane contains 11 regularly spaced satellites, whose positions are offset from SVs in the adjacent co-rotating plane by one-half of the satellite spacing.

As a consequence of the constellation design, the satellite density is much higher near the poles than at lower latitudes. For example, the average number of Iridium SVs visible at any instant is 2.2 in Chicago and 1.8 in Miami. In addition, the spacecraft trajectories generate larger North-South LOS variations relative to a ground observer than East-West. Accordingly, the horizontal carrier phase positioning performance is heterogeneous and higher precision is generally achieved for the North coordinate.

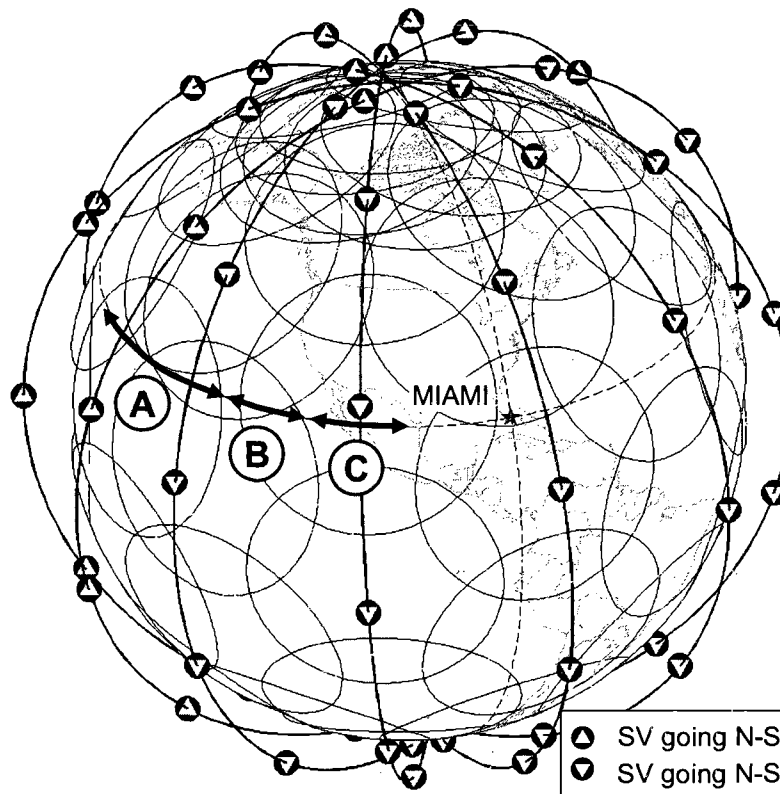


Figure 4.1. Iridium Satellite Coverage

In this work, the possibility of expanding the Iridium space segment was also considered with a modified 88 Iridium satellite constellation. In this case, 8 orbital planes are separated by a 23deg angle, leaving 19deg at the seam of the constellation. The resulting increased average spacecraft numbers over Chicago and Miami are respectively 3 and 2.4.

Further investigations are carried out for a joint GPS/Iridium/GlobalStar constellation. GlobalStar is comprised of 48 satellites arranged in 6 regularly spaced orbital planes of 8 satellites each, with 56deg inclination and an orbital period of about 114min. Continuous coverage for GlobalStar is realized between 70S-70N latitude, which is complementary with Iridium's satellite distribution (denser near the poles). Finally, GEO satellites used in WAAS and EGNOS provide ranging signals in addition to measurement error corrections. The contribution of single-frequency code and carrier measurements from three GEO spacecraft covering part of CONUS (as shown in Figure 2.7) is also evaluated in Chapter 6.

The nominal 24 GPS satellite constellation described in Section 2.1.1 is pictured in Figure 4.2a together with the 66 Iridium SVs. The constellations' orbital planes are quasi-stationary in an earth-centered inertial (ECI) frame, whose origin is the center of the earth and whose axes are fixed with respect to the stars. Satellites travel along the orbits, while the earth rotates about its North-South axis. Figure 4.2b shows from the point of view of a user at the Miami location, the tremendous difference in accumulated angular variations between GPS and LEO satellites over a 10min period. In parallel for the same location and duration, an azimuth-elevation sky plot underscores again the difference in spacecraft motion, and the North-South directionality of Iridium satellites.

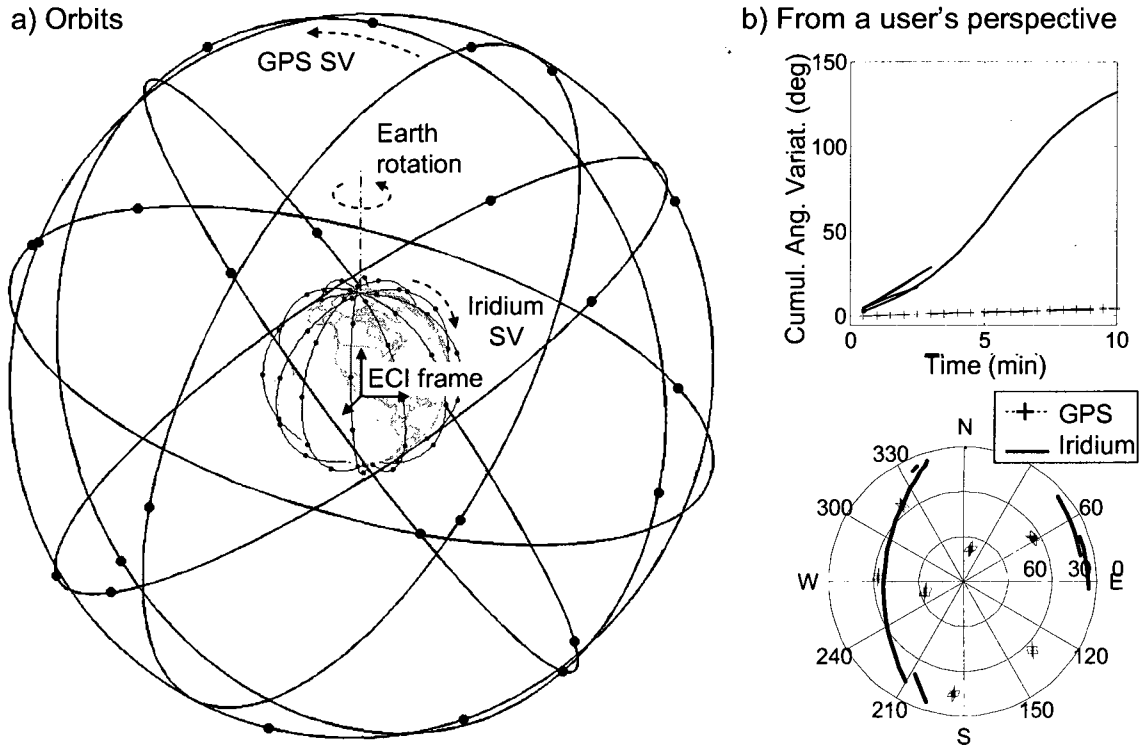


Figure 4.2. Joint GPS and Iridium Constellations

A quantitative measure of the difference between the two constellations is given by the satellites' angular velocities as perceived by an observer on earth. Let ${}^s\mathbf{e}_k$ be the 3×1 unit LOS vector (in a local reference frame) for satellite s epoch k . Over a short sampling period T_p (here, $T_p = 30\text{s}$), the angular rate between epochs $k-1$ and k is evaluated as:

$${}^s\omega_k = \cos^{-1} \left({}^s\mathbf{e}_{k-1}^T {}^s\mathbf{e}_k \right) / T_p .$$

The ratio of ${}^{IRI}\omega_k$ for Iridium SVs over ${}^{GPS}\omega_k$ for GPS satellites is the angular rate ratio (${}^{IRI}\omega_k$ and ${}^{GPS}\omega_k$ can be averaged over all visible Iridium and GPS satellites, respectively). It is evaluated every 30s over a 3day period to compute the average ratio. The resulting quantity equals to approximately 30 (it barely varies with location). In

other words, from a user's perspective, Iridium satellites move 30 times faster than GPS. This fundamental characteristic is exploited in the estimation process of Chapter 5 for fast cycle ambiguity resolution.

4.1.2 Envisioned iGPS Ground Segment. As described in Section 2.1.2, the primary function of the twelve GPS OCS ground monitoring stations is to make satellite position and time synchronization information available to users. A similar architecture is assumed for Iridium satellites. Although, unlike GPS, Iridium spacecraft can't be continuously tracked by ground stations, they are visible several times a day.

Precision navigation requires that additional information be transmitted, in particular to correct for errors due to refraction in the ionosphere. Unlike clock errors that have similar effects for all ground stations within a satellite's footprint, orbit ephemeris errors and, to a greater extent, ionospheric disturbances vary with receiver location. Indeed, the LOS to the receiver determines the section of the atmosphere crossed by the signal. Differential approaches described in Section 2.4 can be employed to mitigate ionospheric effects.

In this work, the conceptual iGPS ground segment consists of a network of ground reference stations (illustrated in Figure 4.3), whose density determines the accuracy of ionospheric corrections. In a first attempt to determine the overall system performance, iGPS ground stations are assumed co-located with the WAAS reference stations, whose correction accuracy has been documented over the past five years [NST03]. WAAS-like ionospheric delay estimates and long-term GPS satellite error corrections are derived at a master station (e.g., following the algorithm outlined in

reference [Wal00]) using dual-frequency measurements collected at ground reference stations, and broadcast to the user via Iridium communication channels.

Moreover, Iridium's communication capability greatly expands the potential to transmit data, which is severely limited for both GPS and WAAS (whose data rates are 50bps and 250bps respectively). This feature is exploited in Section 4.2 by considering precise Iridium clock and ephemeris data (assuming more numerous, more frequently updated orbital and clock parameters). Iridium's high-throughput communication could bring even further improvement if used to broadcast ionospheric and GPS clock and orbit ephemeris corrections (for now, a nominal 250bps data rate is assumed, which limits the WAAS correction resolution as noted for the IVDE in Section 2.4.2).

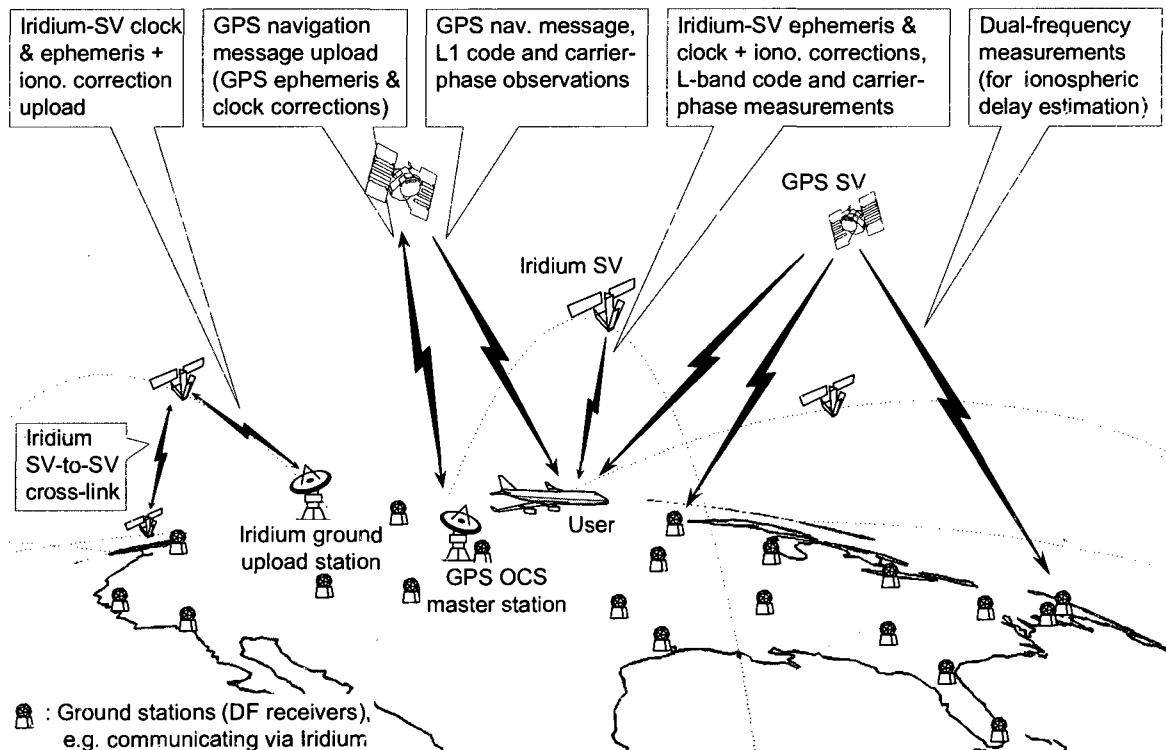


Figure 4.3. Conceptual Overview of the Assumed iGPS Architecture

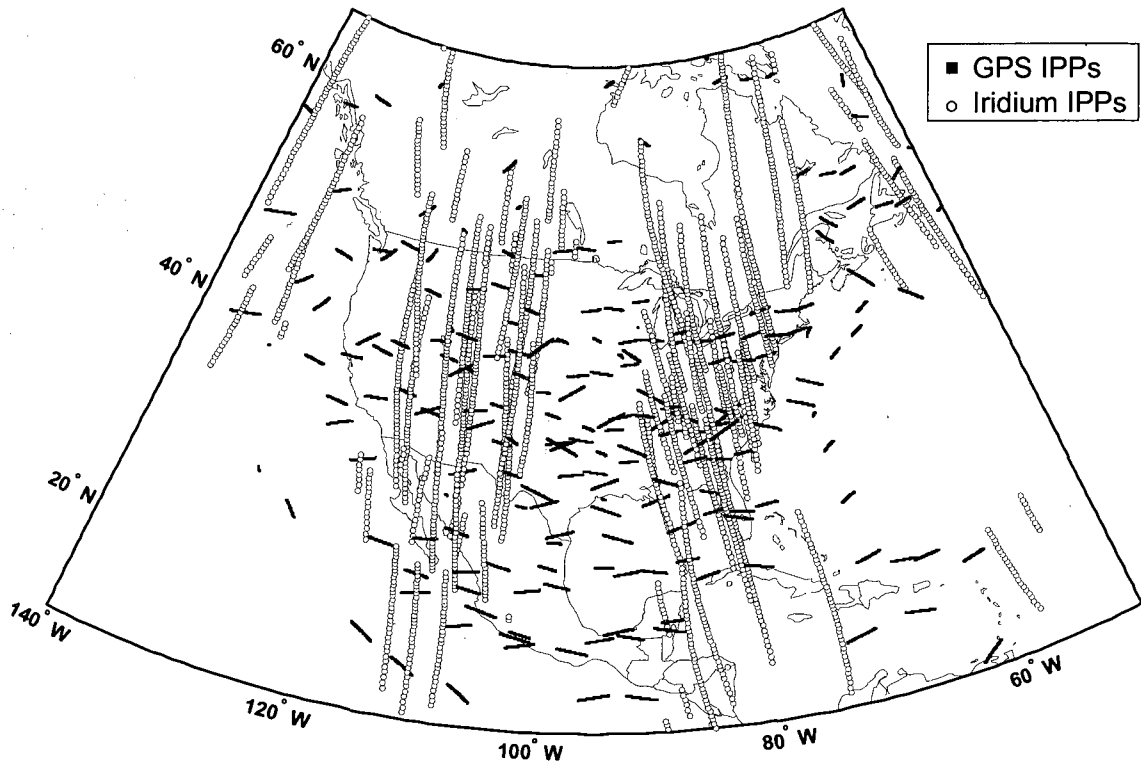


Figure 4.4. Iridium and GPS IPPs in an ECSF Frame over 10min

Finally, dual-frequency Iridium measurements collected at ground reference stations could improve the sampling of the ionospheric shell (this concept was introduced for WAAS in Section 2.4.2). These measurements are localized at ionospheric pierce points (IPPs), defined as the intersection between the station-to-satellite LOS and the height at which most of the ionosphere electrons are concentrated (i.e., approximately 350km). With the current WAAS ionospheric delay estimation algorithm performed as a snapshot implementation [Wal00], additional Iridium observations would only bring marginal improvement (on average, two extra IPPs per reference station added to about seven GPS IPPs). However, if the ionospheric shell is assumed constant over a short 10min period in an earth-centered sun-fixed (ECSF) frame, then the IPP sampling using

fast moving LEO satellites is dramatically improved in large sections of the sky, as displayed in Figure 4.4. This aspect of the ground architecture is beyond the scope of this work, but deserves further investigation in future work.

Measurement monitoring by the ground and user segments is addressed later in Section 4.4.

4.1.3 iGPS User Segment. The user segment is composed of all GPS/Iridium receivers. The iGPS concept described in this work is intended for civilian users, who can collect single-frequency L-band code and carrier ranging observations (centered at 1575MHz for GPS (L1) and at 1624MHz for Iridium). Users also have access to navigation messages for each constellation and measurement corrections. In the perspective of GPS modernization described in Section 2.1.3, dual-frequency GPS measurements are considered for the sensitivity analysis of longer-term future implementations. In addition, Iridium satellites are equipped with Ka-band (19.5GHz) transmitters [ICA07]. Dual-frequency Iridium signals are therefore simulated as well, although Ka signals might be attenuated by heavy rain.

Finally, user equipment is assumed to include the necessary computational and memory resources to carry out the estimation and detection algorithms (derived in Chapter 5), i.e. to process current and past-time observations collected within a fixed filtering period (noted T_f). As discussed in the following section, the filtering period is limited to ensure the validity of the measurement error models.

4.2 Nominal Measurement Error Models

In this section, the measurement error sources introduced in Section 2.3 are modeled under nominal fault-free conditions. Wide-area differential corrections are insufficient to make residual errors negligible with respect to the carrier phase tracking errors. Therefore, a conservative approach is adopted for the derivation of new parametric error models, which account for the instantaneous uncertainty at signal acquisition (absolute measurement error) as well as variations over the signal tracking duration (relative error with respect to initialization). Unlike existing GPS measurement models used in WAAS (e.g., [Han00a]) and in LAAS [McG00], the iGPS residual error models must deal with large drifts in ranging errors for LEO satellite signals moving across wide sections of the sky. In the following subsections, published data and experimental results help establish an initial knowledge of the measurement error probability distributions (e.g., [War03]) and show that the dynamics of the errors can be reliably modeled over short time periods [Oly02].

4.2.1 Residual Satellite Orbit Ephemeris and Clock Errors. Individual GPS satellite clocks, in spite of their high stability and of corrections provided by the OCS, exhibit a slow but significant drift with respect to true GPS system time. During short filtering intervals, the remaining ranging error can be modeled for a satellite s by:

- an undetermined clock bias sCB at the time the satellite first comes in sight, which is constant over T_F ,
- plus a ramp over time with an unknown but constant gradient sCG , accounting for linear variations from the initial value over T_F .

The satellite clock bias is assumed normally distributed with zero mean and variance σ_{CB}^2 , which with the notation introduced in equation 2.2 is expressed as:

$${}^sCB \sim N(0, \sigma_{CB}^2).$$

The standard deviation σ_{CB-GPS} is approximately 1.5m for GPS [Mis06]. The corresponding value for Iridium is addressed later when combined with the orbit ephemeris bias. Based on several years of GPS data, the initial uncertainty on the parameter sCG is modeled as ${}^sCG \sim N(0, \sigma_{CG}^2)$, where σ_{CG} is $4 \cdot 10^{-4}$ m/s [vGr07] [Par96]. The same gradient model is assumed for Iridium.

Another primary source of error stems from the orbit ephemeris parameters computed by the ground segment. In reference [War03], several years of broadcast GPS ephemeris data were compared to decimeter-level precision post-processed satellite (truth) positions: from 1997 to 2003, daily root-mean-square ranging errors due to orbit parameter errors remain around 1.1m. The GPS ephemeris bias is therefore modeled as ${}^sEB_{GPS} \sim N(0, \sigma_{EB-GPS}^2)$ with σ_{EB-GPS} equal to 1.1m. The value for Iridium is again given below.

In addition, reference [Gra03] investigates the sensitivity over 24 hour periods of computed GPS satellite positions to individual ephemeris parameter errors. It shows that the most sensitive parameter is the orbit inclination angle, which causes satellite position deviations to vary periodically with the orbital period T_{GPS} . This is further corroborated in the 24-hour broadcast ephemeris error plots of Figure 2.3 and references [Par96] [War03].

For short filtering durations T_F (10min or less) relative to T_{GPS} , changes in orbit errors are linear [Oly02]. In this work, a worst slope approximation is used to evaluate the ephemeris gradient sEG , assuming periodic variations with frequency $2\pi/T_{GPS}$ and normally distributed amplitude m_{E-GPS} (with zero mean and variance σ_{EB-GPS}^2):

$${}^sEG_{GPS} = {}^sm_{E-GPS} \frac{2\pi}{T_{GPS}},$$

so that ${}^sEG_{GPS} \sim N(0, \sigma_{EG-GPS}^2)$ with $\sigma_{EG-GPS} = \sigma_{EB-GPS} 2\pi/T_{GPS}$. Since Iridium benefits from higher communication data rates, more numerous and more frequently updated orbital parameters can be exploited. The proposed orbit error model for Iridium is similar to GPS, with $\sigma_{EG-IRI} = \sigma_{EB-IRI} 2\pi/T_{IRI}$, but with a lower standard deviation for the Iridium orbit ephemeris bias σ_{EB-IRI} ($\sigma_{EB-IRI} = 0.1\text{m}$), which is realistically achievable in near-real-time using GPS receivers onboard the LEO spacecraft [Bis01] [Bae06].

The combined ephemeris and clock bias is modeled as ${}^sECB \sim N(0, \sigma_{ECB}^2)$. The value allocated to σ_{ECB} for GPS is $(\sigma_{CB-GPS}^2 + \sigma_{EB-GPS}^2)^{1/2}$, which equals 1.86m. For the same reasons as the ephemeris gradient, a lower value of 0.1m is allocated to σ_{ECB} for Iridium.

When corrections from a WAAS-like network of reference stations are available, the σ_{ECB} value for GPS drops to less than 1m. More precisely, a one-sigma root-mean-square value of 0.86m was computed using quarterly 95% range error indexes for all locations and all GPS satellites tabulated in the WAAS performance analysis reports [NST03] from spring 2002 to spring 2008 (a conservative 2m value is used in simulations).

Finally, the combined ephemeris and clock gradient is defined as:

$${}^s ECG = {}^s CG + {}^s EG ,$$

so that

$${}^s ECG \sim N(0, \sigma_{CG}^2 + \sigma_{EG}^2) .$$

Altogether at epoch k of the filtering interval, for a satellite s that has been visible over a period Δt_k (from filter initiation at t_{k_0} to the sample time of interest t_k), GPS and Iridium SV-related errors are expressed as:

$${}^s \mathcal{E}_{SV,k} = {}^s ECB + \Delta t_k \cdot {}^s ECG .$$

4.2.2 Residual Ionospheric Error. The residual ionospheric error model implemented in this work hinges on three major assumptions. Under anomaly-free conditions, the ionosphere's slow dynamics in the mid-latitude temperate zones justifies that it be assumed constant over the short periods of time in an ECSF frame (whose x-axis is pointing toward the sun and whose z-axis is the earth's axis of rotation) [Oly02] [Coh92] [Chr99]. In Figure 4.5, the varying thickness of the egg-shaped grey area surrounding the earth represents the non-uniform electron density in the ionosphere, which is fixed in ECSF.

Second, the peak electron density occurs between 250km and 400km above the earth surface. A spherical thin shell approximation is typically adopted to localize the effect of the ionosphere. As mentioned earlier, an IPP is defined as the intersection between the satellite-user LOS and the thin shell at an altitude h_i of 350km. IPP displacement in ECSF coordinates is due to the relative motions of the SV, of the user close to earth surface, and of the earth itself. In most precision applications (including aircraft final approach with a relatively low vehicle velocity of 70m/s), GPS IPPs move

mostly westwards in ECSF (especially for high-elevation satellites) because the rotation of the earth is the dominant factor (surface velocity larger than 200m/s at latitudes lower than 65deg). Iridium IPPs in contrast move along a North-South axis due to fast satellite motion. The effect of the earth rotation is highlighted in Figure 4.6: the IPP displacement relative to an arbitrary reference time (e.g., the initial epoch) is plotted over 10min, for a user at a Miami location, in earth-centered-earth-fixed (ECEF) and ECSF reference frames.

Third, extensive LAAS and WAAS-motivated research (see references [Han00a] [Han00b] [Dat02] [Bla03]) suggest that the vertical ionospheric delay varies linearly with IPP separation distances (actually ‘great circle distances’ or GCD) of up to 2000km (it levels off for larger distances). The distribution of the corresponding slope can be bounded by a Gaussian model [Han00a] [Han00b].

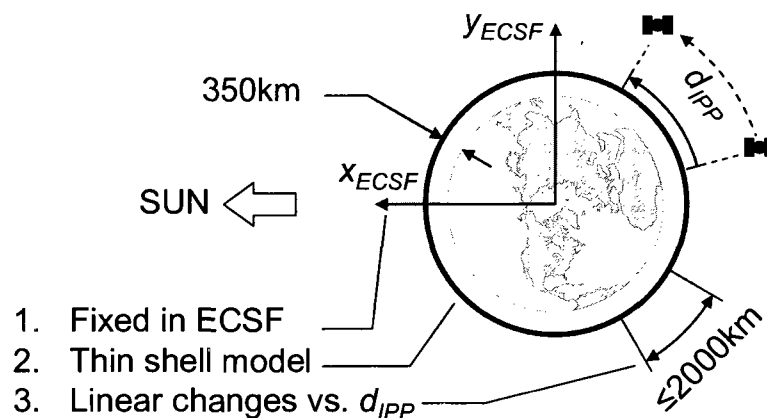


Figure 4.5. Three Assumptions for the Ionospheric Error Model

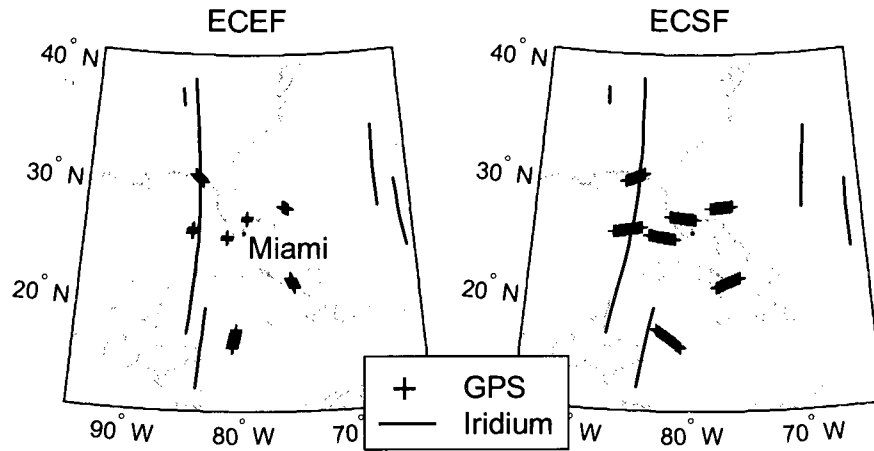


Figure 4.6. IPP Displacement

The equivalent delay or advance is therefore modeled as an initial vertical ionospheric bias VIB associated to a ramp, whose slope over IPP displacement d_{ipp} (in an ECSF frame) is the vertical ionospheric gradient VIG . A single gradient per SV accounts for ramps along one direction only, which means that the model assumes pierce point traces that are straight paths along the great circle, with little lateral motion (as seen in Figure 4.6). An obliquity factor ${}^s ob_{l,k}$ adjusts this error for the fact that the LOS pierces the ionosphere with a slant angle function of the satellite elevation angle ${}^s el_k$ (e.g., [Mis06]):

$${}^s ob_l = 1 / \sqrt{1 - \left[R_E \cos({}^s el) / (R_E + h_l) \right]^2},$$

where R_E is the radius of the earth (6378km). As a result, the slant ionospheric delay is given by:

$${}^s \varepsilon_{l,k} = {}^s ob_{l,k} \cdot ({}^s VIB + d_{ipp,k} \cdot {}^s VIG) \quad (4.1)$$

Initial uncertainties on the bias and gradient are modeled as:

$${}^sVIB \sim N(0, \sigma_{VIB}^2) \quad \text{and} \quad {}^sVIG \sim N(0, \sigma_{VIG}^2).$$

Values are allocated to these parameters as follows.

- Under normal conditions, with standalone single-frequency GPS, a σ_{VIB} of 10-20m is not unreasonable [Mis06]. Empirical ionosphere modeling (e.g., using the Klobuchar model) helps decrease this number by approximately 50% [Klo87].
- Furthermore, an important amount of work (motivated by LAAS and WAAS and referenced earlier) aims at determining the VIG under anomaly-free conditions. Researchers agree on a σ_{VIG} of 1mm/km for quiet days [Kol05] [Lee06b] and 4mm/km for active (but non-stormy) ionospheric days.
- The ionospheric residual error can be significantly decreased when WAAS-like corrections are available. After correction from a WAAS-like network, the instantaneous ionospheric error σ_{VIB} drops to 0.5-1.5m. In fact, a one-sigma root-mean-square value of 0.51m was computed using quarterly 95% ionospheric error indexes for all locations and all GPS satellites tabulated in the WAAS performance analysis reports [NST03] from spring 2002 to spring 2008 (a conservative 1.5m nominal value is used in simulations).
- In addition to VIB, VIG-corrections are computed at the WAAS master stations (they are the slopes of the plane fit computed at each IGP as noted in Section 2.4.2). These corrections are not broadcast because they are not needed in aviation applications currently serviced by WAAS (and due to the low 250bps data transmission rate). A covariance analysis replicated from

[Wal00] establishes that a σ_{VIG} of 0.5mm/km after correction is achievable. Performance analysis in Chapter 6 will evaluate the impact of such corrections as compared to the nominal 4mm/km σ_{VIG} value.

These results were all corroborated after analysis of a limited set of dual-frequency GPS data and WAAS corrections (pictured in Figure 2.4). Further experimental validation using years of data and multiple locations will be performed in future work.

Iridium SVs move across much wider sections of the ionosphere than GPS satellites. The average ratio of Iridium over GPS IPP displacements was computed at mid-latitude locations: it is constant over 10min and is equal to approximately 10. The maximum GCD traveled by an Iridium IPP when occasionally crossing the sky with near-zero azimuth is reached in approximately 10min. Using an expression of the earth central angle (the angle between the satellite, the center of the earth and the user) given in reference [Fos98] and for an elevation mask angle el_{min} of 5deg, the maximum IPP displacement can be expressed as:

$$2(R_E + h_I) \left(\cos^{-1} \left(\frac{R_E \cdot \cos(el_{min})}{R_E + h_I} \right) - el_{min} \right),$$

This number amounts to 3300km, which is larger than the suggested 2000km limit. To circumvent this problem, equation 4.1 is applied piecewise over less-than-2000km-long segments of the satellite pass. In practice, a satellite s whose d_{IPP} exceeds the limit between epochs k and $k+1$ is attributed a new gradient sVIG_N (with ${}^sVIG_N \sim N(0, \sigma_{VIG}^2)$), so that the ionospheric error at epoch $k+j$ posterior to k becomes:

$${}^s\varepsilon_{I,k+j} = {}^s ob_{I,k+j} \cdot \left({}^sVIB + d_{IPP,0:k} \cdot {}^sVIG + d_{IPP,k+1:k+j} \cdot {}^sVIG_N \right),$$

where $d_{IPP,i,j}$ is the IPP displacement between epochs i and j . In fact, simulation results show that this added precaution only generates minor differences in navigation performance results. Another alternative would simply be to limit the filtering period T_F to 5min so that d_{IPP} would never exceed 2000km, but this in turn would limit the positioning accuracy.

4.2.3 Residual Tropospheric Error. The largest part of the delay due to signal refraction in the troposphere can be removed by modeling of its dry and wet gas components [Par96].

The residual uncertainty is modeled as a zenith tropospheric delay ZTD (i.e., associated with a hypothetical signal coming from 90deg elevation), which is constant over the time interval T_F . In addition, user motion causes variations relative to this initial value, which are captured by a LAAS-like residual tropospheric error model expressed as a function of the local air refractivity index Δn [MAS04] [McG00], so that the total zenith tropospheric error is:

$$\varepsilon_{T_Z,k} = ZTD + 10^{-6} h_0 \left(1 - e^{-\Delta h_k / h_0}\right) \cdot \Delta n.$$

Here, Δh_k designates the difference in height that the user (e.g., aircraft) experiences from the start of the filtering interval to epoch k . A fixed value of 15km [MAS04] is assigned to the tropospheric scale height h_0 . Notations are simplified as follows:

$$\varepsilon_{T_Z,k} = ZTD + c_{T,k} \cdot \Delta n,$$

where

$$c_{T,k} = 10^{-6} h_0 \left(1 - e^{-\Delta h_k / h_0}\right).$$

A tropospheric obliquity factor ${}^s ob_{T,k}$ is applied [MAS04] because a larger segment of the signal's path travels through the troposphere at lower elevations:

$${}^s ob_{T,k} = \left(0.002 + \sin^2({}^s el_k)\right)^{-1/2},$$

so that the tropospheric error is expressed as:

$${}^s \mathcal{E}_{T,k} = {}^s ob_{T,k} \left(ZTD + c_{T,k} \cdot \Delta n \right),$$

The parameters ZTD and Δn are not satellite-dependent because they characterize the environment surrounding the airplane. They are modeled as random constants over the time interval T_F such that $ZTD \sim N(0, \sigma_{ZTD}^2)$ [MOP01] and $\Delta n \sim N(0, \sigma_{\Delta n}^2)$ [MAS04], where the nominal standard deviations are given later in Table 4.1.

4.2.4 Receiver Noise and Multipath. The code and carrier phase receiver noise (${}^s v_{RN-\rho,k}$ and ${}^s v_{RN-\phi,k}$) are modeled as Gaussian white noise sequences (according to results of Section 2.3.3):

$$v_{RN-\rho,k} \sim N(0, \sigma_{RN-\rho}^2) \quad \text{and} \quad v_{RN-\phi,k} \sim N(0, \sigma_{RN-\phi}^2).$$

In order to account for the time-correlation introduced by unwanted signal reflections reaching the antenna, the multipath error is modeled as a first-order Gauss-Markov Process (GMP) with time constant T_M , variance $\sigma_{M-\phi/\rho}^2$ and driving noise $v_{M,k}$ (this is the same model as the one introduced in Section 3.2.1):

$${}^s \mathcal{E}_{M,k+1} = e^{-T_k/T_M} \cdot {}^s \mathcal{E}_{M,k} + v_{M,k}$$

with

$$v_{M-\phi/\rho,k} \sim N\left(0, \sigma_{M-\phi/\rho}^2 \left(1 - e^{-2T_p/T_M}\right)\right),$$

where T_p is the sampling interval. Large azimuth-elevation variations generate fast

changes in the directions of signal reflections for Iridium. The multipath time-constant for Iridium $T_{M,IRI}$ was therefore computed by multiplying the time constant for GPS $T_{M,GPS}$ (assumed to be 60s, which is conservative for a dynamic user as explained in Section 2.3.3) with the angular rate ratio between GPS and Iridium satellites (approximately 1/30 according to Section 4.1.1).

4.2.5 Summary of Error Sources. The complete GPS and Iridium carrier phase measurement equation for a satellite s at epoch k can be written as:

$$\begin{aligned} {}^s\phi_k = & {}^s r_k + \tau_k + {}^s N + {}^s ECB + \Delta t_k \cdot {}^s ECG + {}^s ob_{T,k} (ZTD + c_{T,k} \cdot \Delta n) \\ & - {}^s ob_{I,k} ({}^s VIB + {}^s d_{IPP,k} \cdot {}^s VIG) + {}^s \mathcal{E}_{M-\phi,k} + {}^s V_{RN-\phi,k} \end{aligned} \quad (4.2)$$

Unlike in Section 2.4.1, the measurement (${}^s\phi_k$) is not single-differenced between receivers and can not be directly expressed in terms of the user position vector $\mathbf{x}_{ENU,k}$ in a local reference frame. It is customary in GPS navigation to linearize ${}^s\phi_k$ about an approximated user position $\bar{\mathbf{x}}_{ENU,k}$ and clock deviation $\bar{\tau}_k$, which are iteratively refined using a Newton-Raphson approach (described in Appendix C for laser measurements). The linearized carrier phase observation is defined as:

$${}^s\phi_{L,k} = {}^s\phi_k - {}^s\bar{r}_k - {}^s\bar{\mathbf{e}}_k^T \bar{\mathbf{x}}_{ENU,k}$$

where ${}^s\bar{r}_k$ and ${}^s\bar{\mathbf{e}}_k$ are respectively the distance and the LOS vector computed from the approximated user and satellite locations. Finally, using notation akin to equation 2.6, equation 4.2 becomes:

$$\begin{aligned} {}^s\phi_{L,k} = & {}^s \mathbf{g}_k^T \mathbf{u}_k + {}^s N + {}^s ECB + \Delta t_k \cdot {}^s ECG + {}^s ob_{T,k} (ZTD + c_{T,k} \cdot \Delta n) \\ & - {}^s ob_{I,k} ({}^s VIB + {}^s d_{IPP,k} \cdot {}^s VIG) + {}^s \mathcal{E}_{M-\phi,k} + {}^s V_{RN-\phi,k} \end{aligned} \quad (4.3)$$

The equation for the linearized code phase measurement ${}^s\rho_{L,k}$ is identical except for the absence of cycle ambiguity bias sN , a positive sign on the ionospheric error, and the receiver noise ${}^sV_{RN-\rho,k}$ and multipath ${}^s\mathcal{E}_{M-\rho,k}$ which respectively replace ${}^sV_{RN-\phi,k}$ and ${}^s\mathcal{E}_{M-\phi,k}$.

In summary, error parameter values for the nominal configuration (listed in Table 4.1) were selected to describe a system architecture implementable in the short term, for single-frequency GPS/Iridium users. The nominal configuration assumes that users are provided with GPS ephemeris and clock data from the OCS, precise Iridium satellite orbit and clock information, as well as WAAS-like GPS satellite clock and orbit ephemeris corrections and ionospheric corrections for VIB. An estimated 10min upper-limit is fixed on the validity of the error models.

The initial uncertainty on the error parameters (Table 4.1) constitute the *prior knowledge* acquired from experimental observations of physical phenomena, and are a crucial input to the estimation algorithm (derived in Chapter 5).

Finally, the assertion that error models are conservative is only true if the Gaussian models over-bound the cumulative distribution functions of each error sources' ranging errors [DeC00]. The next phase of this research consists in establishing probability distributions for the error parameters, and in verifying the fidelity of the dynamic models to experimental data. Alternatively, parameter values in Table 4.1 may be considered as requirements that ground corrections should meet in order to achieve the desired system performance (evaluated in Chapter 6).

Table 4.1. Summary of Error Parameter Values

Parameter	Description (σ : standard deviations, a.f.i.: at filter initialization)	Nominal Value
$\sigma_{ECB-GPS}$	GPS SV clock & ephem. bias a.f.i. (corrected)	2m
$\sigma_{ECG-GPS}$	GPS SV clock & ephem. gradient a.f.i. (uncorrected)	$4.72 \cdot 10^{-4}$ m/s
$\sigma_{ECB-IRI}$	Iridium SV clock & ephemeris bias a.f.i.	0.1m
$\sigma_{ECG-IRI}$	Iridium SV clock & ephemeris gradient a.f.i.	$4.57 \cdot 10^{-4}$ m/s
σ_{ZTD}	Residual zenith tropospheric delay a.f.i.	0.12m
$\sigma_{\Delta n}$	Residual refractivity index a.f.i. (unit-less)	$30 \cdot 10^{-6}$
σ_{VIB}^*	Vertical ionospheric bias a.f.i. (corrected)	1.5m
σ_{VIG}^*	Vertical ionospheric gradient a.f.i. (uncorrected)	4mm/km
$\sigma_{RN-\rho}^{**}$	Code phase receiver noise	0.3m
$\sigma_{RN-\phi}^{**}$	Carrier phase receiver noise	0.003m
$\sigma_{M-\rho}^{**}$	Code phase multipath noise	1m
$\sigma_{M-\phi}^{**}$	Carrier phase multipath noise	0.01m
$T_{M,GPS}$	GPS multipath time constant	1min
$T_{M,IRI}$	Iridium multipath time constant	2s

* for dual-frequency at f_1 and f_2 (GPS: L_1/L_5 , Iridium: L/Ka): VIG and VIB terms are eliminated

** for dual-frequency (f_1, f_2), these terms are multiplied by $([f_1^2/(f_1^2 - f_2^2)]^2 + [f_2^2/(f_1^2 - f_2^2)]^2)^{1/2}$

4.3 Measurement Fault Models

Measurement errors, whose magnitude, distribution and dynamics are not accounted for in the above nominal models, are referred to as faults. They correspond to rare events such as equipment and satellite failures or unusual atmospheric conditions (as described in Section 4.3.1 and listed in Table 4.2). Fault models are developed in Section 4.3.2 to reproduce the impact of such rare-event integrity threats. They will later be deliberately injected into simulated measurements to evaluate the performance of the fault-detection algorithm.

Table 4.2. Fault Mode Inventory (Page 1 of 3)

Error Source	Origin	Primary Effect	Impact on Ranging Measurement	Mitigation	Current Threat Model
Signal Deformation	Ranging Source (Satellite)	Measurement correlation peak offset	Single SV measurement offset or drift on code	Ground and user RAIM monitor	Single channel step, ramp
Satellite Signal Power	Ranging Source (Satellite)	Reduced signal power, C/N degraded	Increase in single SV meas. noise on code/carrier	Ground and user C/N and doppler monitor	Not yet implemented
Code-Carrier Divergence	Ranging Source (Satellite)	Code delayed, carrier advanced	Single SV meas. drift on code minus carrier	Ground and user RAIM monitor	Single channel step, ramp
Excessive Clock Drift	Ranging Source (Satellite)	Acceleration, steps in pseudorange meas.	Single SV meas. acceleration on code and carrier	Ground and user RAIM monitor	Single channel step, ramp
Ephemeris Fault	Ranging Source (Satellite)	Incorrect calculation of SV ranges	Single SV meas. offset, drift, acceleration on code & carrier	Ground and user RAIM monitor	Single channel step, ramp
Tropospheric Anomaly	Propagation Environment (R)	Signal delay due to refraction	Offset, drift, acceleration in all measurements	Ground monitor	Not yet implemented
Interference	Propagation Environment (R)	Increased noise	Increased noise on all measurements	Ground C/N monitor	Not yet implemented

Table 4.2. Fault Mode Inventory (Page 2 of 3)

Error Source	Origin	Primary Effect	Impact on Ranging Measurement	Mitigation	Current Threat Model
Ionospheric Anomaly on GPS Meas.	Propagation Environment (U)	Code delayed, carrier advanced	One or two SVs, code and carrier meas. offset/drift	User RAIM (and ground) monitor	Single channel step, ramp
Ionospheric Anomaly on Iridium Meas.	Propagation Environment (U)	Code delayed, carrier advanced	Single SV code and carrier meas. impulse, step, short ramp	User RAIM (and ground) monitor	Single channel step, ramp, impulse
Tropospheric Anomaly	Propagation Environment (U)	Signal delay due to refraction	Offset, drift, acceleration in all measurements	User RAIM monitor	Single channel step, ramp
Interference	Propagation Environment (U)	Increased noise	Increased noise on all measurements	User C/N monitor	Not yet implemented
Receiver/Antenna Hardware	Ground Equipment	Reduced signal power or increased noise level	Increased noise on all measurements for that one receiver	Ground monitor (multiple receivers)	None needed
Receiver Hardware	Ground Equipment	Single channel bias	Single SV meas. offset, on code and carrier	Ground monitor (multi. receivers)	None needed
Excessive Multipath	Ground Equipment	Delayed Signal combines with direct signal	All measurements for that one antenna, or for multiple antennas (diffuse multipath)	Ground monitor (multiple receivers)	Not yet implemented

Table 4.2. Fault Mode Inventory (Page 3 of 3)

Error Source	Origin	Primary Effect	Impact on Ranging Measurement	Mitigation	Current Threat Model
Processing Fault	Ground Equipment	Many possible effects		Ground monitor (multi. processors)	None needed
Communication Fault	Ground Equipment	Message corrupted		CRC performed by user detects and excludes	None needed
Receiver/Antenna Hardware	User Equipment	Reduced signal power or increased noise level	Increased noise on all measurements for that one receiver	User redundant avionics/voting	None needed
Receiver Hardware	User Equipment	Single channel bias	Single SV meas. offset, on code and carrier	User redundant avionics/voting	None needed
Excessive Multipath	User Equipment	Delayed Signal combines with direct signal	Measurements for one antenna, or multiple antennas (diffuse multipath)	User RAIM monitor	Single channel step. ramp
Processing Fault	User Equipment	Many possible effects		User redundant avionics/voting	None needed
Communication Fault	User Equipment	Message corrupted	All measurements for that one antenna, or for multiple antennas (diffuse multipath)	CRC performed by user detects and excludes	None needed

4.3.2 Inventory of Faults. Potential faults to be considered in aircraft navigation applications are summarized in Table 4.2 (inspired from reference [MAS04]). Faults are grouped with respect to their origin (second column): they may be caused by the satellite, by the signal's transit environment to the reference stations (R) or user (U) location, or by the ground or user equipment. Ground stations equipped with dual-frequency receivers are unaffected by ionospheric anomalies.

The third and fourth columns of Table 4.2 describe the primary effects of the faults and their impact on the ranging measurements. Measurement fault models are designed to recreate such failure modes. In this work, particular attention is paid to the behavior of faults over time because constant carrier phase cycle ambiguities are estimated using sequences of observations.

4.3.3 Single-Satellite Fault Models. A set of canonical threat models is established. Simulated faults of arbitrary magnitude (the worst case magnitude is determined as part of the RAIM detection method derived Section 5.2), spanning the entire range of possible starting times (at regular intervals T_B of 5s or less over the filtering period T_F), are constructed using blocks of truncated triangular and diagonal matrices. For example, if four consecutive measurements at a sampling interval T_p of 10s (in this example, $T_p = 2T_B$) are stacked over time for a satellite s , the set of failures is:

$${}^s\mathbf{f} = \begin{bmatrix} 0 & 0 & 0 & 1 & 0 & 0 & 1 & 0 & 0 & 0.5 & 0 & 0 \\ 0 & 0 & 1 & 1 & 0 & 1 & 2 & 0 & 0.5 & 1.5 & 0 & 1 \\ 0 & 1 & 1 & 1 & 1 & 2 & 3 & 0.5 & 1.5 & 2.5 & 1 & 0 \\ 1 & 1 & 1 & 1 & 2 & 3 & 4 & 1.5 & 2.5 & 3.5 & 0 & 0 \end{bmatrix}.$$

Let t_{k_0} be the time of the first measurement. The first four columns represent step faults.

The next six columns are ascending ramps (whose starting times respectively from left to right are $t_{k_0} + 4T_B$, $t_{k_0} + 2T_B$, t_{k_0} , $t_{k_0} + 5T_B$, $t_{k_0} + 3T_B$ and $t_{k_0} + T_B$) and the last two columns are impulse-type faults. For efficiency, all redundant failure modes are eliminated (for example, ramps starting between the last two samples are equivalent to the first column). Similar matrices are generated for all measurements collected during the filtering duration T_F , and are applied to code and carrier phase measurements individually as well as simultaneously, one SV at a time. In practice, when establishing failure modes for all satellites, columns of the full fault matrix are filled with zeros to fit the dimension of the measurement vector. Therefore, each column of the fault matrix is a single-satellite fault mode of arbitrary magnitude. As a result, the number of simulated threat models exceeds 7000 for a ten-minute filtering interval. These fault models will be deliberately injected in GPS and Iridium measurements to evaluate the detection performance of the RAIM algorithm derived in Chapter 5.

At this stage of this research, simulated faults are limited to satellite failures because they are the only types of faults for which the failure rate FR is reliably known. Reference [SPS01] specifies that the satellite service failure frequency should not exceed three per year for the entire GPS constellation. This number is said to be conservatively established based upon a historical assessment of spacecraft and OCS characteristics (reference [FAA02] provides a more conservative estimate but makes no claim of experimental validation). In fact, the GPS ground segment monitors the satellite's health to minimize the probability of faults.

As indicated in column 6 of Table 4.2, steps and ramps account for a large part of the satellite faults, including signal deformation, code-carrier divergence, excessive clock

deviations and erroneous ephemeris parameters. Satellite fault modes stopping during the interval T_F (e.g., descending ramps) are not considered: such faults would have either repaired themselves, which is unlikely, or would have gotten repaired after being detected by the ground, in which case the spacecraft would have been set unhealthy by the OCS.

Furthermore, the canonical fault modes of matrix \mathbf{f} are valid for more than satellite faults and will be used again in future investigations. For example, ionospheric fronts translate into ramps for GPS measurements (as modeled in [Lee06a]), and into steps or impulses for fast moving Iridium satellites, whose LOS might cross the front in a few seconds. Also carrier phase cycle slips at the user receiver can be modeled by steps. Failure types such as discontinuous ramps (e.g., ionospheric fronts), accelerations (e.g., SV clock) or tropospheric fronts (e.g., modeled as triangular functions in [Cha08]) also have to be addressed in future work.

A new approach, different from the canonical fault modes, is developed in Section 5.3.1. It consists in testing the system for the single-satellite faults that are the most difficult to detect using the measurement residuals. The concept is introduced later because it requires prior mathematical development of the RAIM algorithm.

4.4 Integrity Risk Allocation

For iGPS to be validated as a navigation solution for applications such as autonomous transportation, it must demonstrate the ability to fulfill an overall integrity requirement. For example, for the benchmark mission of aircraft precision approach, requirements specify that no more than one undetected hazardous navigation system failure is allowed in a billion approaches [MAS04].

In this work, the overall integrity risk requirement, or probability of hazardous misleading information (HMI), is noted P_{HMI} . It is defined as the limit probability of any information sent by iGPS resulting in out-of-specification user position error without timely warning [MAS04]. It represents the total integrity budget that must be allocated to individual system components in order to ensure safe user navigation under FF, SSF, and all other conditions.

4.4.1 Ground and User Integrity Monitoring. Measurement error sources are represented on a simplified schematic in Figure 4.7. Potential sources of faults can be monitored by the ground and user segments, as indicated respectively by fair and dark shaded areas. Satellite ranging sources are surrounded by even darker areas to signify that they can be monitored by both the user (U) and the ground reference (R) stations. The user signal propagation environment can be at least partially observed by the ground network using models of the atmospheric error spatial correlation.

The ground segment is better equipped than the user to detect certain types of faults (including reference receiver, reference propagation environment and satellite faults), as suggested in column 5 of Table 4.2. If the iGPS ground infrastructure is implemented like WAAS, each ground station will be equipped with redundant dual-frequency (DF) receivers, and will have access to additional external information if necessary (stored ephemerides, meteorological data, precise clock, etc.). Also in WAAS, all measurements are gathered at redundant master stations for estimation and detection of reference receiver and ranging source failures.

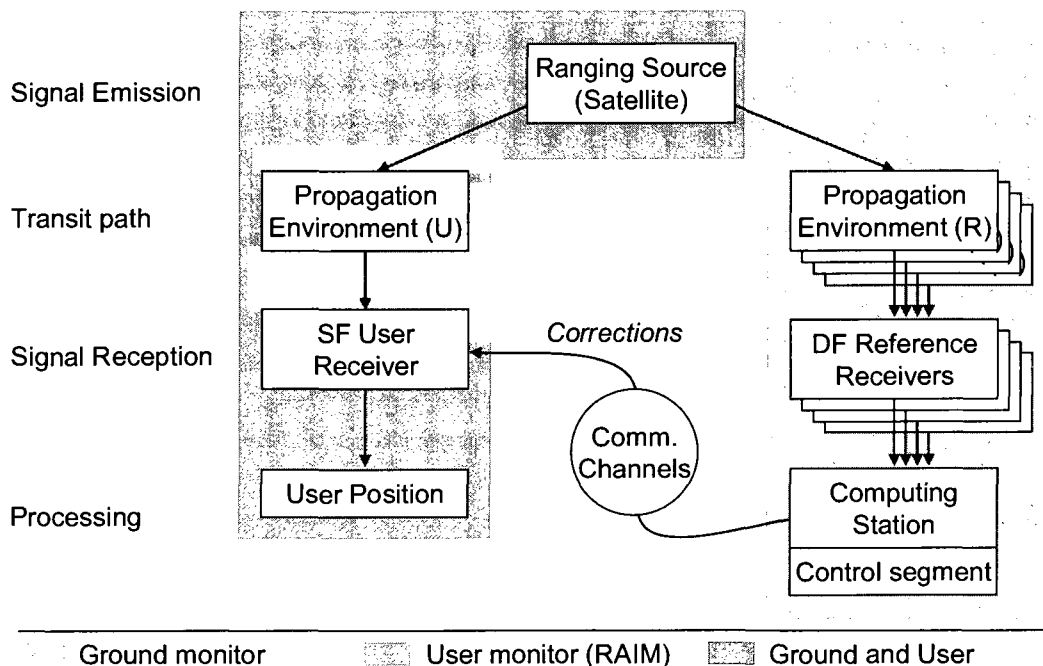


Figure 4.7. Simplified Schematic of User and Ground Measurement Error Sources

User equipment faults, localized anomalies in the user propagation environment and satellite faults can be monitored at the user receiver using RAIM. User equipment faults can also be monitored using redundant avionics.

Hence, fault detection must be performed both at ground stations and at the user. Two architectures are considered:

- *Ground-assisted RAIM fault-detection:* The ground segment monitors against satellite faults and ionospheric disturbances that may affect the user. Updated information (e.g., 'do not use' flags or short-term error bounds) are transmitted and must reach the user within a specified time-to-alert (TTA). The integrity of measurements that are not protected by the ground (more recent than current time minus TTA), must be ensured by the user.

- *Standalone RAIM fault-detection*: The detection of faults in satellites and in the user equipment and propagation environment is entirely performed using RAIM. The role of the ground system is limited to ensure the integrity of broadcast long-term corrections. In this case, the time between RAIM-based detection and alert is reduced to negligible computation delays that are well within the TTA requirement.

The second architecture may not be as efficient (it does not exploit the detection capability available at ground installations) but it is less constraining (the TTA requirement is met). It is therefore the architecture of choice for the upcoming analyses.

4.4.2 Standalone RAIM. A preliminary integrity allocation tree for the standalone RAIM architecture is established in Figure 4.8. It is a practical tool to analyze the total integrity performance in function of individual system components. The top layer of the tree is the overall integrity risk requirement P_{HMI} . It is subdivided between the fault-free case, the single-fault case, and all other cases.

An integrity risk P_ϵ is allocated to this third category (other cases). They include cases of multiple SV faults occurring during the same time interval T_F . Multiple simultaneous faults are considered independent events and hence have a low probability of occurrence. The prior probability p_p for an individual satellite fault, with failure rate FR (introduced in Section 4.3.2), occurring during the exposure period T_F , is defined as: $p_p = FR \cdot T_F$. Therefore, the value allocated to P_ϵ can be selected larger than the probability of two or more faults occurring during T_F , so that:

$$P_\epsilon \geq 1 - \sum_{k=0}^1 C_k^{n_s} p_p^k (1 - p_p)^{n_s - k},$$

where $C_k^{n_s}$ is the binomial coefficient, the number of combinations of k satellites given the total number of visible satellites n_s . For a 10min exposure period T_F and using measurements from 7 different SVs, the probability P_ϵ is larger than 10^{-10} .

An integrity budget of $\alpha(P_{HMI} - P_\epsilon)$ is allocated to normal fault-free conditions (FF), and the remaining fraction $(1 - \alpha)(P_{HMI} - P_\epsilon)$ is attributed to single-satellite failures (SSF). The coefficient α ranges between 0 and 1 and is selected in Section 6.1.2 to maximize the combined FF and SSF performance.

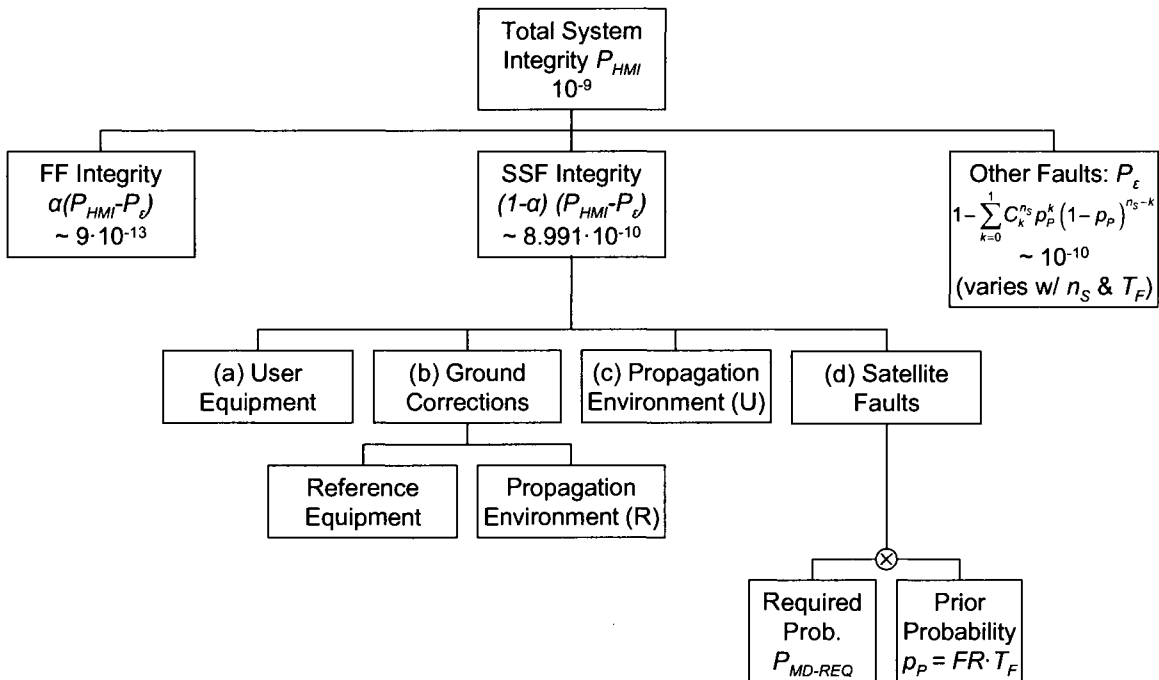


Figure 4.8. Preliminary Integrity Allocation Tree for Standalone RAIM

The third layer of the tree breaks down the single channel faults into (a) user equipment malfunctions, (b) faults in the corrections sent by the ground, (c) anomalous conditions in the user's propagation environment, and (d) satellite failures. Faulty ground corrections (item (b)) may be caused by faults in the reference equipment and propagation environment for the reference location. The third and fourth layers of the tree may be further subdivided into error sources according to Table 4.2.

The following items are left aside for now, and will be treated in future phases of this research:

- (a) faults in user equipment (integrity may be guaranteed by avionics redundancy),
- (b) faults in ground corrections (small probability of occurrence because ground monitoring functions will exist),
- (c) faults in the user's propagation environment (establishing the probability of occurrence of ionospheric and tropospheric anomalies is outside the scope of this work)
- multiple simultaneous faults caused by error sources (a), (b) and (c).

Therefore, as mentioned earlier, results established in upcoming analyses account for spacecraft failures only. The integrity risk caused by a single-satellite fault is the product of its required probability of missed detection P_{MD-REQ} with its prior probability of occurrence p_p .

In summary, the integrity risk allocation tree provides performance requirements for the fault-free estimation algorithm (with a FF integrity risk of $\alpha(P_{HMI} - P_\epsilon)$) and for the RAIM fault detection method (with a required probability of missed detection

P_{MD-REQ}). Estimation and detection algorithms are devised and evaluated in Chapters 5 and 6 in order to assess the ability of iGPS to fulfill the overall integrity requirement

P_{HMI} .

CHAPTER 5

IGPS POSITIONING AND FAULT-DETECTION ALGORITHM

Observations from fast-moving LEO Iridium satellites have the potential to accelerate the estimation of cycle ambiguity biases, hence enabling rapid carrier phase positioning. Still, the accuracy of the cycle ambiguity estimates improves as the signal tracking duration increases. In parallel, realistic measurement error models could be established in Chapter 4 in large part because short time periods were considered (deriving and validating error models over longer durations is much more challenging).

Thus, a crucial tradeoff is shaping the carrier phase iGPS estimation process: as the filtering duration increases to draw maximum benefit from changes in satellite geometry, the robustness of the measurement error model decreases. In response, an upper limit on filter duration is set to ensure the error model validity, and a fixed-interval smoothing algorithm is devised in Section 5.1 for the simultaneous estimation of user position and floating carrier phase cycle ambiguities. It is compatible with real-time implementations provided that sufficient memory is allocated to the storage of a finite number of past measurements and LOS coefficients.

In addition, Iridium and GPS observations collected within the filtering interval are all vulnerable to rare-event integrity threats such as user equipment and satellite failures. To protect the system against faults that may affect successive measurements, a residual-based RAIM detection method is developed in Section 5.2.

The iGPS RAIM algorithm is further investigated in Section 5.3. First, an expression for the most-difficult-to-detect fault is derived. Then, in cases where the fault detection requirement (noted P_{MD-REQ} in Section 4.4.2) is not met using standalone RAIM

and where the mission duration exceeds the initial filtering period, a second layer of integrity monitoring may be implemented using relative RAIM (RRAIM).

5.1 iGPS Position and Cycle Ambiguity Estimation Algorithm

Models previously derived for the satellite clock and ephemeris, the ionosphere and the troposphere errors all assume that measurements are collected over a short, limited duration. In order not to exceed the 10min period of model validity, optimal position and cycle ambiguity estimation is performed using a fixed-interval filtering algorithm.

Continuous real-time operation requires that measurements and LOS coefficients be stored over the filtering interval T_F . Let t_{j-1} and t_j be two successive epochs, and let T_j be the positioning update interval defined as: $T_j = t_j - t_{j-1}$ (T_j is only limited by the receiver sampling period, and may be lower than 1s). At each new epoch t_j , incoming data is updated and the oldest stored data at $t_{j-1} - T_F$ can be erased from memory. Current-time optimal state estimates are obtained from iteratively feeding the stored finite sequence of observations (between $t_j - T_F$ and t_j) into a Kalman filter (KF).

In this regard, the interval T_p between samples sent to the KF does not have to be equal to T_j . Within the interval T_F , there is limited benefit in using all available measurements both because of their correlation in time due to multipath (for GPS signals), and because the contribution of geometry change to the estimation process far outweighs that of redundant measurement averaging. Therefore past measurements within T_F are selected at regular intervals T_p of 30s, which greatly decreases the computational burden

while maintaining similar positioning performance. All the time variables are summarized in Figure 5.1.

The KF also provides an indication of the estimation uncertainty in the form of a state covariance matrix, which serves as basis for the analyses of Chapter 6. State augmentation is used to integrate the dynamics of all error models (i.e., extra states for constant biases and gradients), including the multipath GMP [Gel74]. Practical implementation of the KF also necessitates that rows and columns for all vectors and matrices (including covariance matrices) be added and removed as satellites come in and out of sight (which is frequent for Iridium).

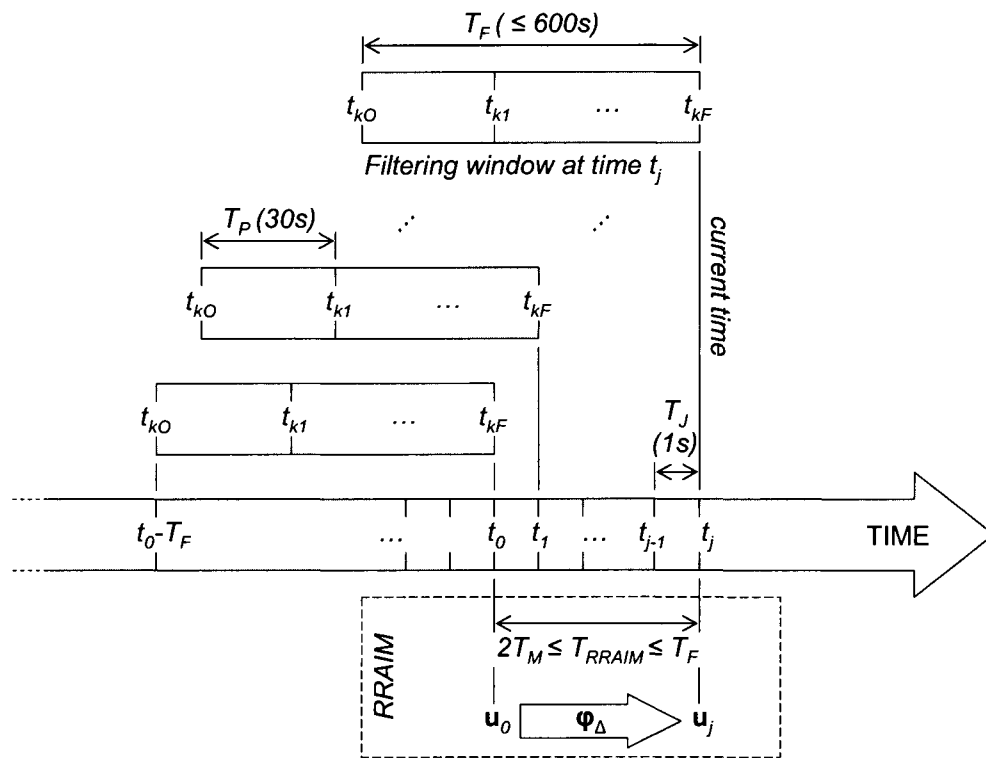


Figure 5.1. Time Variables used in the Algorithms

Measurement faults, whether they affect recent or older observations within the interval T_F , are just as likely to generate hazardous current-time positioning information. In anticipation of the RAIM-type residual-based fault detection introduced in Section 5.2, a fixed-interval smoothing (instead of filtering) process is used; it can be efficiently realized using for example a forward-backward iterative smoother, or a Rauch-Tung-Striebel algorithm [Cra04]. Although smoothing is computationally more intensive than filtering, the computation time is negligible with respect to the specified 1s time-to-alarm (TTA) limit [MAS04].

Finally, in applications where timing and computational load are not of primary concern, measurements can be processed as a batch, which is the method presented below for clarity in exposition. Batch processing produces results identical to the KF for the current time, as well as optimal estimates for past epochs that are later used for residual generation.

Consider first the vector of carrier phase observations for a satellite s in view between epochs k_O and k_F :

$${}^s\boldsymbol{\varphi} = \left[{}^s\phi_{k_O} \quad \cdots \quad {}^s\phi_{k_F} \right]^T.$$

These epochs are the first and last of the smoothing interval for GPS signals, but not necessarily for Iridium satellites, whose passes are often shorter than T_F . For clarity of notation, no subscript is added to capture the fact that ${}^s\boldsymbol{\varphi}$ can be established at any time t_j of interest (e.g., in real time applications, at the current epoch).

A state space representation of vector ${}^s\boldsymbol{\varphi}$ is realized based on equation 4.3. In the same way as in the aforementioned KF, error parameters and their dynamic models are

incorporated by state augmentation. Let $\mathbf{0}_{n \times m}$ be a $n \times m$ matrix of zeros. State coefficients are arranged in matrices that are needed in later steps, so that for satellite s :

$${}^s \mathbf{G} = \begin{bmatrix} {}^s \mathbf{g}_{k_O}^T & \mathbf{0}_{1 \times 4} \\ & \ddots \\ \mathbf{0}_{1 \times 4} & {}^s \mathbf{g}_{k_F}^T \end{bmatrix}, \quad {}^s \Delta \mathbf{t} = \begin{bmatrix} 0 & \Delta t_{k_1} & \cdots & \Delta t_{k_F} \end{bmatrix}^T,$$

$${}^s \mathbf{ob}_T = \begin{bmatrix} {}^s ob_{T,k_O} & \cdots & {}^s ob_{T,k_F} \end{bmatrix}^T,$$

$${}^s \mathbf{c}_T = \begin{bmatrix} 0 & {}^s ob_{T,k_1} \cdot c_{T,k_1} & \cdots & {}^s ob_{T,k_F} \cdot c_{T,k_F} \end{bmatrix}^T,$$

$${}^s \mathbf{ob}_I = \begin{bmatrix} {}^s ob_{I,k_O} & \cdots & {}^s ob_{I,k_F} \end{bmatrix}^T \text{ and}$$

$${}^s \mathbf{c}_I = \begin{bmatrix} 0 & {}^s ob_{I,k_1} \cdot d_{IPP,k_1} & \cdots & {}^s ob_{I,k_F} \cdot d_{IPP,k_F} \end{bmatrix}^T.$$

Carrier phase observations for all n_s Iridium and GPS satellites are then stacked together:

$$\boldsymbol{\varphi} = \begin{bmatrix} {}^1 \boldsymbol{\varphi}^T & \cdots & {}^{n_s} \boldsymbol{\varphi}^T \end{bmatrix}^T.$$

The carrier phase measurement equation is written in the form:

$$\boldsymbol{\varphi} = \mathbf{H}_\varphi \mathbf{x} + \mathbf{v}_\varphi, \quad (5.1)$$

where \mathbf{v}_φ designates the carrier phase measurement noise vector and the observation matrix \mathbf{H}_φ will be defined below. The state vector is

$$\mathbf{x} = \begin{bmatrix} \mathbf{u}_{k_O}^T & \cdots & \mathbf{u}_{k_F}^T & \mathbf{N}^T & \mathbf{ECB}^T & \mathbf{ECG}^T & ZTD & \Delta n & \mathbf{VIB}^T & \mathbf{VIG}^T \end{bmatrix}^T,$$

where k_O and k_F (subscripts of \mathbf{u}) are now the first and last epochs of the smoothing interval. Bold face characters for parameters other than \mathbf{u}_k designate vectors of states for all satellites, such as for example:

$$\mathbf{N} = \begin{bmatrix} {}^1N & \cdots & {}^{n_s}N \end{bmatrix}^T.$$

The dynamics of the user position and clock deviation vector \mathbf{u}_k are unknown. Different states are therefore allocated to the vector \mathbf{u}_k at each time step, as opposed to the other parameters that are modeled as constants over interval T_F .

The carrier phase observation matrix \mathbf{H}_φ is constructed by blocks:

$$\mathbf{H}_\varphi = [\mathbf{G} \quad \mathbf{B}_N \quad \mathbf{B}_{\text{ECB}} \quad \mathbf{B}_{\text{ECC}} \quad \mathbf{B}_{\text{ZTD}} \quad \mathbf{B}_{\Delta n} \quad \mathbf{B}_{\text{VIB}} \quad \mathbf{B}_{\text{VIG}}].$$

Each block corresponds to a vector of state parameters, and contains coefficients for all spacecraft, for the entire sequence of measurements. Let $n_k(s)$ be the number of samples for satellite s (which generally differs for Iridium SVs), and $\mathbf{1}_{n \times 1}$ be a $n \times 1$ column-vector of ones:

$$\begin{aligned} \mathbf{G} &= \begin{bmatrix} {}^1\mathbf{G} \\ \vdots \\ {}^{n_s}\mathbf{G} \end{bmatrix}, & \mathbf{B}_N = \mathbf{B}_{\text{ECB}} &= \begin{bmatrix} \mathbf{1}_{n_k(1) \times 1} & & 0 \\ & \ddots & \\ 0 & & \mathbf{1}_{n_k(n_s) \times 1} \end{bmatrix}, \\ \mathbf{B}_{\text{ECC}} &= \begin{bmatrix} {}^1\Delta t & & 0 \\ & \ddots & \\ 0 & & {}^{n_s}\Delta t \end{bmatrix}, & \mathbf{B}_{\text{ZTD}} &= \begin{bmatrix} {}^1\mathbf{ob}_T \\ \vdots \\ {}^{n_s}\mathbf{ob}_T \end{bmatrix}, & \mathbf{B}_{\Delta n} &= \begin{bmatrix} {}^1\mathbf{c}_T \\ \vdots \\ {}^{n_s}\mathbf{c}_T \end{bmatrix} \\ \mathbf{B}_{\text{VIB}} &= - \begin{bmatrix} {}^1\mathbf{ob}_I & & 0 \\ & \ddots & \\ 0 & & {}^{n_s}\mathbf{ob}_I \end{bmatrix}, & \text{and } \mathbf{B}_{\text{VIG}} &= - \begin{bmatrix} {}^1\mathbf{c}_I & & 0 \\ & \ddots & \\ 0 & & {}^{n_s}\mathbf{c}_I \end{bmatrix}. \end{aligned}$$

A measurement equation similar to equation 5.1 is established for the code-phase observation vector $\boldsymbol{\rho}$. In this case, the sign on the ionospheric coefficients \mathbf{B}_{VIB} and \mathbf{B}_{VIG} is positive. Also, the columns of ones in \mathbf{B}_N corresponding to the cycle ambiguity vector \mathbf{N} are replaced by zeros; this explains why state vectors \mathbf{N} and \mathbf{ECB} have to be

distinguished, even though columns of \mathbf{B}_N and \mathbf{B}_{ECB} are linearly dependent for carrier phase measurements. Since no prior knowledge is assumed for \mathbf{N} , the system's performance sensitivity to \mathbf{ECB} (later investigated in Section 6) reflects the influence of code-phase measurements. It is also worth noticing that no more than $n_s - 1$ cycle ambiguities are actually observable because the unknown receiver clock bias in \mathbf{u}_k is common to all satellites [Hwa91]. This is not an issue here because the integer nature of cycle ambiguities is not exploited (a reduced order form may be implemented [Per97]).

The complete sequence of code and carrier phase signals for all satellites over the smoothing interval are included into a batch measurement vector:

$$\mathbf{z}_B = [\boldsymbol{\varphi}^T \quad \boldsymbol{\rho}^T]^T,$$

and

$$\mathbf{z}_B = \mathbf{H}_B \mathbf{x} + \mathbf{v}_B. \quad (5.2)$$

The measurement noise vector \mathbf{v}_B is utilized to introduce the time-correlated noise due to multipath modeled as a GMP. Its covariance \mathbf{V}_B is block diagonal, and each block corresponds to observations from a same SV over time. Within each block, the time-correlation between two measurements originating from a same satellite s at sample times t_i and t_j is modeled as $\sigma_{M-\rho/\phi}^2 \cdot e^{-\Delta t_{ij}/T_M}$, where $\Delta t_{ij} = |t_i - t_j|$. $\sigma_{RN-\rho}^2$ and $\sigma_{RN-\phi}^2$ are also added to the diagonal elements to account respectively for code-phase and for carrier phase uncorrelated receiver noise.

Finally as mentioned in Section 4.2, valuable information is gained from the study of the physical phenomena causing measurement disturbances. This prior knowledge of the error parameters is expressed in terms of bounding values on their probability distributions. It can be included as a vector of pseudo-measurements \mathbf{z}_p that provide

direct a-priori observations to the corresponding states. Let n_S , n_E and n_K be respectively the numbers of available satellites, of error states and of samples over T_F . In addition, let \mathbf{I}_n be a $n \times n$ identity matrix. \mathbf{H}_p is defined as $[\mathbf{0}_{n_E \times (4n_K + n_S)} \quad \mathbf{I}_{n_E}]$, so that:

$$\mathbf{z}_p = \mathbf{H}_p \mathbf{x} + \mathbf{v}_p. \quad (5.3)$$

The covariance matrix \mathbf{V}_p of the pseudo-measurement noise vector \mathbf{v}_p is diagonal, with values of the initial conditions on the error states **ECB**, **ECG**, **ZTD**, Δn , **VIB** and **VIG**. In other words, the diagonal vector of \mathbf{V}_p is:

$$\left[\mathbf{1}_{1 \times n_S} \sigma_{ECB}^2 \quad \mathbf{1}_{1 \times n_S} \sigma_{ECG}^2 \quad \sigma_{ZTD}^2 \quad \sigma_{\Delta n}^2 \quad \mathbf{1}_{1 \times n_S} \sigma_{VIB}^2 \quad \mathbf{1}_{1 \times n_S} \sigma_{VIG}^2 \right].$$

The elements of \mathbf{z}_p are the mean values of the error states (zeros in this case). The vector \mathbf{z}_p can either be added to the system by direct augmentation of \mathbf{z}_B , in which case $\mathbf{z} = [\mathbf{z}_B^T \quad \mathbf{z}_p^T]^T$, $\mathbf{H} = [\mathbf{H}_B^T \quad \mathbf{H}_p^T]^T$, and the covariance matrix \mathbf{V} of the measurement noise \mathbf{v} is block diagonal with \mathbf{V}_B and \mathbf{V}_p on its diagonal. It can also be incorporated using the equivalent reduced-order form proposed in Appendix E. An alternative derivation based on the method of Lagrange multipliers and without introducing the concept of pseudo-measurements is available in reference [Cra04]. The total measurement equation becomes:

$$\mathbf{z} = \mathbf{H}\mathbf{x} + \mathbf{v}. \quad (5.4)$$

The weighted least squares estimate $\hat{\mathbf{x}}$ of the state vector \mathbf{x} is obtained using the equation:

$$\hat{\mathbf{x}} = \mathbf{S} \mathbf{z}, \quad (5.5)$$

where \mathbf{S} is the weighted pseudo-inverse of \mathbf{H} :

$$\mathbf{S} = (\mathbf{H}^T \mathbf{V}^{-1} \mathbf{H})^{-1} \mathbf{H}^T \mathbf{V}^{-1}, \quad (5.6)$$

and the state covariance matrix is:

$$\mathbf{P}_x = (\mathbf{H}^T \mathbf{V}^{-1} \mathbf{H})^{-1}. \quad (5.7)$$

The diagonal element of \mathbf{P}_x corresponding to the current-time vertical position covariance (noted σ_u^2) is used in Chapter 6 to determine the positioning performance under fault-free conditions. The focus is on the Up-coordinate, both because of the tighter requirements in this direction and because of the generally higher vertical dilution of precision (or VDOP, defined as the third diagonal element of $(\mathbf{G}_k^T \mathbf{G}_k)^{-1}$ where $\mathbf{G}_k = [{}^1 \mathbf{g}_k^T \quad \cdots \quad {}^{n_s} \mathbf{g}_k^T]^T$) as compared to horizontal coordinates.

5.2 iGPS RAIM-type Detection Algorithm

State estimation is based on a history of observations, all of which are vulnerable to equipment faults (satellite clock excessive acceleration, corrupted ephemeris parameter, user receiver cycle slip, etc. [MAS04]) or unusual atmospheric phenomena. To protect the system against abnormal events, a RAIM-type process is implemented, using the least-squares residuals of the batch measurement equation 5.4.

The least-squares residual RAIM methodology gives a statistical description of the impact of a measurement fault vector \mathbf{f} (of same dimensions as \mathbf{z}), whose non-zero elements (described in Section 4.3.2 for step and ramp-type faults) introduce deviations from normal FF conditions. Equation 5.4 becomes:

$$\mathbf{z} = \mathbf{H}\mathbf{x} + \boldsymbol{\varepsilon},$$

where $\boldsymbol{\varepsilon} \equiv \mathbf{v} + \mathbf{f}$.

The RAIM procedure is articulated around two dimensions.

First, the fault vector \mathbf{f} impacts the state estimate error $\delta\mathbf{x}$ defined as:

$$\delta\mathbf{x} = \hat{\mathbf{x}} - \mathbf{x}. \quad (5.8)$$

Let \mathbf{s}_{U,k_F}^T be the row of \mathbf{S} corresponding to the vertical position at the last (i.e., current-time) epoch k_F of the smoothing interval. The corresponding positioning error δx_U due to vector \mathbf{f} is such that:

$$\delta x_U \sim \mathbf{N}(\mathbf{s}_{U,k_F}^T \mathbf{f}, \sigma_U^2). \quad (5.9)$$

The system is said to produce hazardous information if a failure causes a vertical position error that exceeds a vertical alert limit VAL :

$$|\delta x_U| > VAL.$$

Second, the fault \mathbf{f} may be detected using the residual vector \mathbf{r} , defined as:

$$\mathbf{r} = \mathbf{z} - \mathbf{H}\hat{\mathbf{x}}, \quad (5.10)$$

which can be rewritten as:

$$\mathbf{r} = (\mathbf{I} - \mathbf{H}\mathbf{S})\boldsymbol{\varepsilon} \quad (5.11)$$

(see the second part of Appendix E for a reduced-order form that includes prior knowledge on the error states). The norm of \mathbf{r} weighted by the inverse measurement noise matrix \mathbf{V}^{-1} is used as a test statistic:

$$\|\mathbf{r}\|_w^2 = \mathbf{r}^T \mathbf{V}^{-1} \mathbf{r}.$$

$\|\mathbf{r}\|_w^2$ is non-centrally chi-square distributed with $n_z - (4n_k + n_s)$ degrees of freedom (n_z is the length of \mathbf{z}_b , i.e., the length of \mathbf{z} in the reduced-order form) and non-centrality

parameter NCP^2 [Wal95], such that:

$$NCP^2 = \mathbf{f}^T \mathbf{V}^{-1} (\mathbf{I} - \mathbf{H}\mathbf{S}) \mathbf{f}$$

A detection threshold R_C is set in compliance with a continuity requirement P_C to limit the probability of false alarms under fault free conditions [Stu88] (R_C^2 is the value for which the chi-square cumulative distribution function with $n_z - (4n_k + n_s)$ degrees of freedom equals $1 - P_C$). As a result, a measurement failure is undetected if:

$$\|\mathbf{r}\|_w < R_C.$$

The influence of a SSF on both of these dimensions can be represented on a plot of δx_U versus $\|\mathbf{r}\|_w$. The y and x axes of the plot in Figure 5.2 are normalized by VAL and R_C , respectively. The graph's upper left quadrant delimited by $\delta x_U = VAL$ and $\|\mathbf{r}\|_w = R_C$ corresponds to the missed-detection (MD) area (shaded), where failures are both hazardous and undetected. The probability of missed detection P_{MD} is defined as a joint probability:

$$P_{MD} = P(|\delta x_U| > VAL, \|\mathbf{r}\|_w < R_C).$$

Therefore, within the MD area, P_{MD} is the product of the cumulative probability distribution functions of $|\delta x_U|$ and $\|\mathbf{r}\|_w$. The normal and non-central chi-square distributions of respectively δx_U and $\|\mathbf{r}\|_w$ explain the ovoid shape of the contours of constant joint probability density depicted in Figure 5.2 for an example failure mode \mathbf{f} .

The failure mode slope FMS , defined as the ratio of $|\delta x_U|$ over $\|\mathbf{r}\|_w$, is a useful concept that is independent of the fault's magnitude. The resulting failure mode curve

for all magnitudes is a line of slope FMS passing through the origin. On the failure mode plot of Figure 5.2, as the magnitude of vector \mathbf{f} is increased from zero (fault-free case) to some larger value, the point moves along the failure mode line from the origin towards the right of the plot. The detection performance of the integrity threat search algorithm can therefore be evaluated by finding the steepest FMS for a set of failures, and then varying magnitudes along the corresponding line in search for the highest missed-detection probability P_{MD} (corresponding to the worst-case fault).

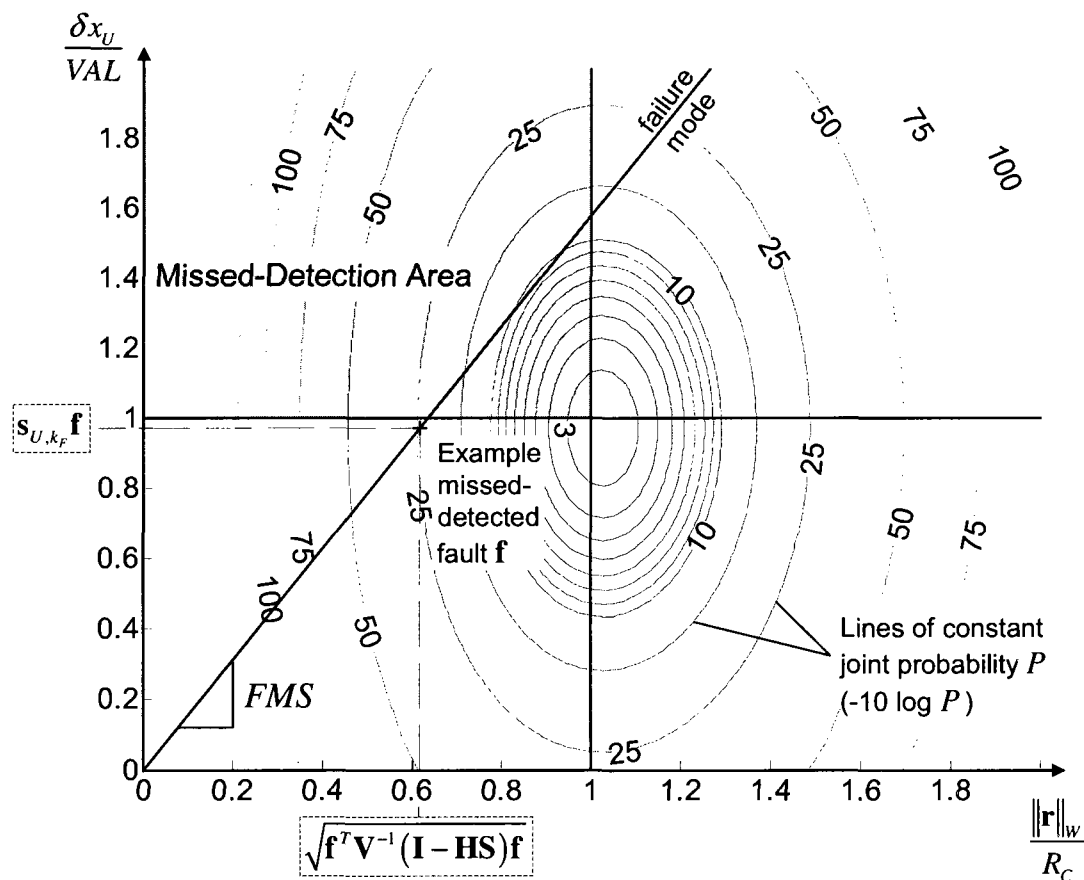


Figure 5.2. Failure Mode Plot

5.3 Further RAIM-based Derivations: Minimum-Residual Fault and RRAIM

Canonical step and ramp-type fault models established in Section 4.3.2 account for the largest part of realistic satellite-related integrity threats. A more direct approach is investigated in Section 5.3.1 by deriving single-satellite faults specifically designed to be the most difficult to detect (i.e., minimizing residuals). In addition, if the fault-detection requirement is not met using the RAIM method and if the mission duration exceeds the smoothing interval T_F , a second layer of integrity monitoring may be implemented using RRAIM (derived in Section 5.3.2).

5.3.1 Minimum-Residual Single-Satellite Fault Derivation. The worst-case fault maximizes position estimate error (most hazardous) while minimizing the residual (most misleading). Fault vectors that belong to the range space of \mathbf{H} (e.g., $\mathbf{f} = \mathbf{H}\mathbf{x}_w$, for any vector \mathbf{x}_w of same length as \mathbf{x}) are strictly undetectable using the residual (\mathbf{r} in equation 5.11 is zero). In fact, the impact of the vector \mathbf{x}_w is entirely transferred onto the state estimate error vector $\delta\mathbf{x}$ (equation 5.10). In general, it has been proven that the estimate error $\delta\mathbf{x}$ and the residual \mathbf{r} are derived from orthogonal components of the fault vector \mathbf{f} [Per97].

Single-satellite faults only affect the few elements of the vector \mathbf{f} corresponding to the SV of interest. Let n_{NZ} be the number non-zero elements in \mathbf{f} (i.e., the number of faulty samples). Following the order in which measurements are stacked in \mathbf{z} , let n_B and n_A be the numbers of measurements respectively before and after the non-zero elements (the total number of measurements n_Z equals $n_B + n_{NZ} + n_A$). The vector \mathbf{f} may be

expressed as:

$$\mathbf{f} = {}^s \mathbf{A} \mathbf{f}_{NZ},$$

where ${}^s \mathbf{A}$ is a $n_Z \times n_{NZ}$ matrix defined as $[\mathbf{0}_{n_Z \times n_B} \quad \mathbf{I}_{n_{NZ}} \quad \mathbf{0}_{n_Z \times n_A}]^T$, and \mathbf{f}_{NZ} is a $n_{NZ} \times 1$ vector of non-zero elements.

In this case, the fault vector \mathbf{f} causing the largest estimate error δx_U can be proven to be ${}^s \mathbf{A} {}^s \mathbf{A}^T \mathbf{s}_{U,k_F}$, but performance analyses show that it is easily detected. Instead, given a matrix ${}^s \mathbf{A}$, the fault generating the smallest residual can be derived by rewriting the non-centrality parameter NCP of $\|\mathbf{r}\|_W$ in terms of \mathbf{f}_{NZ} :

$$NCP^2 = \mathbf{f}_{NZ}^T {}^s \mathbf{A}^T (\mathbf{H}\mathbf{S} - \mathbf{I})^T \mathbf{V}^{-1} (\mathbf{H}\mathbf{S} - \mathbf{I}) {}^s \mathbf{A} \mathbf{f}_{NZ}$$

$$NCP^2 = \mathbf{f}_{NZ}^T {}^s \mathbf{A}^T \mathbf{V}^{-1} (\mathbf{H}\mathbf{S} - \mathbf{I}) {}^s \mathbf{A} \mathbf{f}_{NZ}.$$

The vector \mathbf{f}_{NZ} that minimizes NCP^2 (and therefore $\|\mathbf{r}\|_W$) is the eigenvector corresponding to the smallest eigenvalue of the symmetric matrix ${}^s \mathbf{A}^T \mathbf{V}^{-1} (\mathbf{H}\mathbf{S} - \mathbf{I}) {}^s \mathbf{A}$.

Whereas minimizing the residual might not result in the worst case failure (the derivation did not consider the impact on δx_U), numerical results will show that such fault modes are worse integrity threats than any of the canonical failures.

5.3.2 Relative RAIM for iGPS. The concept of RRAIM was first introduced in the context of the GNSS Evolutionary Architectural Study (GEAS), a research program that aims at analyzing future GPS modernizations at the 2025 horizon [Gra09]. RRAIM assumes that measurement integrity is ensured at some prior time t_0 (either by the ground segment, or by a previous RAIM verification). The precise and unambiguous relative

change in carrier phase observations between times t_j and t_0 is exploited for measurement integrity monitoring at time t_j .

In this work, it seems pertinent to use RRAIM to coast through temporary periods of poor satellite geometries occasionally occurring in the fast changing GPS/Iridium constellation. RRAIM is thought of as a second layer of integrity monitoring: if the current absolute RAIM algorithm at time t_j fails to detect all integrity threats, the RRAIM process is launched. RRAIM is performed using measurements at a previous reference epoch t_0 that is selected going backwards in time until the single-satellite fault integrity requirement can be fulfilled. However, the period T_{RRAIM} , defined as $t_j - t_0$, shall not exceed the maximum interval over which measurement error models are valid (less than 10min).

Performance analyses in Chapter 6 will show that if the integrity requirement can not be met at the current time, there is always a satellite geometry within the past ten minutes that generates better positioning and detection performance. RRAIM enhances the current-time fault-detection capability by exploiting improved past-time geometries.

A position-domain procedure is developed, based on a prior estimate ($\hat{\mathbf{u}}_0$) of the receiver clock deviation and position state vector \mathbf{u}_0 . The vector \mathbf{u}_j at time t_j is obtained from:

$$\mathbf{u}_j = \mathbf{u}_0 + \mathbf{u}_\Delta, \quad (5.12)$$

where \mathbf{u}_Δ is the relative change in receiver clock deviation and position between the two epochs. The only measurement used in the process of estimating \mathbf{u}_Δ , and hence \mathbf{u}_j , is the change in carrier phase observations Φ_Δ .

The stored state estimate vector $\hat{\mathbf{u}}_0$ and its 4×4 covariance matrix $\mathbf{P}_{\mathbf{u},0}$ are the elements of $\hat{\mathbf{x}}$ and $\mathbf{P}_{\mathbf{x}}$ in equations 5.5 and 5.7 corresponding to the receiver clock deviation and position at time t_0 . They were computed using a sequence of observations collected between $t_0 - T_F$ and t_0 . In addition, let \mathbf{v}_0 be a $n_z \times 1$ vector equal to \mathbf{v} in the batch measurement equation 5.4, and \mathbf{S}_0 a $4 \times n_z$ matrix made of the four rows of \mathbf{S} (defined in equation 5.6) corresponding to the states in \mathbf{u}_0 .

The estimate $\hat{\mathbf{u}}_0$ may be slightly biased because of a tolerable single-satellite fault, occurring during the smoothing interval at t_0 , and going undetected. The bias is conservatively accounted for by first identifying the fault \mathbf{f}_0 that generates the largest position error, while its residual \mathbf{r}_0 at time t_0 is such that: $\|\mathbf{r}_0\|_w < R_C$. Then, to ensure that the fault vector \mathbf{f}_0 is conservatively considered, its impact on the residual at time t_j (computed below) is assumed null. In other words, the impact of \mathbf{f}_0 on the estimate error is accounted for, but no credit is taken for its contribution to detection. In practice, the fault mode and magnitude of \mathbf{f}_0 is determined using the RAIM methodology. The fault vector \mathbf{f}_0 in the state space is noted \mathbf{b}_0 ($\mathbf{b}_0 = \mathbf{S}_0 \mathbf{f}_0$). Therefore, the vector $\hat{\mathbf{u}}_0$ is a biased and noisy estimate of \mathbf{u}_0 :

$$\hat{\mathbf{u}}_0 = \mathbf{u}_0 + \mathbf{S}_0 \mathbf{v}_0 + \mathbf{b}_0. \quad (5.13)$$

It is worth noticing that: $\mathbf{P}_{\mathbf{u},0} = \mathbf{S}_0 \mathbf{E}\{\mathbf{v}_0 \mathbf{v}_0^T\} \mathbf{S}_0^T$, where $\mathbf{E}\{\}$ is the expected value operator.

The vector $\boldsymbol{\varphi}_\Delta$ is constructed by differencing the GPS carrier phase measurements from time t_0 to t_j . Let \mathbf{G}_0 and \mathbf{G}_j be the geometry matrices at times t_0 and t_j for the

n_Δ satellite signals that are continuously tracked over the interval T_{RRAIM} :

$$\mathbf{G}_0 = \begin{bmatrix} \mathbf{g}_0 & \cdots & \mathbf{g}_0 \end{bmatrix}^T \quad \text{and} \quad \mathbf{G}_j = \begin{bmatrix} \mathbf{g}_j & \cdots & \mathbf{g}_j \end{bmatrix}^T,$$

The n_Δ signals under consideration may be restricted to GPS signals for which the ionospheric error model is more robust (an upper limit of 2000km is set on IPP displacements, and the piecewise linear vertical ionospheric delay model derived in Section 4.2.2 for Iridium SVs can not be used in this case). In addition, Iridium spacecraft are likely to get out of sight during T_{RRAIM} , and their larger time-differenced measurement error (due to fast satellite LOS motion across the ionosphere) limits their contribution. The change in carrier phase measurements can be written as:

$$\boldsymbol{\varphi}_\Delta = \mathbf{G}_j \mathbf{u}_j - \mathbf{G}_0 \mathbf{u}_0 + \mathbf{v}_{\varphi,\Delta}. \quad (5.14)$$

A careful derivation of $\mathbf{v}_{\varphi,\Delta}$ and of its covariance $\mathbf{V}_{\varphi,\Delta}$ is given in Appendix F. A null quantity is now added to equation 5.14, and terms are rearranged:

$$\boldsymbol{\varphi}_\Delta = \mathbf{G}_j (\mathbf{u}_j - \mathbf{u}_0) + (\mathbf{G}_j - \mathbf{G}_0) \mathbf{u}_0 + \mathbf{v}_{\varphi,\Delta}.$$

Finally, the $n_\Delta \times 1$ measurement vector $\boldsymbol{\varphi}_\Delta$ may be affected by a single-satellite fault \mathbf{f}_Δ (occurring during the interval T_{RRAIM}), so that:

$$\boldsymbol{\varphi}_\Delta = \mathbf{G}_j \mathbf{u}_\Delta + \mathbf{G}_\Delta \mathbf{u}_0 + \boldsymbol{\varepsilon}_{\varphi,\Delta} \quad (5.15)$$

where

$$\mathbf{G}_\Delta = \mathbf{G}_j - \mathbf{G}_0 \quad \text{and} \quad \boldsymbol{\varepsilon}_{\varphi,\Delta} = \mathbf{v}_{\varphi,\Delta} + \mathbf{f}_\Delta.$$

Isolating all available information to the left-hand side, equation 5.15 yields:

$$\boldsymbol{\varphi}_\Delta - \mathbf{G}_\Delta \hat{\mathbf{u}}_0 = \mathbf{G}_j \mathbf{u}_\Delta - \mathbf{G}_\Delta (\mathbf{S}_0 \mathbf{v}_0 + \mathbf{b}_0) + \boldsymbol{\varepsilon}_{\varphi,\Delta}. \quad (5.16)$$

Therefore, the weighted least-squares estimate of \mathbf{u}_Δ is (estimate error is computed next):

$$\hat{\mathbf{u}}_\Delta = \mathbf{S}_\Delta (\boldsymbol{\varphi}_\Delta - \mathbf{G}_\Delta \hat{\mathbf{u}}_0), \quad (5.17)$$

where the matrix \mathbf{S}_Δ is the weighted pseudo-inverse of \mathbf{G}_j defined as:

$$\mathbf{S}_\Delta = (\mathbf{G}_j^T \mathbf{V}_\Delta^{-1} \mathbf{G}_j^T)^{-1} \mathbf{G}_j^T \mathbf{V}_\Delta^{-1}, \quad \text{with} \quad \mathbf{V}_\Delta = \mathbf{V}_{\varphi,\Delta} + \mathbf{G}_\Delta \mathbf{P}_{u,0} \mathbf{G}_\Delta^T. \quad (5.18)$$

The state estimate error vector $\delta \mathbf{u}_0$ is defined according to equation 5.8 and expressed using equation 5.13 as:

$$\delta \mathbf{u}_0 = \hat{\mathbf{u}}_0 - \mathbf{u}_0 = \mathbf{S}_0 \mathbf{v}_0 + \mathbf{b}_0.$$

Also, after substituting equation 5.16 into 5.17, the vector $\delta \mathbf{u}_\Delta$ can be written as:

$$\delta \mathbf{u}_\Delta = \hat{\mathbf{u}}_\Delta - \mathbf{u}_\Delta = \mathbf{S}_\Delta (\boldsymbol{\varepsilon}_{\varphi,\Delta} - \mathbf{G}_\Delta \delta \mathbf{u}_0). \quad (5.19)$$

The expected value $E\{\delta \mathbf{u}_j\}$ of the state estimate error $\delta \mathbf{u}_j$ is computed by substituting equation 5.19 into equation 5.12:

$$E\{\delta \mathbf{u}_j\} = E\{\delta \mathbf{u}_0\} + E\{\mathbf{S}_\Delta (\boldsymbol{\varepsilon}_{\varphi,\Delta} - \mathbf{G}_\Delta \delta \mathbf{u}_0)\}$$

$$E\{\delta \mathbf{u}_j\} = (\mathbf{I}_4 - \mathbf{S}_\Delta \mathbf{G}_\Delta) \mathbf{b}_0 + \mathbf{S}_\Delta \mathbf{f}_\Delta.$$

A lengthier derivation is necessary for the covariance $\mathbf{P}_{u,j}$ of $\delta \mathbf{u}_j$ and is reported in Appendix G. A practical and easy-to-satisfy assumption is imposed, whereby T_{RRAIM} is equal or larger than $2T_M$. The resulting expression is:

$$\mathbf{P}_{u,j} = \mathbf{S}_\Delta \mathbf{V}_{\varphi,\Delta} \mathbf{S}_\Delta^T + (\mathbf{I}_4 - \mathbf{S}_\Delta \mathbf{G}_\Delta) \mathbf{P}_{u,0} (\mathbf{I}_4 - \mathbf{S}_\Delta \mathbf{G}_\Delta)^T.$$

Finally, RRAIM can be implemented as a traditional snapshot RAIM methodology, where simulated fault modes are simply the columns of the matrix \mathbf{I}_{n_Δ} .

- The vertical position estimate error at time t_j is:

$$\delta x_{U,j} \sim N\left({}^3: \mathbf{S}_\Delta \mathbf{f}_\Delta + {}^3: [(\mathbf{I}_4 - \mathbf{S}_\Delta \mathbf{G}_\Delta) \mathbf{b}_0] \ , \ {}^{3,3} \mathbf{P}_{u,j}\right)$$

where the left superscript 3,: designates the third row of a matrix or vector and the superscript 3,3 is the third diagonal element.

- The residual vector is expressed as (applying the definition of equation 5.10 to the measurement equation 5.16):

$$\begin{aligned}\mathbf{r}_\Delta &= (\boldsymbol{\varphi}_\Delta - \mathbf{G}_\Delta \hat{\mathbf{u}}_0) - \mathbf{G}_j \hat{\mathbf{u}}_\Delta \\ &= \mathbf{G}_j \mathbf{u}_\Delta + \mathbf{G}_\Delta \mathbf{u}_0 + \boldsymbol{\varepsilon}_{\varphi,\Delta} - \mathbf{G}_\Delta \hat{\mathbf{u}}_0 - \mathbf{G}_j \hat{\mathbf{u}}_\Delta \\ &= \boldsymbol{\varepsilon}_{\varphi,\Delta} - \mathbf{G}_j \delta \mathbf{u}_\Delta - \mathbf{G}_\Delta \delta \mathbf{u}_0\end{aligned}$$

and using equation 5.19,

$$\mathbf{r}_\Delta = (\mathbf{I}_{n_\Delta} - \mathbf{G}_j \mathbf{S}_\Delta) (\boldsymbol{\varepsilon}_{\varphi,\Delta} - \mathbf{G}_\Delta \delta \mathbf{u}_0).$$

Its norm $\|\mathbf{r}_\Delta\|_w$, weighted by \mathbf{V}_Δ , is non-centrally chi-square distributed with $n_\Delta - 4$ degrees of freedom and non-centrality parameter NCP_Δ :

$$NCP_\Delta^2 = \mathbf{f}_\Delta^T \mathbf{V}_\Delta^{-1} (\mathbf{I}_{n_\Delta} - \mathbf{G}_j \mathbf{S}_\Delta) \mathbf{f}_\Delta,$$

where as mentioned earlier, the conservative assumption is made that the bias vector \mathbf{b}_0 caused by a fault at time t_0 does not contribute to the residual. The detection threshold $R_{C,\Delta}^2$ is the value for which the chi-square cumulative distribution function with $n_\Delta - 4$ degrees of freedom equals $1 - P_c$ under fault free conditions (i.e., $\mathbf{f}_\Delta = 0$).

In this case, the probability of missed detection is defined as:

$$P_{MD,\Delta} = P \left(|\delta x_{U,j}| > VAL, \|\mathbf{r}_\Delta\|_w < R_{C,\Delta} \right). \quad (5.20)$$

Unlike in Figure 5.2, the failure mode line caused by \mathbf{f}_Δ does not cross the origin but crosses the y-axis at the value: ${}^{3,3}[(\mathbf{I}_4 - \mathbf{S}_\Delta \mathbf{G}_\Delta) \mathbf{b}_0]$.

In summary, in this chapter, a carrier phase positioning and cycle ambiguity estimation algorithm as well as carrier phase fault detection methods (RAIM and RRAIM) have been derived for iGPS. They can now be evaluated using the measurement error parameter values and the canonical fault models established in Chapter 4, and also the minimum-residual faults presented above. At this stage of the design process, sensitivity analysis of integrity performance to system parameters is essential in providing guidelines for system components that have not been fully defined yet.

CHAPTER 6

IGPS PERFORMANCE ANALYSIS

The expected high-integrity real-time positioning performance of iGPS makes it a potential navigation solution for demanding precision applications such as autonomous land and air transportation. Target requirements, inspired from the most stringent standards in the civilian aviation community, are described in Section 6.1 for the benchmark mission of aircraft precision approach.

In subsequent sections, the system's ability to meet these requirements is assessed using the estimation and detection algorithms derived in Chapter 5. First, Section 6.2 investigates the impact of Iridium's near-polar-orbit spacecraft geometry on the estimated fault-free positioning performance. Second in Section 6.3, the detection of canonical step and ramp-type single-satellite faults is analyzed using the batch-residual-based RAIM method. Worst-case performance is measured next, by injecting minimum-residual faults into the system. The effect of such integrity threats is efficiently mitigated in Section 6.4 using ground monitoring and using RRAIM.

Finally, a sensitivity analysis is proposed in Section 6.5 that evaluates the relative influence of individual system parameters on the overall end-user output. The methodology compares various system configurations (for the space, ground, and user segments) and singles out system components likely to bring about substantial performance improvement.

6.1 Framework for the Performance Analysis

The iGPS performance evaluations are structured around the benchmark application of aircraft precision approach defined in Section 6.1.1. Then in Section 6.1.2, performance criteria are established in compliance with demanding aviation standards [MAS04] and with the integrity allocation tree of Figure 4.8. Finally in Section 6.1.3, nominal simulation parameters are derived in order to generate results that are representative of the average system performance. In particular, an approximated period is computed over which the joint GPS-Iridium constellation repeats itself for any fixed location on earth.

6.1.1 Benchmark Aircraft Precision Approach Application. The benchmark application of precision approach for civilian aircraft is illustrated in Figure 6.1. An airplane equipped with a GPS/Iridium receiver is following a simplified straight-in trajectory: it is flying at a constant speed of 70m/s with a 3deg glide-slope angle towards the runway until touchdown (TD) where lateral and vertical requirements apply (symbolized by a rectangle). The focus in this work is on the vertical position coordinate (for reasons given in Section 5.1). Measurement processing over the filtering interval T_f is simulated for position estimation at TD. Protection levels (PL) are defined below and analyzed when assessing the fault-free performance.

6.1.2 Requirements and Availability Performance Criteria. In this work, system performance is measured in terms of availability of a high-integrity vertical position solution.

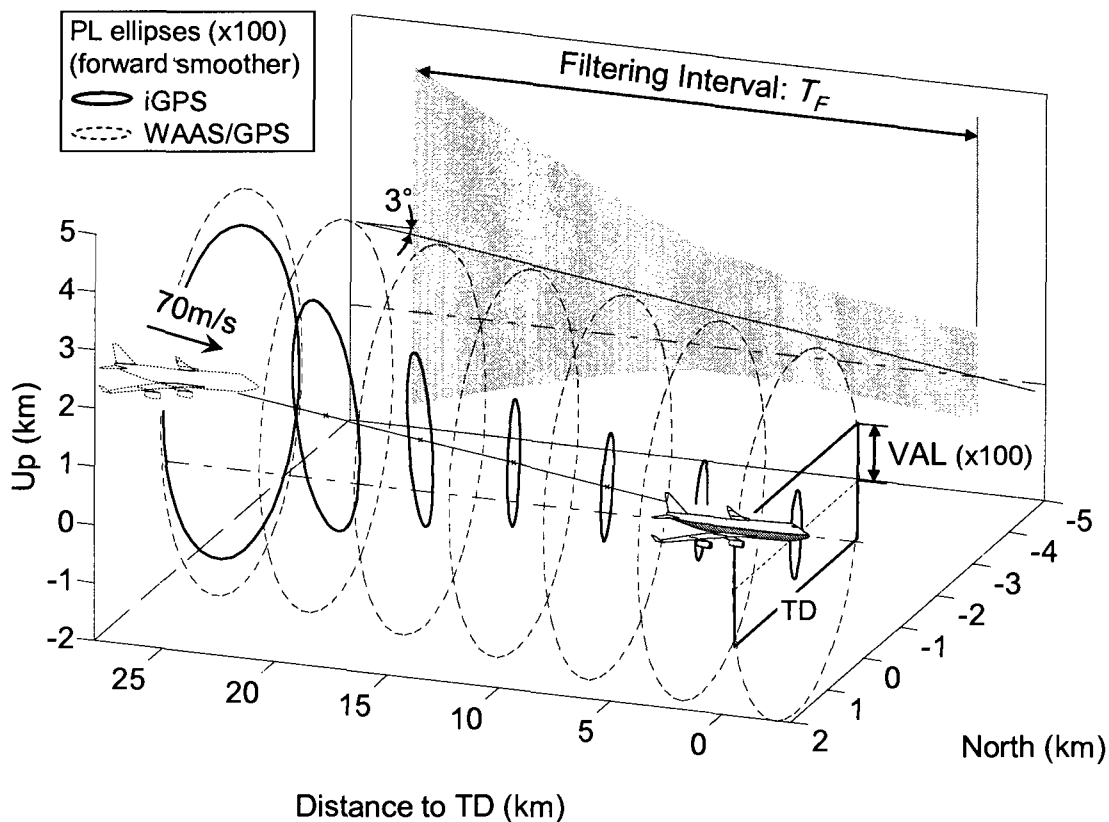


Figure 6.1. Final Approach Simulation Description (Case 'Standard' in Figure 6.3)

The overall integrity risk requirement P_{HMI} is defined in Section 4.4. For the application of interest, it specifies that when the aircraft's pilot has near-zero visibility to the runway, no more than one event leading to hazardous misleading navigation information is allowed in a billion approaches ($P_{HMI} = 10^{-9}$) [MAS04]. As described in Figure 4.8 for the standalone RAIM architecture, the required probability P_{HMI} is subdivided between cases of multiple simultaneous measurement faults (P_ϵ), normal fault-free conditions (FF: $\alpha(P_{HMI} - P_\epsilon)$) and rare-event single-satellite faults (SSF: $(1 - \alpha)(P_{HMI} - P_\epsilon)$).

Under normal conditions, the vertical protection level VPL , a statistical over-bound on the positioning error in the Up-direction, is defined as a function of the standard deviation of the vertical position coordinate σ_U (derived in Section 5.1):

$$VPL = \kappa_{FF} \cdot \sigma_U,$$

where the probability multiplier κ_{FF} corresponding to $\alpha(P_{HMI} - P_\epsilon)$ is a confidence-level coefficient (it is the value for which the normal cumulative distribution function equals $1 - \alpha(P_{HMI} - P_\epsilon)/2$). In accordance with civilian aviation standards, which specify a vertical alert limit VAL of 10m from 200 feet of altitude to TD, an approach (corresponding to a specific satellite geometry) is deemed available under FF conditions if and only if:

$$VPL < VAL. \tag{6.1}$$

Rare-event faults such as equipment and satellite failures (whose rate FR of approximately $4 \cdot 10^{-9}/s$ was defined in Section 4.3.2) become significant threats when aiming at ensuring an integrity risk $(1 - \alpha)(P_{HMI} - P_\epsilon)$ on the order of 10^{-9} . The RAIM methodology (Section 5.2) is implemented to evaluate the impact of such faults. The detection threshold is set in compliance with a continuity requirement P_C of $2 \cdot 10^{-6}$ to limit the probability of false alarms [MAS04] (requirements are all summarized in Table 6.1). For each simulated fault type (bias, ramp and impulse), the RAIM algorithm determines the fault causing the highest probability of missed detection P_{MD} over all satellites (identified with the subscript sv), all fault magnitudes (subscript mag) and all fault breakpoints (i.e., starting times, with a subscript bkp). In order to speed up the screening of simulated faults, two SSF-availability criteria are established. The first

conservative criterion specifies that:

$$\max_{sv, mag, bkp} (P_{MD}) FR \cdot T_F < (1 - \alpha)(P_{HMI} - P_\epsilon). \quad (6.2)$$

For clarity of notation, the maximum P_{MD} (left-hand side term) is implicitly summed over all fault types (subscript typ):

$$\max_{sv, mag, bkp} (P_{MD}) \equiv \sum_{typ} \left(\max_{sv, mag, bkp} (P_{MD, typ}) \right).$$

The criterion of equation 6.2 is conservative because it assumes that the probability P_{MD} maintains its highest level over the entire exposure period T_F . In fact, the maximum P_{MD} varies considerably over T_F : analyses in Section 6.3 will show that there is a sharp peak in maximum P_{MD} for faults whose breakpoint occurs at a particular time, i.e. within a small interval T_B (the interval between simulated breakpoints). In this case, the probabilities $P_{MD, bkp}$ must be summed for all fault breakpoints:

$$\sum_{bkp} \max_{sv, mag} (P_{MD, bkp}) (FR \cdot T_B) < (1 - \alpha)(P_{HMI} - P_\epsilon). \quad (6.3)$$

The computation of the left-hand-side term of equation 6.3 is time-consuming, but it only needs to be performed if the conservative criterion of equation 6.2 is not met. Finally, if equation 6.3 is not satisfied, the approach or geometry is deemed SSF-unavailable.

In the case where RRAIM is implemented, a fraction of the SSF integrity budget equal to $\beta(1 - \alpha)(P_{HMI} - P_\epsilon)$ is put aside for RRAIM, so that the remaining fraction for absolute RAIM becomes $(1 - \beta)(1 - \alpha)(P_{HMI} - P_\epsilon)$. The coefficient β ranges between 0 and 1 (β equals 0 if RRAIM is not used) and is selected to maximize the SSF performance. Equation 6.3 (for absolute RAIM) becomes:

$$\sum_{bkp} \max_{sv,mag} (P_{MD,bkp}) (FR \cdot T_B) < (1-\alpha)(1-\beta)(P_{HMI} - P_\epsilon). \quad (6.4)$$

If this criterion can not be fulfilled at the current time-step t_j , a RRAIM check is carried out based upon a position fix from a previous epoch t_0 where equation 6.4 was satisfied. The probability of missed detection $P_{MD,\Delta}$ (equation 5.20) of a fault affecting the differenced carrier phase measurement over the T_{RRAIM} exposure period ($T_{RRAIM} = t_j - t_0$) must satisfy the following equation:

$$\max_{sv,mag} (P_{MD,\Delta}) (FR \cdot T_{RRAIM}) < \beta(1-\alpha)(P_{HMI} - P_\epsilon). \quad (6.5)$$

Equations 6.1 and 6.3 (or 6.1 and 6.4 to 6.5 for RRAIM) are the expressions of FF and SSF binary criteria that either validate or nullify availability for an approach. In Sections 6.2 to 6.5, approaches starting at regular intervals are simulated for sequences of satellite-user geometries, over a period T_{AV} defined below. Ultimately, the percentage of available approaches is the measure of iGPS FF and SSF performance.

Table 6.1. Summary of Requirements

Parameter	Description	Nominal
P_{HMI}	Integrity risk	10^{-9}
P_C	Continuity risk	$2 \cdot 10^{-6}$
VAL	Vertical alert limit	10m
FR	Single satellite failure rate	$\sim 4 \cdot 10^{-9}/s$
α	FF integrity risk coefficient	10^{-3}
β	RRAIM integrity risk coefficient	10^{-1}

6.1.3 Simulation Parameter Calibration for the Availability Analysis. iGPS performance is first established for a nominal system configuration, conservatively selected to produce reliable availability results for a near-term future iGPS architecture (i.e., for a single-frequency iGPS user receiving WAAS-like ground corrections as described in Section 4.2.5). The Miami location is selected, because the Iridium satellite geometry at this southern latitude is one of the poorest for CONUS. In addition, a nominal smoothing period T_F of 8 minutes is chosen to investigate availability performance variations (the estimated 10min upper limit ensuring measurement error validity is respected). A 30s sampling interval T_p within the smoothing period T_F was selected in Section 5.1. Also, the interval T_b between simulated fault breakpoints is maximized (to reduce computation time) under the condition that SSF availability variations with respect to smaller T_b values do not exceed 0.05%. A summary of simulation parameters is given in Table 6.2.

Table 6.2. Summary of Nominal Simulation Parameters

Parameter	Description	Nominal
T_F	Filtering period	8min
T_p	Sampling interval (different from positioning interval)	30s
T_{AV}	Availability simulation period	3 days
	Interval between simulated approaches	30s
T_b	Interval between simulated fault breakpoints	5s
Location	Near-worst case (25.5deg North, -81.1deg East)	Miami
Signals	Single-frequency (SF) or dual-frequency (DF)	SF
	GPS constellation	24 SVs
	Iridium constellation	66 SVs

Of particular importance when combining measurements from multiple constellations is the duration T_{AV} over which availability simulations are carried out. The period T_{AV} should enable sampling of a complete set of satellite geometries. For GPS, T_{AV} is one sidereal day (the earth's rotation period in an ECI frame, which equals $2T_{GPS}$). It corresponds to the time-period the constellation needs to completely repeat itself with respect to the earth.

The orbital period for Iridium T_{IRI} is 6028s. The combined GPS/Iridium constellation repeatability period with respect to the earth can be easily calculated if secular variations due to the earth's oblateness are neglected. Secular effects prove to be very small both for GPS and Iridium due respectively to the high-altitude and to the high-inclination of their orbits. Hence, it takes 1,507 sidereal days (more than 4 years) for the geometry between the earth, GPS and Iridium satellites to completely repeat itself. Simulating the algorithms over 1,507 days is computationally too intensive.

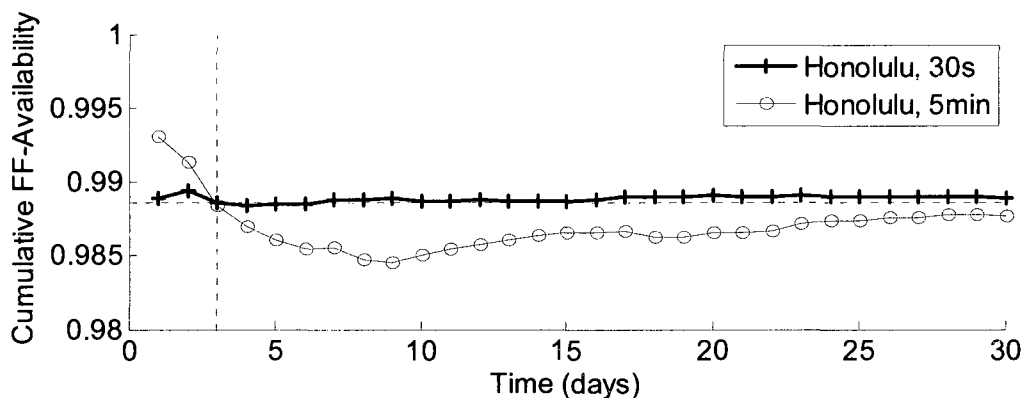


Figure 6.2. Determination of T_{AV}

Fortunately, an approximated duration representative of a large number of geometries can be utilized. In fact, Iridium satellites circle the earth exactly 43 times in three solar days and four seconds. Also, the remainder of the closest integer number of intervals T_{IRI} within $n \cdot 2T_{GPS}$, where n is a series of consecutive integers, exhibits a three to four day cyclic trend. Finally, Figure 6.2 demonstrates that the computed cumulative FF-availability averages out after a few days, for the nominal system configuration at the Honolulu location (FF-availability is less than 100% at this low latitude of 21.31deg). The maximum deviation relative to the accumulated value after three days stays within 0.05% over one month of simulation. Concurrently, it is important that the interval between simulated approaches be selected short enough as illustrated with the 30s and 5min interval curves. In view of these results, approaches are simulated every 30s over a period T_{AV} of three days.

6.2 Fault-Free Availability Analysis

The preceding section has set the framework for performance evaluations. As expressed in equation 6.2, fault-free availability is determined by the output of the estimation algorithm. The impact of geometric diversity on carrier phase cycle ambiguity estimation is investigated for a single approach in Section 6.2.1, and for sequences of satellite geometries over the three day T_{AV} period in Section 6.2.2. The contribution of code phase GPS and Iridium measurements to the estimation algorithm is also discussed in Section 6.2.3.

6.2.1 Single Approach Analysis. The aircraft precision approach mission is illustrated in Figure 6.1. Covariance ellipses, derived using the recursive KF, represent the protection levels (PLs) in the North and Up coordinates at different time steps. Position estimate standard deviations are multiplied by the probability coefficient κ_{FF} (equation 6.2), and inflated by a constant scaling factor for the clarity of the plot. Their shape and size change with geometry, mainly because of Iridium satellite motion. A gray area for the corresponding vertical position covariance envelope along the aircraft trajectory is projected in the background. This example illustrates the incremental improvement in positioning accuracy within the filtering interval T_F , and the dramatic enhancement of iGPS over WAAS/GPS, for which the position error barely changes. In this case, the iGPS solution meets the FF-integrity requirements, meaning that the ellipse at TD is fully contained inside the specified rectangle of alert limits.

The estimation algorithm performance is further analyzed to understand the impact of satellite geometries on carrier phase positioning. Cycle ambiguity estimation for mobile users (sometimes referred to as kinematic on-the-fly estimation [Rem93]) requires SV redundancy as well as variations in user-to-satellite lines of sight [Hwa91], both of which are provided by augmenting GPS with Iridium. In general, position and cycle ambiguity estimates improve as the change in LOS angle increases [Per96] [Rab00]. The example geometry depicted in Figure 4.2b underscores the sharp contrast between an Iridium satellite whose angular variation over 10min exceeds 130deg, and GPS satellites whose LOS rotation barely reaches 5deg.

6.2.2 Analysis over Multiple Satellite Geometries. A similar argument on observability helps explain the influence of angular variations on individual position coordinates (in the East, North and Up directions). In this availability analysis, a total of 8620 different approaches (i.e., sequences of satellite geometries) are simulated at the Miami location, and for the nominal system configuration summarized in Tables 4.1, 6.1 and 6.2. All approaches (100%) are available in this fault-free scenario.

iGPS performance is first evaluated for comparison with WAAS/GPS. In Figure 6.3a, a 15-hour period is extracted out of the total 72-hour simulation period T_{AV} in order to better visualize the variations in VPL. As mentioned above, filtering WAAS/GPS measurements over the period T_F brings very little positioning improvement. VPL variations for WAAS/GPS are therefore nearly proportional to the vertical dilution of precision (or VDOP – the GPS VDOP in Figure 6.3a is averaged over T_F).

Then, parallels are established between iGPS VPL variations and Iridium satellite availability (thick solid curves). The average number of Iridium satellites in view over T_F (the sum of visible Iridium SVs at each epoch divided by the number of epochs T_F/T_p) is displayed in Figure 6.3a for each simulated approach. The first finding is that neither the number of GPS satellite signals nor the VDOP influence iGPS VPL results as significantly as the number of Iridium spacecraft.

In this regard, three regions are identified in Figure 4.1 to distinguish different areas of Iridium satellite visibility at Miami's latitude:

- Region A is located at the seam of the constellation, where the orbital plane separation-angle is smaller, so that the number of Iridium satellites in view is higher than elsewhere.

- Regions of type B are located in-between co-rotating orbital planes and benefit from the coverage of LEO satellites from both planes.
- Regions of type C designate areas around orbital planes, covered by only one or two LEO satellites from a single plane at a time.

Moving along a parallel at Miami's latitude, regions of types B and C succeed to each other, presenting respectively 1-3 and 1-2 visible satellites at a time.

Over time, the earth rotates about its axis in an ECI-frame while SVs move in their quasi-stationary orbital planes. So regions of types B and C in Figure 4.1 correspond to intervals of time in Figure 6.3a. Type-B periods alternate with type-C periods and the average number of visible satellites during these intervals varies between about 2.2 and 1.3 satellites respectively. The number of satellites increases every half sidereal day during type-A intervals. This increase is more pronounced on one end of the seam than on the other (around the 15hr point) because of the less-than-90deg Iridium orbital plane inclination. Users at Miami's latitude all experience patterns similar to Figure 6.3a, which are shifted in time depending on their longitude.

The first obvious parallel between FF-performance and Iridium satellite visibility is that during intervals of type A, numerous Iridium measurements logically produce lower VPLs. A close look at the high-frequency variations of both curves (with a less than 10min period) shows that peaks in VPLs, especially during phases of types A and B, correspond to valleys in average number of visible Iridium satellites (this again, regardless of GPS geometry).

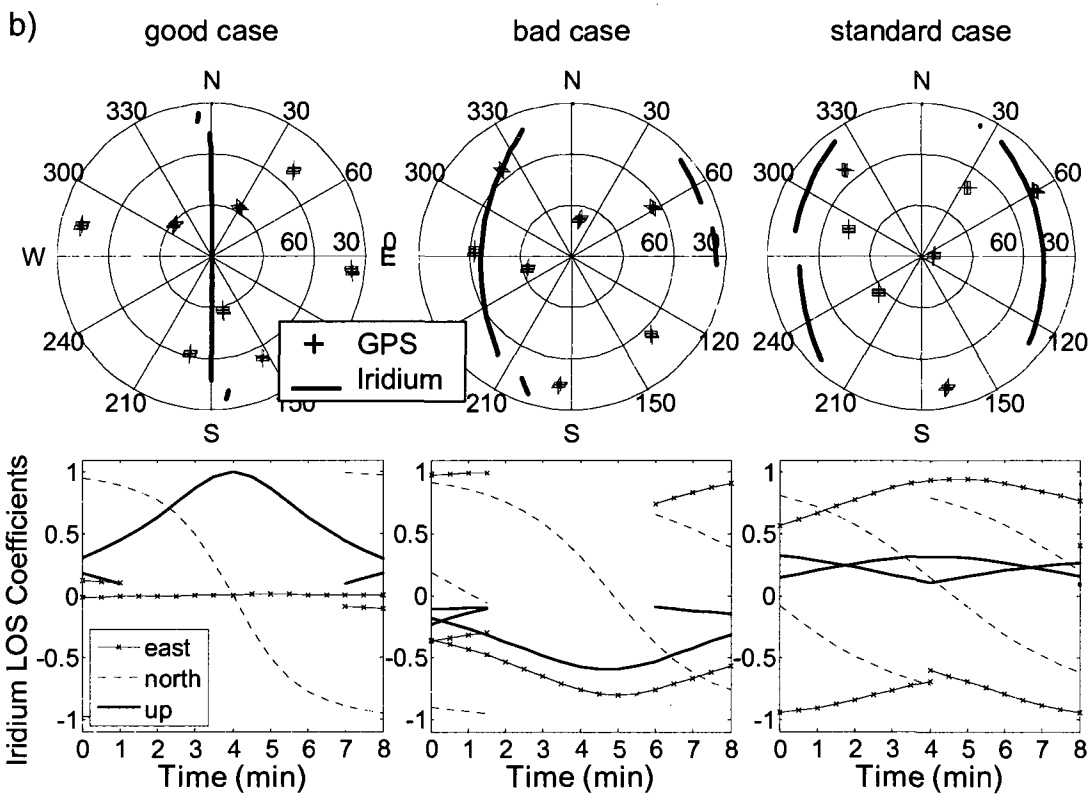
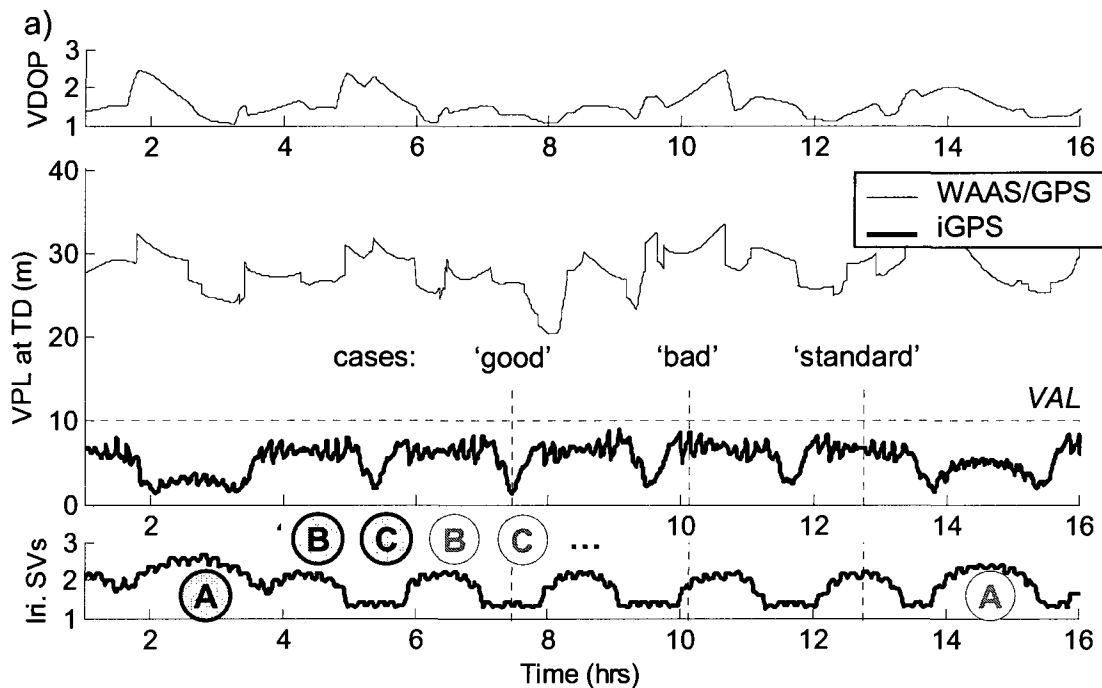


Figure 6.3. Fault-Free Availability Analysis

Another strong observation is that the highest VPL peaks occur around the beginning or the end of type-B intervals. This is verified over the 3-day T_{AV} period for a wide range of system parameters. In addition, what seems paradoxical is that sharp drops in VPLs are achieved during intervals of type C, where the average number of Iridium satellites is the lowest.

To further examine these two points, three characteristic cases are investigated: a ‘good’ case, a ‘bad’ case, and a ‘standard’ case. For each case, Figure 6.3b introduces azimuth-elevation sky plots of the SV trajectories over the 6min filtering period T_F , and Iridium satellite LOS variations along each of the three local position coordinates.

- Case (good), the best of the three cases, occurs in the middle of a type-C interval: one LEO satellite is traveling directly overhead the user, so that the variation in LOS coefficient corresponding to the vertical coordinate is the largest.
- Case (bad), the worst of the three, is at the beginning of a type-B phase. Two mechanisms have been identified, that explain the poor performance. First, the amount of angular variation with respect to the vertical direction is decreased relative to the previous case. Second, an observability issue appears that prevents accurate bias estimation: unlike the two other cases, the angular variations in the East and Up coordinates have become difficult to distinguish for the single satellite that is visible over most of the period T_F . The corresponding states remain undetermined, causing a peak in VPL.
- Finally in the standard case, in the middle of a type-B interval, additional low-elevation satellites from the adjacent orbital plane come in sight, slightly

augmenting the cumulated amount of angular variations and above all, resolving the East-Up ambiguity.

In summary, excellent vertical positioning performance is obtained when a satellite crosses the sky directly overhead the user, where angular variations with respect to the vertical axis are the most substantial. As time passes, the user's location drifts away from the orbital plane due to earth rotation, causing vertical LOS variations to decrease with Iridium satellite elevation. Then, for a few spacecraft trajectories, occasional observability issues arise from the difficulty to distinguish variations in the East and Up directions. Additional low-elevation satellites come in view as the user location approaches the adjacent plane, which solves the observability problem, and provides improved geometric diversity.

Practical lessons learned from this exercise are for example, that if Iridium satellites were added for navigation purposes, the constellation should be re-arranged to include extra orbital planes with tighter separation angles, rather than launching more SVs in the existing planes. Results for an 88-Iridium-satellite constellation (with eight orbital planes instead of six) are presented in Section 6.5. Another costless and straightforward way to improve FF-performance is to increase the filtering period T_F (within the 10min upper limit) in order to include extra range variations. Using an interval T_F of 8min, 100% FF-availability is achieved at the Miami location.

6.2.3 Influence of Code Phase Measurements. Code phase observations provide absolute ranging information, which plays a considerable part in the cycle ambiguity estimation process, especially in cases of poor satellite geometry. To illustrate this

statement, VPLs are recomputed in Figure 6.4 (for the nominal configuration at the Miami location) without using Iridium code measurements (upper chart) and without GPS code pseudoranges (middle chart). The average number of Iridium SVs over time is reproduced in the lower chart (same curve as in Figure 4.3a).

The VPL saw tooth pattern in the upper chart (without Iridium code) is driven by the geometric diversity provided by Iridium carrier phase signals. Low VPLs are achieved when the user location is close to an Iridium orbital plane (middle of type-C phases). VPLs increase gradually as the user location moves away from the orbital plane (due to earth rotation) until a local maximum is reached right in between two planes (middle of type-B intervals). A comparison with the nominal case (thin curve) reveals the contribution of Iridium code phase measurements. Their coarse absolute ranging accuracy, combined with GPS code and GPS and Iridium carrier phase observations, is sufficient to bring VPLs below the 10m VAL.

In the middle graph of Figure 6.4, the absence of GPS code measurements results in peaks of VPL occurring between type-B and type-C intervals. These intervals were previously identified as ‘bad’ cases of Iridium satellite geometries, where biases in the East and Up position coordinates were unobservable. Therefore, without the rough user position estimate obtained from GPS code measurements, rapid cycle ambiguity estimation becomes extremely challenging. Even though Iridium signals carry the most weight in the estimation (see the results with and without Iridium in Figure 4.3), code and carrier phase measurements from both constellations are instrumental in achieving high-integrity FF performance.

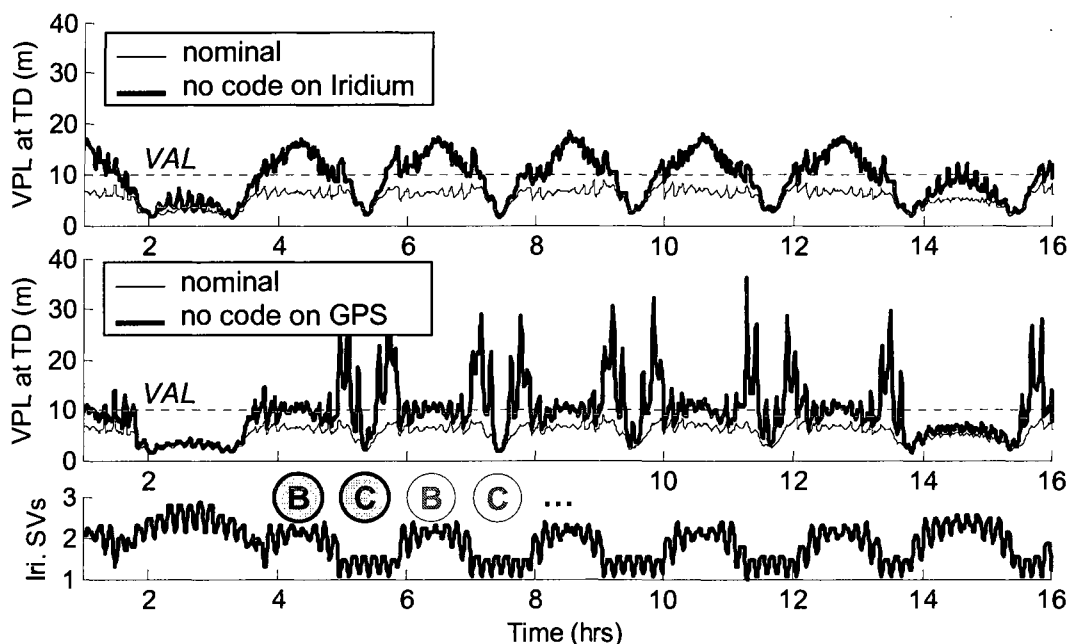


Figure 6.4. Influence of Code Phase Measurements

6.3 Undetected Single-Satellite Fault Analysis

The RAIM-type single satellite fault detection process is tested against measurement impulses, steps and single-breakpoint ramps of all magnitudes and starting times, for simulated approaches repeated every 30 seconds over the 3 day T_{AV} -period. The nominal system configuration enables 100% FF-availability but does not prevent SSF-unavailable approaches at the Miami location (98.1% availability is achieved under SSF conditions). A value of 10^{-3} is assigned to the coefficient α in order to maximize the fraction of the integrity risk allocated to SSF detection without reducing the FF performance (see Table 6.1).

Fault-modes causing SSF-unavailability can be identified. First, results show that impulse and step-type faults are systematically detected. They generate large residuals,

even for low failure magnitudes, which translates into a gentle slope on a failure mode plot (Figure 5.2).

All 164 unavailable approaches, out of 8620 simulated cases, are due to ramp-type faults on Iridium carrier phase measurements. Carrier phase observations are the most sensitive because they carry the most weight in the estimation algorithm (they have a low tracking error – Section 2.3.3) as opposed to code-phase measurements, which if corrupted but undetected, are typically not hazardous to the final position estimate. For the same reason, faults on Iridium signals have a more dramatic impact than faults on GPS.

Further examination suggests that integrity threats causing missed-detection can be related to a simple physical quantity: the undetected fault profile matches that of range variations on the faulty satellite. To the detection algorithm, the fault appears as a scaled version of the measurement. In other words, the fault is masked by a fault-free behavior.

- In general, ramp-type faults that don't match the range variation are detected, which is the case for most faults that include breakpoints. Elements of the residual vector \mathbf{r} corresponding to measurements collected just before and just after the breakpoint exhibit sharp magnitude variations, hence inflating the detection test statistic $\|\mathbf{r}\|_w$.
- The overwhelming majority of undetected threats are uninterrupted ramps over the entire satellite pass affecting Iridium SVs visible for short periods (for only part of the filtering interval). In fact, the longest undetected failures do not stretch over more than 6 minutes, which is about half the maximum

duration of an Iridium satellite pass (e.g., from rise to maximum elevation), and beyond which its range variation is no longer ramp-like.

- In the rare cases where a fault that includes a breakpoint goes undetected, the breakpoint has to precisely match the change in the faulted satellite range variation. Simulations show that breakpoints that are offset by 10-20s generate residuals large enough to trigger detection.

Fault and range-variation profiles are pictured in Figure 6.5 for an example undetected ramp-type fault (left-hand-side plots) and for an example minimum-residual fault that will be discussed later (right-hand-side).

The RAIM method, in addition to verifying SSF-availability (by finding the fault magnitude generating the highest probability P_{MD}), allows for the boundaries of the integrity threat space to be determined (i.e., the minimum and maximum fault magnitudes for which P_{MD} violates equation 6.3). Simulations indicate that the slopes of the 164 ramps causing SSF unavailability range from 6.9mm/s to 31.3mm/s over 2-6min periods. Further research will determine whether physical phenomena actually exist that may cause such faults, and how likely they are to occur.

In addition, as illustrated in the FF analysis of Figure 6.3, cases of poor geometries are isolated, and do not last long. Accordingly, SSF-availability results show that navigation service outages last on average 1.3min, with a maximum of 3min, meaning that users would never have to wait more than 3min to recover the required performance.

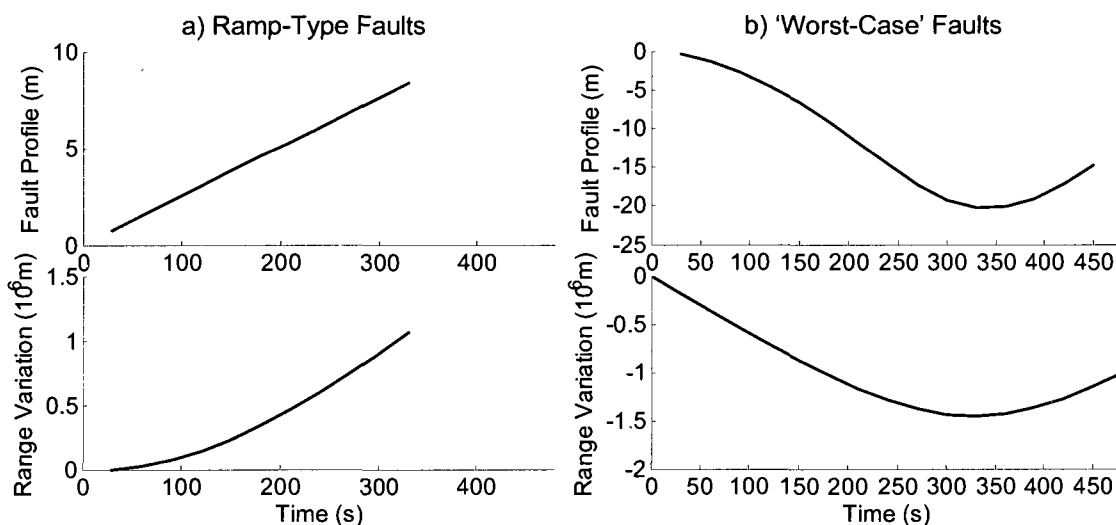


Figure 6.5. Worst Ramp-Type Fault and Minimum Residual Fault

As explained in Section 4.3.2, results for this set of canonical faults provide a preliminary assessment of the system's detection performance against single-satellite failures. Ultimate validation of fault detection performance must be verified against a comprehensive set of all realistic fault modes. An alternative approach is explored in the next section, which consists in evaluating the worst-case detection performance.

6.4 Complementary RAIM-based Analyses

The limits of the detection algorithm are evaluated in Section 6.4.1 using previously derived fault modes that minimize the residual. The resulting SSF performance is much deteriorated. In response, ground monitoring and RRAIM processes are investigated respectively in Sections 6.4.2 and 6.4.3.

6.4.1 Minimum Residual Fault Detection Analysis. Minimum residual fault modes derived in Section 5.3.1 are computed for all satellites and for all starting times during the

filtering interval. An example fault causing unavailability is plotted in Figure 6.5 (upper right-hand-side plot). Its profile was derived specifically to minimize the residual, meaning that it is the most difficult single-satellite fault to detect for this geometry. It turns out that the curvature is similar to the faulty satellite's range variation, which confirms the analysis of Section 6.3.

SSF availability is severely impacted when injecting minimum residual faults into the system. The performance drops from the nominal value of 98.1% (when evaluated against canonical fault models, for the nominal configuration at the Miami location) to 40.7%. Even when increasing the filtering interval T_f from 8min to 10min (the upper limit set in Section 4.2.5 to ensure measurement error model validity), SSF-availability reaches 100% against canonical faults versus 77.2% against minimum residual faults. Still, in the latter case, the average availability outage duration remains lower than 2min and never exceeds 5min. The user may be protected from such faults using integrity information sent from ground reference stations, or using RRAIM.

6.4.2 Impact of Ground Monitoring. Section 4.4.1 briefly introduced a ground-assisted RAIM architecture, which exploits the ground station's information and equipment resources to protect the user's navigation solution. However, this approach is constraining because once a fault has been detected at the ground, the user must be warned in time to take action. In the example of aircraft final approach, the warning must reach the pilot soon enough to abort the mission.

The time to alarm (TTA) requirement is always fulfilled in the standalone-RAIM approach simulated so far, because detection-to-warning delays amount to negligible

computation delays. In contrast, in the ground-assisted RAIM architecture, TTA becomes a major parameter of the system design because ground monitors need to detect the faults and alarms must be communicated to distant users via ground or space-based data-links. Under the assumption that ground monitors could guarantee the integrity of past measurements (up to the current time t_j minus the specified TTA, i.e., $t_j - TTA$), the availability performance can be re-evaluated. In this case, the RAIM algorithm is used to relax the TTA requirement (small TTA's are challenging to achieve), and ensures integrity between times $t_j - TTA$ and t_j .

In Figure 6.6, all faults starting before $t_j - TTA$ are assumed detected by ground monitors. The remaining set of faults is injected into the RAIM detection algorithm. One quarter of the overall integrity requirement is allocated to ground monitoring, so that SSF availability is computed using the remaining 75% of P_{HMI} , against minimum residual faults, and for a smoothing period T_F of 10min. Results for the nominal configuration at the Miami location suggest that the TTA requirement can be set as large as 4min and still ensure maximum SSF availability. In comparison, a 6s TTA requirement is specified for WAAS-based aviation applications, which is extremely constraining. Ground requirements might be further relaxed, or even deemed unnecessary, when implementing RRAIM.

6.4.3 RRAIM Analysis. The RRAIM algorithm described in Section 5.3.2 enables coasting through periods where integrity requirements are not fulfilled using the RAIM detection function. Unlike ground monitoring, it does not add any constraint on the computation and communication system between ground and user segments.

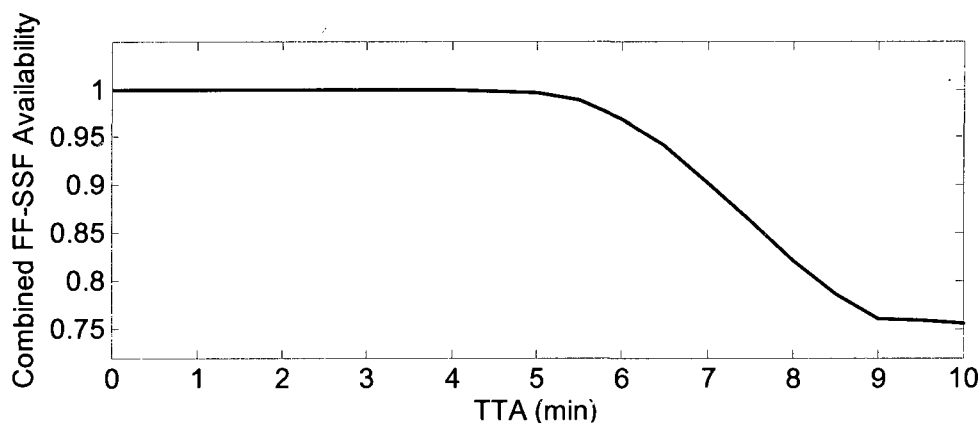


Figure 6.6. Impact of Ground Monitoring

The pertinence of RRAIM for iGPS was initially inspired by the high-frequency profile of VPL variations in Figure 6.3, and is reaffirmed by the maximum navigation service outage duration that never exceeds 5min using the traditional ‘absolute’ RAIM method. This means that there is always an improved satellite geometry within the past 10min (the limit set for validity of the error models) that can be used as a RAIM-validated fault-free reference epoch. Any fault occurring between that reference epoch and the current time may be detected using RRAIM.

RRAIM is evaluated against minimum residual faults, for a period T_F of 10min (for the nominal configuration at the Miami location). The availability performance increases from 77.2% for absolute RAIM to 99.7% when RRAIM is implemented. As a result, the combination of absolute RAIM and RRAIM may become the standard implementation in future phases of the project. The remainder of the chapter only considers the absolute RAIM algorithm, tested against canonical fault models over the nominal 8min filtering period T_F .

6.5 Combined FF-SSF Availability Sensitivity Analysis

Sensitivity analysis results are presented in terms of ‘combined availability’, which is only granted for an approach if both the FF and SSF criteria are satisfied. Despite a small value assigned to the coefficient α (in Table 6.1), the SSF criterion remains the driving factor for loss of availability. Performance is evaluated using the canonical impulse, step and ramp-type fault models. Parameter values for the nominal configuration (Tables 4.1, 6.1 and 6.2) are used as a reference for comparisons, and are conservatively selected to describe a system architecture implementable in the short term. The nominal combined availability performance (for the 8min-long filtering period T_F) is 98.10% at the Miami location, which is a near-worst-case location in CONUS.

6.5.1 Sensitivity to Measurement Error Model Parameters. The performance sensitivity to individual error model parameters is investigated for realistic ranges of values in Figure 6.7. More precisely, the combined FF-SSF availability at the Miami location, for a fixed smoothing interval T_F of 8min, is plotted for each parameter’s nominal standard deviation σ_{NOM} (listed in Table 4.1 – e.g. for VIB, σ_{NOM} is σ_{VIB}) inflated by $i/5$, where i is an integer ranging from 1 to 9. As expected for all parameters, values lower than σ_{NOM} produce better results than the nominal case, and conversely availability decreases for higher values.

Three parameters stand out as being the most influential. First, the standard deviation of the vertical ionospheric bias σ_{VIB} generates the largest performance variations. Assuming WAAS-like ground corrections under non-anomalous ionosphere

conditions at mid-latitudes, a nominal value of 1.5m was selected for σ_{VIB} (Section 4.2.2). The need for ionospheric corrections determines in large part the scale of the ground infrastructure, which motivates further analysis below.

GPS orbit ephemeris and clock deviations are the second largest cause of performance variations. The nominal 2m parameter value for $\sigma_{ECB-GPS}$, representative of GPS ephemeris and clock errors after OCS and WAAS-like corrections, was selected based on multiple years of data ([War03] [NST03]). The corresponding parameter for Iridium $\sigma_{ECB-IRI}$ only produces minute variations, and was not plotted for clarity of the plot.

Third, availability performance is very sensitive to receiver noise and multipath. Values attributed to σ_{RN} and σ_M depend on user receiver technology, and may vary with satellite elevation depending on the antenna. Thus the corresponding result in Figure 10 describes the sensitivity of iGPS performance to user equipment. The nominal values selected in Table 4.1 are typical of aircraft equipment (the 60s GPS multipath time constant is conservative).

Finally, in view of the remaining results, biases (VIB and ECB) have a more significant impact than gradients (VIG and ECG) and than the troposphere parameters ZTD and Δn . Obviously, σ_{ZTD} is relatively small, and the accumulated error for the gradient-terms $ob_1 d_{IPP} VIG$, $\Delta t \cdot ECG$ and $ob_1 c_T \Delta n$ over the short smoothing interval is not nearly as large as the bias-terms ECB and $ob_1 VIB$. The influence of σ_{VIG} could be further reduced if VIG-corrections were made available (these are computed by WAAS but not currently transmitted).

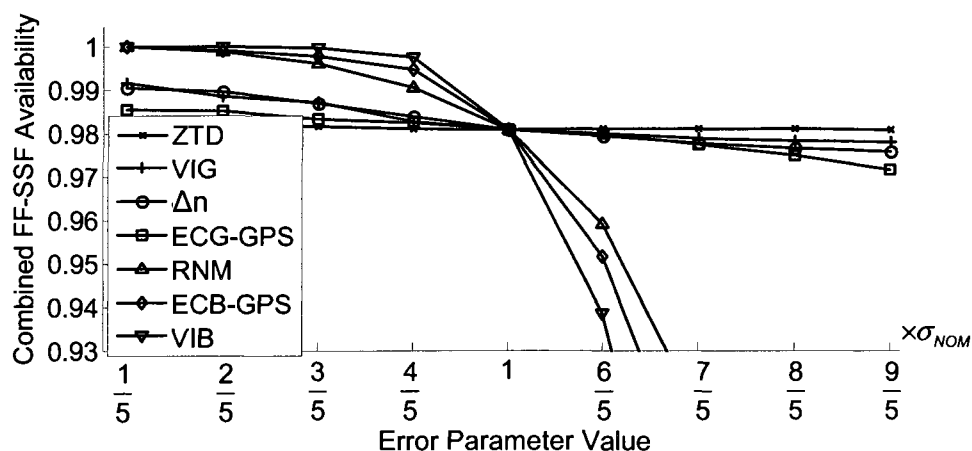


Figure 6.7. Performance Sensitivity to Measurement Error Model Parameters

6.5.2 Locations and System Configurations. Combined FF and SSF availability (for the nominal configuration) is presented for a 5deg×5deg and a 4deg×4deg latitude-longitude grid of locations respectively over CONUS and over Europe in Figure 6.8. As expected, results improve gradually at higher latitudes, as the density of Iridium satellites increases. Again in this simulation, the smoothing period T_F is 8min. If T_F is increased to 10min, 100% availability is achievable for all CONUS and Europe locations.

Since the performance is driven by Iridium SV motion, and since a large part of the variations in longitude averages out over the 3-day simulation period, availability is plotted versus latitude in Figure 6.9, for an example longitude of -80deg. Six different system configurations are considered, including the nominal case (bottom curve), which is established for a single-frequency user receiving GPS/Iridium ranging signals and WAAS-like corrections.

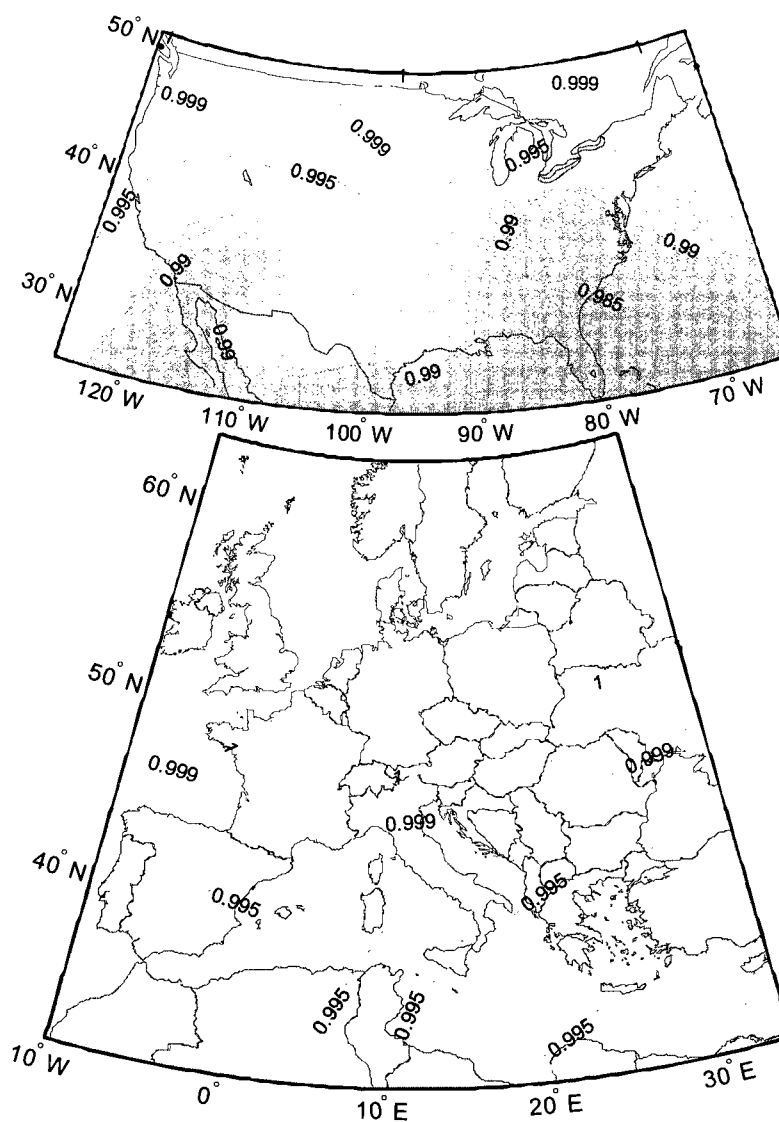


Figure 6.8. Combined FF-SSF Availability Maps for the Nominal Configuration

A substantial increase in availability, from 98.3% to 99.7% at the lowest latitude, is obtained when tracking currently-available code and carrier phase measurements from WAAS and EGNOS geostationary (GEO) satellites (coverage plots in Figure 2.7a show that two GEO SVs are visible for locations considered in Figure 6.9).

Further improvement is gained in the case where dual-frequency (DF) Iridium signals are exploited (e.g., if the Iridium Ka-band frequency is reliably tracked), or if the

Iridium space segment is extended to the hypothetical 88 spacecraft constellation described in Section 4.1.1. In both cases (DF Iridium and Iridium88), 100% availability is achieved for latitudes of 32deg and higher. Augmenting GPS with 66 Iridium and 48 GlobalStar LEO satellites provides maximum availability for all locations. In this last case, the smoothing period T_F can even be reduced from 8min to 7min.

Finally, the most promising results are obtained for future long-term evolutions. Modernization of GPS (scheduled over the next two decades) will provide civilians with DF signals, which are free of ionospheric error. There is also potential to add a reliable DF capability (other than using the Ka-band signals) to the next generation of Iridium satellites. Thus, ranging measurements only require corrections for satellite orbit and clock related errors. This considerably reduces the need for ground stations, and extends the availability of high-integrity positioning solutions to the entire planet. Results generated for the dual-frequency GPS and Iridium implementation are excellent at all latitudes.

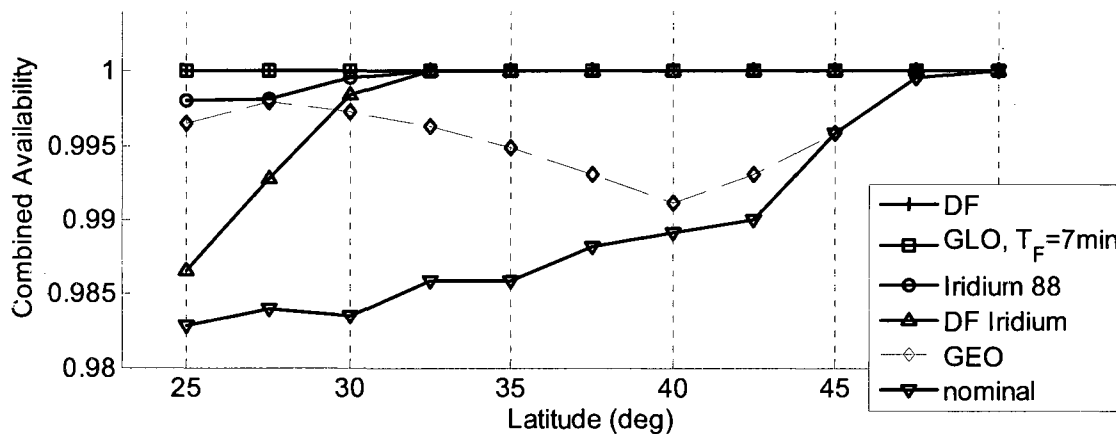


Figure 6.9. Sensitivity to System Configurations (Longitude = -80deg)

6.5.3 Near-Future iGPS Performance. To refine the sensitivity analysis, the emphasis is placed on two of the most influential parameters: the smoothing interval T_F , and the standard deviation of the residual vertical ionospheric bias σ_{VIB} . The period T_F is limited to a maximum of 10min to ensure robustness of the error models. The parameter σ_{VIB} depends on the accuracy of ionospheric corrections, which is itself determined by the ground segment. Thus, this preliminary iGPS analysis investigates the investment in ground infrastructure needed to achieve high-integrity positioning.

The system's near-future performance is evaluated for a single-frequency Iridium/GPS architecture. As a reminder, the nominal configuration assumes that users are provided with GPS ephemeris and clock data from the OCS and from WAAS as well as precise Iridium satellite orbit information. Moreover, the uncorrected instantaneous ionospheric error is such that σ_{VIB} is larger than 5m. After correction from a WAAS-like network of reference stations spread across the US, this number drops to 0.5-1.5m.

Combined FF-SSF availability results for the Miami location are given in Figure 6.10 versus σ_{VIB} and T_F . Contours of constant availability for σ_{VIB} larger than 2m are lower than 90%, regardless of T_F . This is evidence that single-frequency iGPS without corrections from a sizeable network of ground stations (e.g., WAAS-like) is not sufficient to enable applications that require high levels of accuracy and integrity, such as aircraft precision approach.

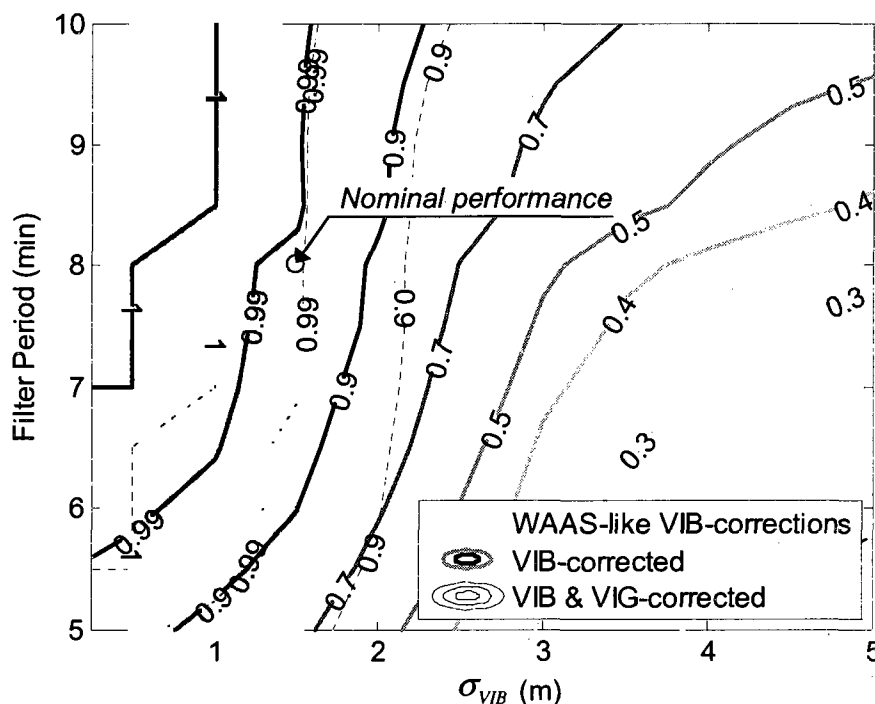


Figure 6.10. Availability Sensitivity to Filtering Period and Ionospheric Corrections

In contrast, excellent availability levels are reached in the grey-shaded area corresponding to WAAS-like ionospheric corrections. The performance sensitivity to filtering period T_F actually decreases at low σ_{VIB} values (slopes of contour lines are higher in the grey area than in the right-hand side of the plot). The 100%-availability domain ranges from σ_{VIB} of 1m and lower, and filtering periods T_F longer than 8.5min. Further enlargement of this range is immediately achievable assuming that VIG-corrections (dashed contours), which are computed but not broadcast by WAAS, are transmitted via Iridium communication channels.

Finally, the superposition of dashed and solid lines in Figure 6.10 illustrates the multidimensionality of the problem. In future steps of the navigation system design, similar analyses will be carried-out for the satellite ephemeris and clock parameters,

which have been identified in Figure 6.7 as another sensitive error source for which ground corrections are provided. In parallel, error model validation and refinement using experimental data is imperative. Ultimately, quantifying the influence on the overall end-user performance of parameters such as ionospheric and satellite-related corrections is instrumental in establishing and prioritizing recommendations on the iGPS system architecture.

CHAPTER 7

CONCLUSION

Carrier phase GPS measurements provide centimeter-level ranging precision, which can potentially enable high-accuracy and high-integrity navigation applications. Unfortunately, carrier phase-based positioning is not instantaneous, and can not be performed everywhere. This dissertation has directly addressed the issue of precision carrier phase navigation in GPS-obstructed environments using laser scanner augmentation. It has also explored the use of additional LEO Iridium satellite signals for fast cycle ambiguity resolution and for global high-integrity carrier phase navigation.

7.1 Carrier Phase GPS Augmentation Using Laser Scanners

Autonomous ground vehicles operate in environments where GPS signals are attenuated by buildings or trees. The latter must be detected for obstacle avoidance, and can in turn be used as landmarks for laser-based SLAM navigation. Tree trunks and building edges are observable by lasers when GPS is obstructed, but are likely to be out of scanner range in open-sky areas.

The complementary properties of the two sensors go beyond measurement availability. In particular, laser-based SLAM drifts with distance as earlier landmarks get out of the scanner's range and new landmarks come in sight. Also, the unbounded growth of the laser-based relative positioning error is aggravated by failed associations of newly extracted measurements with previously estimated landmark features. Absolute carrier phase GPS measurements provide a decisive means to mitigate the drift in estimation error, and to decrease the risk of miss-associations.

In urban canyons, both GPS and laser measurements are available, but individually, neither sensor is capable of generating precise vehicle trajectory estimates. In this type of environment, the superior performance of measurement-level integration over a simpler position-domain implementation is demonstrated because GPS signals that alone are too few to generate a position fix, can be effectively exploited using laser measurements.

7.2 Carrier Phase GPS Augmentation Using Low Earth Orbiting Satellites

Centimeter-level carrier phase positioning is contingent upon correct resolution of cycle ambiguities. An efficient solution for their estimation is to exploit the bias observability provided by redundant satellite motion. Unlike GPS satellites, LEO spacecraft cross large sections of the sky in short amounts of time. Therefore the combination of GPS and Iridium ranging measurements opens the possibility for rapid and accurate carrier phase positioning.

The system's promise for real-time high-integrity carrier phase positioning performance makes it a potential navigation solution for demanding precision applications such as autonomous land and air transportation. Integrity requirements for life-critical applications are particularly stringent. In this regard, the addition of Iridium satellite guarantees measurement redundancy, which enables effective mitigation of integrity threats by fault detection.

Finally, single-frequency signals implemented in most civilian applications are affected by a number of error sources including large ionospheric delays. Their impact on the positioning performance can be reduced using differential corrections from a

network of ground reference stations. Future system evolutions including dual-frequency architectures yield an even more decisive impact for Iridium-augmented GPS, as they may relax the requirements on ground infrastructure while extending the availability of high-integrity carrier-phase positioning from wide areas to the entire globe.

7.3 Summary of Achievements

The focus of this dissertation has been to investigate two augmentation systems that widen the scope of carrier phase GPS-based navigation applications. First, integration with laser scanners has resulted in increased availability of precise positioning. Second, combination with LEO Iridium satellites has opened the perspective to achieve the highest levels of civilian aircraft navigation accuracy, integrity, continuity and availability at global scale. Areas of contributions are discussed in the following subsections.

7.3.1 GPS/Laser Measurement-level Integration Algorithm and Analysis. A navigation system that integrates carrier phase GPS and laser scanner observations in the measurement range domain was developed, analyzed and tested for seamless precision positioning through GPS-obstructed environments. More precisely, a measurement-differencing extended Kalman filter was designed to perform simultaneous vehicle and landmark positioning and carrier phase estimation. Quantitative performance evaluation of the integrated navigation algorithm by covariance analysis and Monte-Carlo simulations was conducted for a benchmark AGV trajectory-tracking problem.

7.3.2 Experimental Validation of the GPS/Laser System. Experimental testing of CPDGPS-augmented SLAM procedures was carried out first in a structured environment where landmarks were easily identified and distinguished, and then in streets of Chicago where sensors were surrounded by cluttered obstacles. In the latter case in particular, the performance of the range-domain integrated system far exceeded that of a simpler position-domain implementation, in that it not only achieved sub-meter-level precision over extended GPS-obstructed areas, but also improved the robustness of laser-based SLAM.

7.3.3 iGPS Measurement Errors and Fault Modes. Realistic stochastic models were created and implemented for nominal ionosphere, troposphere, multipath and satellite orbit ephemeris and clock errors. Potential iGPS fault modes were defined and classified. Canonical models (including impulses, steps and ramps of all magnitudes and start-times) were employed to simulate single-satellite faults affecting sequences of measurements over time. In parallel, a conceptual Iridium/GPS navigation system architecture was established, including integrity requirement allocation for standalone RAIM implementations.

7.3.4 iGPS Position Estimation. A fixed-interval positioning and cycle-ambiguity resolution process was devised based on combined GPS and low-earth-orbit satellite measurements. The algorithm exploits the spatial and temporal geometric diversity provided by the joint Iridium-GPS constellation while ensuring validity for the measurement error models. Two underlying estimation mechanisms were identified as

causes of poor Iridium satellite geometry: smaller angular variations for lines of sight of low-elevation satellites, and unobservable position coordinate states due to coinciding LOS profiles over time.

7.3.5 iGPS Fault-Detection. A batch residual-based RAIM fault-detection method was developed to protect the Iridium-augmented GPS system against single-satellite faults. Performance analysis against canonical fault models helped identify undetected failure modes, whose profile was shown to match that of Iridium spacecraft range variations. In addition, worst-case performance was established by injecting failures into the system, which were specifically designed to minimize the detection test statistic (minimum-residual faults). Ground monitoring was investigated as a way to mitigate the resulting loss in navigation integrity. As an alternative, a relative RAIM algorithm was derived and showed promising results.

7.3.6 iGPS Navigation Performance. A methodology was defined to analyze and quantify the accuracy, integrity, continuity, and availability of Iridium/GPS positioning solutions under both fault-free and faulted conditions. As a result, performance evaluations demonstrate that single-frequency iGPS come close to fulfilling some of the most stringent standards currently in effect for civilian aircraft navigation. Sensitivity to navigation system parameters was assessed over the United States and Europe, for various space, ground and user segment architectures. It is shown in particular that modernization of the GPS and Iridium constellations can potentially provide worldwide high-integrity carrier-phase positioning.

7.4 Future Work

A number of recommendations for future work are given in the following subsections to enhance the performance of the GPS/laser integration, and to refine, extend and validate the Iridium-augmented GPS navigation system.

7.4.1 Laser-based Navigation and Sensor Integration. Typical environment-specific processes were selected for feature extraction and data association, which are part of the complete SLAM solution. These procedures turn out to be crucial in cluttered unstructured environments and have shown their limitations in urban canyons for the position-domain implementation. Superior performance was demonstrated with the measurement-level integration, but even better results can be obtained if miss-associations could be avoided altogether. Laser-based navigation relative to lines extracted from building walls [Sol07] is an attractive solution: lines are constantly observed in urban canyons, and lines alongside the trajectory can be tracked over much longer distances than building edges.

SLAM is typically performed in conjunction with dead-reckoning sensors. Covariance analyses and direct simulations presented in this work have alluded to the potential contribution of such sensors for estimation (they were not used in experiments to emphasize the measurement-level integration with GPS). In addition, high-update rate sensors such as INS would provide much needed robustness for data association, specifically when computing the predicted relative landmark location to be associated with incoming laser measurements. A complete tightly-integrated GPS/INS/LASER

solution will further extend the availability and continuity of high-accuracy navigation solutions.

7.4.2 Further Development and Validation of iGPS. Performance predictions presented in this dissertation are directly determined by measurement modeling assumptions. Realistic results can only be obtained if the magnitude, distribution and dynamics of the measurement errors are properly accounted for. In particular, when targeting high levels of integrity, model validation must be based on large amounts of data. Preliminary processing of experimental GPS measurements collected over a few days provide a glimpse of methods to be used in further stages of this research for estimation of ionospheric and tropospheric delays, satellite clock and orbit ephemeris errors, and multipath and receiver noise. Models for errors affecting Iridium satellite ranging signals that have never been documented require even more careful attention.

In the same perspective, failure modes should be investigated, characterized and modeled for refined evaluation of the detection algorithm (only satellite-related faults were considered in this work). A conservative assessment of the integrity monitoring capability may be provided using minimum residual faults, but it can't be established without prior determination of the failure mode's likelihood of occurrence. Truly realistic predictions of the availability of high-integrity carrier phase positioning fixes will only be achieved after the integrity threat space has been fully defined.

Updated recommendations on the iGPS system design will result from refined performance estimates after measurement error model validation. Further potential research guidelines include the use of Iridium dual-frequency measurements at ground

reference stations to improve the quality of differential ionospheric corrections. Also, Iridium's communication capability may be further exploited for enhanced GPS and Iridium satellite-related error corrections. The emergence of new GNSS implementations is motivating interest in multi-constellation positioning and fault-detection algorithms. Integration of GPS with Galileo provides increased spatial diversity (as compared to temporal diversity using Iridium satellites). Combining iGPS with Galileo will certainly generate unprecedented satellite-based navigation accuracy, integrity, continuity and availability.

Finally, iGPS system performance will have to be experimentally validated, for example for the benchmark application of aircraft precision approach. In this context, the residual-based RAIM algorithm that has been derived as a batch will have to be performed sequentially. Also, solutions other than the fixed-interval positioning algorithm should be investigated and the preferred implementation coded for real-time operation. Further analysis should be conducted to fully assess the great potential of the relative RAIM method to ensure global high-integrity positioning for iGPS.

7.5 Closing

Carrier phase GPS augmentation using laser scanners and using LEO satellites contribute to enhanced navigation performance of autonomous vehicles in the perspective of safer and less expensive transportation systems.

APPENDIX A**ADDED CONDITION FOR THE SEPARATE-STAGE CPDGPS ALGORITHM**

In this appendix, the state covariance matrices for the carrier phase positioning algorithm described in reference [Per97] are derived analytically. The resulting equations show that one important condition must be fulfilled in order to ensure proper treatment of the measurement time-correlation, when transitioning from the Kalman Filter (KF) cycle ambiguity estimation to the weighted least squares (WLS) positioning.

For the cycle ambiguity estimation, the state information matrix \mathbf{S}_k ($\mathbf{S}_k = {}^{KF}\mathbf{P}_k^{-1}$) after KF time and measurement updates can be written as [Per97]:

$$\mathbf{S}_k = \begin{bmatrix} \mathbf{0} & \mathbf{0} \\ \mathbf{0} & \mathbf{S}_N - \mathbf{S}_{uN}^T \mathbf{S}_u^{-1} \mathbf{S}_{uN} \end{bmatrix}_{k-1} + \begin{bmatrix} \mathbf{G}^T & \mathbf{G}^T \\ \mathbf{0} & \mathbf{I}_{n_s} \end{bmatrix} \begin{bmatrix} \mathbf{V}_{\Delta\rho}^{-1} & \mathbf{0} \\ \mathbf{0} & \mathbf{V}_{\Delta\phi}^{-1} \end{bmatrix} \begin{bmatrix} \mathbf{G} & \mathbf{0} \\ \mathbf{G} & \mathbf{I}_{n_s} \end{bmatrix}$$

$$\mathbf{S}_k = \begin{bmatrix} \mathbf{0} & \mathbf{0} \\ \mathbf{0} & \mathbf{S}_N - \mathbf{S}_{uN}^T \mathbf{S}_u^{-1} \mathbf{S}_{uN} \end{bmatrix}_{k-1} + \begin{bmatrix} \mathbf{G}^T (\mathbf{V}_{\Delta\rho}^{-1} + \mathbf{V}_{\Delta\phi}^{-1}) \mathbf{G} & \mathbf{G}^T \mathbf{V}_{\Delta\phi}^{-1} \\ \mathbf{V}_{\Delta\phi}^{-1} \mathbf{G} & \mathbf{V}_{\Delta\phi}^{-1} \end{bmatrix},$$

where similarly to Table 2.1 for matrix $\hat{\mathbf{P}}$, the following notation is used:

$$\mathbf{S} = \begin{bmatrix} \mathbf{S}_u & \mathbf{S}_{uN} \\ \mathbf{S}_{uN}^T & \mathbf{S}_N \end{bmatrix}.$$

The sequence of KF updates can be expressed analytically:

$$\mathbf{S}_0 = \mathbf{0}$$

$$\mathbf{S}_1 = \begin{bmatrix} \mathbf{G}_1^T (\mathbf{V}_{\Delta\rho}^{-1} + \mathbf{V}_{\Delta\phi}^{-1}) \mathbf{G}_1 & \mathbf{G}_1^T \mathbf{V}_{\Delta\phi}^{-1} \\ \mathbf{V}_{\Delta\phi}^{-1} \mathbf{G}_1 & \mathbf{V}_{\Delta\phi}^{-1} \end{bmatrix}$$

$$\mathbf{S}_2 = \begin{bmatrix} \mathbf{G}_2^T (\mathbf{V}_{\Delta\rho}^{-1} + \mathbf{V}_{\Delta\phi}^{-1}) \mathbf{G}_2 & \mathbf{G}_2^T \mathbf{V}_{\Delta\phi}^{-1} \\ \mathbf{V}_{\Delta\phi}^{-1} \mathbf{G}_2 & 2\mathbf{V}_{\Delta\phi}^{-1} - \mathbf{V}_{\Delta\phi}^{-1} \mathbf{G}_1 (\mathbf{G}_1^T (\mathbf{V}_{\Delta\rho}^{-1} + \mathbf{V}_{\Delta\phi}^{-1}) \mathbf{G}_1)^{-1} \mathbf{G}_1^T \mathbf{V}_{\Delta\phi}^{-1} \end{bmatrix},$$

$$\mathbf{S}_3 = \begin{bmatrix} \mathbf{G}_3^T (\mathbf{V}_{\Delta\rho}^{-1} + \mathbf{V}_{\Delta\phi}^{-1}) \mathbf{G}_3 & \mathbf{G}_3^T \mathbf{V}_{\Delta\phi}^{-1} \\ \mathbf{V}_{\Delta\phi}^{-1} \mathbf{G}_3 & 3\mathbf{V}_{\Delta\phi}^{-1} - \sum_{i=1}^2 \mathbf{V}_{\Delta\phi}^{-1} \mathbf{G}_i (\mathbf{G}_i^T (\mathbf{V}_{\Delta\rho}^{-1} + \mathbf{V}_{\Delta\phi}^{-1}) \mathbf{G}_i)^{-1} \mathbf{G}_i^T \mathbf{V}_{\Delta\phi}^{-1} \end{bmatrix},$$

therefore, by induction:
$$\mathbf{S}_k = \begin{bmatrix} \mathbf{G}_k^T (\mathbf{V}_{\Delta\mathbf{p}}^{-1} + \mathbf{V}_{\Delta\varphi}^{-1}) \mathbf{G}_k & \mathbf{G}_k^T \mathbf{V}_{\Delta\varphi}^{-1} \\ \mathbf{V}_{\Delta\varphi}^{-1} \mathbf{G}_k & \mathbf{S}_{\mathbf{N},k} \end{bmatrix}$$

where,
$$\mathbf{S}_{\mathbf{N},k} = k \mathbf{V}_{\Delta\varphi}^{-1} - \sum_{i=1}^{k-1} \mathbf{V}_{\Delta\varphi}^{-1} \mathbf{G}_i (\mathbf{G}_i^T (\mathbf{V}_{\Delta\mathbf{p}}^{-1} + \mathbf{V}_{\Delta\varphi}^{-1}) \mathbf{G}_i)^{-1} \mathbf{G}_i^T \mathbf{V}_{\Delta\varphi}^{-1}. \quad (\text{A.1})$$

$\mathbf{S}_{\mathbf{N},k}$ is the cycle ambiguity state information matrix. It includes the instantaneous carrier-phase measurement information $\mathbf{V}_{\Delta\varphi}^{-1}$ at all k epochs, and a term that is a function of the instantaneous position information at previous epochs ($\mathbf{S}_{\mathbf{u},i} = \mathbf{G}_i^T (\mathbf{V}_{\Delta\mathbf{p}}^{-1} + \mathbf{V}_{\Delta\varphi}^{-1}) \mathbf{G}_i$). This term contains the knowledge that code and carrier phase signals are all collected at the antenna location, and this information takes one KF update to reach the cycle ambiguity states (hence the sum over i , where i ranges from 1 to $k-1$).

The state covariance matrix ${}^{KF} \mathbf{P}_k$ (${}^{KF} \mathbf{P}_k = \mathbf{S}_k^{-1}$) can be computed using familiar matrix inversion identities, so that the block matrix corresponding to the position and receiver clock deviation states \mathbf{u} can be expressed as:

$${}^{KF} \mathbf{P}_{\mathbf{u},k} = \left(\mathbf{G}_k^T (\mathbf{V}_{\Delta\mathbf{p}}^{-1} + \mathbf{V}_{\Delta\varphi}^{-1} - \mathbf{V}_{\Delta\varphi}^{-1} \mathbf{S}_{\mathbf{N},k}^{-1} \mathbf{V}_{\Delta\varphi}^{-1}) \mathbf{G}_k \right)^{-1}. \quad (\text{A.2})$$

A WLS process is employed to estimate user position at any epoch j between times t_k and t_{k+1} :

$${}^{LS} \mathbf{P}_{\mathbf{u},j} = \left(\mathbf{G}_j^T (\mathbf{V}_{\Delta\varphi} + {}^{KF} \mathbf{P}_{\mathbf{N},k-1})^{-1} \mathbf{G}_j \right)^{-1}. \quad (\text{A.3})$$

Again, using matrix inversion identities to express ${}^{KF} \mathbf{P}_{\mathbf{N},k-1}$, equation (A.3) becomes:

$${}^{LS} \mathbf{P}_{\mathbf{u},j} = \left(\mathbf{G}_j^T \left(\mathbf{V}_{\Delta\varphi} + \left(\mathbf{S}_{\mathbf{N},k-1} - \mathbf{V}_{\Delta\varphi}^{-1} \mathbf{G}_{k-1} (\mathbf{G}_{k-1}^T (\mathbf{V}_{\Delta\mathbf{p}}^{-1} + \mathbf{V}_{\Delta\varphi}^{-1}) \mathbf{G}_{k-1})^{-1} \mathbf{G}_{k-1}^T \mathbf{V}_{\Delta\varphi}^{-1} \right)^{-1} \right)^{-1} \mathbf{G}_j \right)^{-1},$$

and using equation A.1:

$${}^{LS}\mathbf{P}_{\mathbf{u},j} = \left(\mathbf{G}_j^T \left(\mathbf{V}_{\Delta\phi} + (\mathbf{S}_{N,k} - \mathbf{V}_{\Delta\phi}^{-1})^{-1} \right) \mathbf{G}_j \right)^{-1},$$

finally, using the matrix inversion lemma:

$${}^{LS}\mathbf{P}_{\mathbf{u},j} = \left(\mathbf{G}_j^T \left(\mathbf{V}_{\Delta\phi}^{-1} - \mathbf{V}_{\Delta\phi}^{-1} \mathbf{S}_{N,k}^{-1} \mathbf{V}_{\Delta\phi}^{-1} \right) \mathbf{G}_j \right)^{-1}. \quad (\text{A.4})$$

At epoch k , the matrices ${}^{KF}\mathbf{P}_{\mathbf{u},k}$ and ${}^{LS}\mathbf{P}_{\mathbf{u},k}$ both describe the covariance of the state vector \mathbf{u}_k , computed using the KF and WLS processes respectively. They should match closely. In fact, equations A.2 and A.4 only differ by the code information matrix $\mathbf{V}_{\Delta\phi}^{-1}$, whose elements are small in comparison to $\mathbf{V}_{\Delta\phi}^{-1}$. The assumption was made in Chapter 2 that code data would not contribute much to the WLS.

Therefore, if the most recent cycle ambiguity estimate covariance ${}^{KF}\mathbf{P}_{N,k}$ was used instead of ${}^{KF}\mathbf{P}_{N,k-1}$ in equation A.3, the matrices ${}^{KF}\mathbf{P}_{\mathbf{u},k}$ and ${}^{LS}\mathbf{P}_{\mathbf{u},k}$ would not be consistent ($\mathbf{S}_{N,k+1}^{-1}$ would replace $\mathbf{S}_{N,k}^{-1}$ in equation A.4). In fact, the measurement time-correlation would not be accounted for when feeding the KF cycle-ambiguity estimates into the WLS. The use of ${}^{KF}\mathbf{P}_{N,k-1}$ imposes an initialization period between the first two KF updates, where code measurements can be used for positioning.

Figure A.1 presents vertical position standard deviations (the square root of $(\mathbf{P}_{\mathbf{u},k})_{3,3}$) for the KF (circles), and for the WLS (solid line). In this case, the multipath time constant T_M is 1min, so that KF updates are performed at regular $2T_M$ intervals of 2min. The results are compared to the vertical position covariance for a system used in Chapters 3 (dashed line), where time-correlated multipath noise is directly modeled as a first order Gauss-Markov Process (GMP) (with a time constant of T_M). The three curves

converge as the estimation of cycle ambiguities improves. The time-step delay in ${}^{KF}\mathbf{P}_N$ ensures that WLS estimates are conservative, so the corresponding curve is on top. Vertical position covariance curves for KF and GMP match at the KF updates.

Further expressions are easily obtained in the special case where four satellites are visible, meaning that \mathbf{G} is invertible. In the absence of redundant satellites, changes in geometry cannot be exploited, and the resulting position covariance is proportional to the dilution of precision $(\mathbf{G}_k^T \mathbf{G}_k)^{-1}$. Therefore, assuming diagonal measurement matrices:

$$\mathbf{V}_{\Delta p} = \sigma_{\Delta p}^2 \cdot \mathbf{I}_{n_s} \quad \text{and} \quad \mathbf{V}_{\Delta \varphi} = \sigma_{\Delta \varphi}^2 \cdot \mathbf{I}_{n_s},$$

equations A.2 and A.4 become:

$${}^{KF}\mathbf{P}_{u,k} = \sigma_{\Delta p}^2 \frac{k\sigma_{\Delta \varphi}^2 + \sigma_{\Delta p}^2}{k(\sigma_{\Delta \varphi}^2 + \sigma_{\Delta p}^2)} (\mathbf{G}_k^T \mathbf{G}_k)^{-1} \quad \text{and} \quad {}^{LS}\mathbf{P}_{u,k} = \frac{k\sigma_{\Delta \varphi}^2 + \sigma_{\Delta p}^2}{k-1} (\mathbf{G}_k^T \mathbf{G}_k)^{-1}.$$

Identical expressions are obtained in a second special case of constant SV geometry (constant matrix \mathbf{G}), even if the number of satellites in view exceeds four.

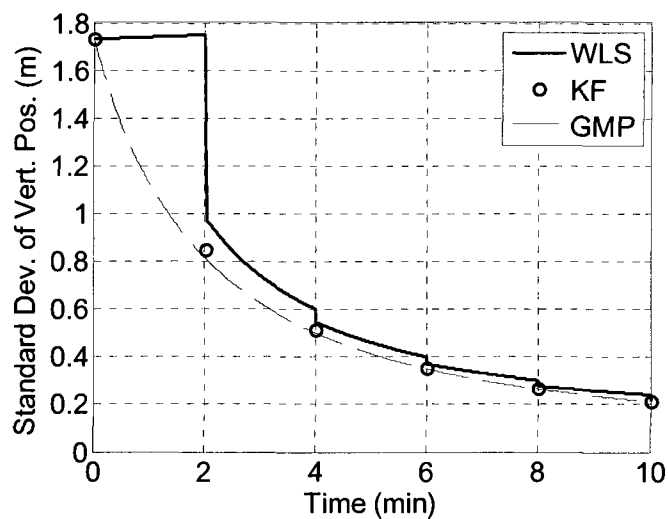


Figure A.1 Comparison Between KF updates, WLS estimates, and System Using a GMP

APPENDIX B
IMPLEMENTATION OF THE FEATURE EXTRACTION AND DATA
ASSOCIATION ALGORITHMS

This appendix describes the feature extraction and data association algorithms used in the simulations and experiments of Chapter 3.

The feature extraction process aims at identifying the most repeatedly recognizable, viewpoint-invariant features surrounding the laser, such as centers of tree trunks or edges of buildings. At this stage of the algorithm's development, separate procedures are used for the forest and urban canyon scenarios. Both situations have in common that noise and discontinuous objects such as fences or vegetation prevent the laser scan from describing clean contours for the landmarks of interest. In addition, laser beams reflected at low angles of incidence have very inconsistent returns. A careful calibration of the laser and a straightforward noise-rejection filter attenuate these problems while preserving the sharpness of the contours. The latter filter also gets rid of mixed-pixel interferences, which occur when a single beam spans on two surfaces at different depths [Ye02]. The data is then segmented based on a predefined threshold (selected using experimental data) between consecutive measurements.

In a structured environment where vertical cylinders are placed along the vehicle trajectory, segments that are closer than the range limit are considered potential landmarks, provided that the segment is large enough. The minimum number of measurements per segment is a function of the target object's minimum size, the angular resolution, and the laser range. Landmark features are then derived so that the extracted ranging measurement fed into the estimator is the sum of the smallest distance to the cylinder and its estimated radius.

For the urban canyon scenario, segments containing less than a predefined number of measurements (calibrated for that specific environment) are considered as noise and such segments are modified into continuous lines linking previous and following segments. Edges of buildings that point toward the laser scanner are easy to identify because they correspond to local minima in the ranging measurements. We choose not to consider edges that point away from the scanner; they coincide with discontinuities in the scanned ranging measurements and can therefore easily be confused with noise. The price to pay for this choice is that features targeted by the front and back lasers are not the same. Next, the laser scan is smoothed using an averaging filter so that only the dominating local minima remain. The size of the averaging kernel is tuned depending on the environment, so that the desired average number of landmarks is extracted. Finally, once the angular values for the dominating local minima are found, the corresponding ranging measurements in the noise-free data are extracted.

The data association procedure aims at matching current extracted measurements with landmarks that are being estimated in the EKF. For each measurement j and for each previously estimated landmark i , we compute the Mahalanobis distance (or normalized innovation square) [Bar88]:

$${}^{i,j}\gamma = {}^{i,j}\tilde{\mathbf{z}}^T ({}^i\bar{\mathbf{Z}})^{-1} {}^{i,j}\tilde{\mathbf{z}}$$

where

$${}^{i,j}\tilde{\mathbf{z}} = {}^j\mathbf{z} - {}^i\bar{\mathbf{z}}.$$

${}^i\bar{\mathbf{z}} = \mathbf{h}_{\text{LAS}}(\bar{\mathbf{x}})$ is the best projected estimate of the laser measurement vector obtained from the non-linear equations 3.2 and 3.3. The matrix ${}^i\bar{\mathbf{Z}}$ is made of the elements of $\bar{\mathbf{Z}}$

corresponding to landmark i , with:

$$\bar{\mathbf{Z}} = \mathbf{H}\bar{\mathbf{P}}\mathbf{H}^T + \mathbf{V}.$$

The first stage of the association is a validation stage. The Mahalanobis distance ${}^{i,j}\gamma$ follows a chi-square probability distribution, with two degrees of freedom. Therefore, the association is validated only if ${}^{i,j}\gamma$ is lower than a predefined threshold corresponding to a desired confidence level.

If a measurement is validated for more than one landmark, it is associated with its nearest neighbor in terms of Mahalanobis distance. If multiple measurements are validated for a single landmark, we make the conservative choice of rejecting all of these observations. Measurements that have not been validated are interpreted as belonging to new landmarks, which are given a new identification number.

It is worth noticing from the expression of ${}^{i,j}\gamma$ that the better the estimate of a landmark, the more robust its association with incoming measurements. Indeed, the equivalent validation threshold on the physical distance between estimated landmark and current measurement (i.e., on $\sqrt{({}^{i,j}\tilde{\mathbf{z}})^T ({}^{i,j}\tilde{\mathbf{z}})}$) tightens as the landmark state estimate improves.

APPENDIX C
LINEARIZED LASER MEASUREMENT EQUATIONS

Measurement equations 3.2 and 3.3 must be linearized for covariance estimation.

Consider a-priori guesses of user and landmark locations, respectively noted $\bar{\mathbf{x}}_{EN}$ and ${}^i\bar{\mathbf{p}}$ (e.g., initially based on prior measurements, then iteratively updated), such that:

$$\bar{\mathbf{x}}_{EN} = [\bar{x}_E \quad \bar{x}_N]^T, \quad {}^i\bar{\mathbf{p}} = [{}^i\bar{p}_E \quad {}^i\bar{p}_N]^T$$

and

$${}^i\bar{d} = \sqrt{({}^i\bar{p}_E - \bar{x}_E)^2 + ({}^i\bar{p}_N - \bar{x}_N)^2} = \|{}^i\bar{\mathbf{p}} - \bar{\mathbf{x}}_{EN}\|.$$

The laser ranging measurement ${}^i d$ in equation 3.2 can be approximated about the predicted estimates using a first order Taylor series expansion:

$${}^i d \approx {}^i\bar{d} + \frac{\partial {}^i d}{\partial x_E} \delta x_E + \frac{\partial {}^i d}{\partial x_N} \delta x_N + \frac{\partial {}^i d}{\partial {}^i p_E} \delta {}^i p_E + \frac{\partial {}^i d}{\partial {}^i p_N} \delta {}^i p_N + v_d, \quad (\text{C.1})$$

where position coordinate deviations δx are defined as:

$$\delta x = (x - \bar{x}). \quad (\text{C.2})$$

Partial derivatives are expressed in terms of the known predicted estimates, so that:

$$\frac{\partial {}^i d}{\partial x_E} = -\frac{{}^i\bar{p}_E - \bar{x}_E}{\|{}^i\bar{\mathbf{p}} - \bar{\mathbf{x}}_{EN}\|}, \quad \frac{\partial {}^i d}{\partial x_N} = -\frac{{}^i\bar{p}_N - \bar{x}_N}{\|{}^i\bar{\mathbf{p}} - \bar{\mathbf{x}}_{EN}\|}, \quad (\text{C.3})$$

and

$$\frac{\partial {}^i d}{\partial {}^i p_E} = \frac{{}^i\bar{p}_E - \bar{x}_E}{\|{}^i\bar{\mathbf{p}} - \bar{\mathbf{x}}_{EN}\|} = -\frac{\partial {}^i d}{\partial x_E}, \quad \frac{\partial {}^i d}{\partial {}^i p_N} = \frac{{}^i\bar{p}_N - \bar{x}_N}{\|{}^i\bar{\mathbf{p}} - \bar{\mathbf{x}}_{EN}\|} = -\frac{\partial {}^i d}{\partial x_N}. \quad (\text{C.4})$$

A fast converging Newton-Raphson method [Mis01] is employed to reduce deviations δx in equation C.2 by iteratively updating prediction estimates \bar{x} until the model fits the measurement with the desired level of accuracy.

In addition, using equations C.1 to C.4, known terms can be isolated in order to define a linearized ranging measurement ${}^i d_L$:

$${}^i d_L \equiv {}^i d - {}^i\bar{d} + \frac{{}^i\bar{p}_E - \bar{x}_E}{\|{}^i\bar{\mathbf{p}} - \bar{\mathbf{x}}_{EN}\|} ({}^i\bar{p}_E - \bar{x}_E) + \frac{{}^i\bar{p}_N - \bar{x}_N}{\|{}^i\bar{\mathbf{p}} - \bar{\mathbf{x}}_{EN}\|} ({}^i\bar{p}_N - \bar{x}_N).$$

Equation C.2 becomes,

$${}^i d_L = \frac{{}^i \bar{p}_E - \bar{x}_E}{\|{}^i \bar{\mathbf{p}} - \bar{\mathbf{x}}_{EN}\|} ({}^i p_E - x_E) + \frac{{}^i \bar{p}_N - \bar{x}_N}{\|{}^i \bar{\mathbf{p}} - \bar{\mathbf{x}}_{EN}\|} ({}^i p_N - x_N) + v_d.$$

The angular measurement equation 3.3 is linearized in an identical manner. The linearized angle ${}^i \theta_L$ is defined as:

$${}^i \theta_L \equiv {}^i \theta_T - {}^i \bar{\theta} - \frac{{}^i \bar{p}_N - \bar{x}_N}{\|{}^i \bar{\mathbf{p}} - \bar{\mathbf{x}}_{EN}\|^2} ({}^i \bar{p}_E - \bar{x}_E) + \frac{{}^i \bar{p}_E - \bar{x}_E}{\|{}^i \bar{\mathbf{p}} - \bar{\mathbf{x}}_{EN}\|^2} ({}^i \bar{p}_N - \bar{x}_N) - \bar{\psi}$$

and is equal to,

$${}^i \theta_L = -\frac{{}^i \bar{p}_N - \bar{x}_N}{\|{}^i \bar{\mathbf{p}} - \bar{\mathbf{x}}_{EN}\|^2} ({}^i p_E - x_E) + \frac{{}^i \bar{p}_E - \bar{x}_E}{\|{}^i \bar{\mathbf{p}} - \bar{\mathbf{x}}_{EN}\|^2} ({}^i p_N - x_N) - \psi + v_\theta.$$

Observations for all landmarks are stacked together in vectors, so that the linearized laser measurement equation 3.4 is:

$$\begin{bmatrix} \mathbf{d}_L \\ \boldsymbol{\theta}_L \end{bmatrix} = \begin{bmatrix} \mathbf{F}_{d,x} & \mathbf{0} & \mathbf{F}_{d,p} \\ \mathbf{F}_{\theta,x} & -\mathbf{1}_{n_L} & \mathbf{F}_{\theta,p} \end{bmatrix} \begin{bmatrix} \mathbf{x}_{EN} \\ \psi \\ \mathbf{p} \end{bmatrix} + \begin{bmatrix} \mathbf{v}_d \\ \mathbf{v}_\theta \end{bmatrix}.$$

The matrices $\mathbf{F}_{d,x}$ (of dimensions $n_L \times 2$) and $\mathbf{F}_{d,p}$ ($n_L \times 2n_L$) are expressed as:

$$\mathbf{F}_{d,x} = \begin{bmatrix} -\frac{{}^1 \bar{p}_E - \bar{x}_E}{\|{}^1 \bar{\mathbf{p}} - \bar{\mathbf{x}}_{EN}\|} & \dots & -\frac{{}^{n_L} \bar{p}_E - \bar{x}_E}{\|{}^{n_L} \bar{\mathbf{p}} - \bar{\mathbf{x}}_{EN}\|} \\ \frac{{}^1 \bar{p}_N - \bar{x}_N}{\|{}^1 \bar{\mathbf{p}} - \bar{\mathbf{x}}_{EN}\|} & \dots & \frac{{}^{n_L} \bar{p}_N - \bar{x}_N}{\|{}^{n_L} \bar{\mathbf{p}} - \bar{\mathbf{x}}_{EN}\|} \end{bmatrix}^T$$

$$\text{and } \mathbf{F}_{d,p} = \begin{bmatrix} \frac{{}^1\bar{p}_E - \bar{x}_E}{\|{}^1\bar{\mathbf{p}} - \bar{\mathbf{x}}_{EN}\|} & \frac{{}^1\bar{p}_N - \bar{x}_N}{\|{}^1\bar{\mathbf{p}} - \bar{\mathbf{x}}_{EN}\|} & \mathbf{0} & \mathbf{0} & \mathbf{0} & \mathbf{0} \\ \mathbf{0} & \mathbf{0} & \ddots & \ddots & \mathbf{0} & \mathbf{0} \\ \mathbf{0} & \mathbf{0} & \mathbf{0} & \mathbf{0} & \frac{{}^{n_L}\bar{p}_E - \bar{x}_E}{\|{}^{n_L}\bar{\mathbf{p}} - \bar{\mathbf{x}}_{EN}\|} & \frac{{}^{n_L}\bar{p}_N - \bar{x}_N}{\|{}^{n_L}\bar{\mathbf{p}} - \bar{\mathbf{x}}_{EN}\|} \end{bmatrix}.$$

$\mathbf{F}_{\theta,x}$ and $\mathbf{F}_{\theta,p}$ are constructed according to the same pattern:

$$\mathbf{F}_{\theta,x} = \begin{bmatrix} \frac{{}^1\bar{p}_N - \bar{x}_N}{\|{}^1\bar{\mathbf{p}} - \bar{\mathbf{x}}_{EN}\|^2} & \dots & \frac{{}^{n_L}\bar{p}_N - \bar{x}_N}{\|{}^{n_L}\bar{\mathbf{p}} - \bar{\mathbf{x}}_{EN}\|^2} \\ \frac{{}^1\bar{p}_E - \bar{x}_E}{\|{}^1\bar{\mathbf{p}} - \bar{\mathbf{x}}_{EN}\|^2} & \dots & \frac{{}^{n_L}\bar{p}_E - \bar{x}_E}{\|{}^{n_L}\bar{\mathbf{p}} - \bar{\mathbf{x}}_{EN}\|^2} \end{bmatrix}^T$$

$$\text{and } \mathbf{F}_{\theta,p} = \begin{bmatrix} -\frac{{}^1\bar{p}_N - \bar{x}_N}{\|{}^1\bar{\mathbf{p}} - \bar{\mathbf{x}}_{EN}\|^2} & \frac{{}^1\bar{p}_E - \bar{x}_E}{\|{}^1\bar{\mathbf{p}} - \bar{\mathbf{x}}_{EN}\|^2} & \mathbf{0} & \mathbf{0} & \mathbf{0} & \mathbf{0} \\ \mathbf{0} & \mathbf{0} & \ddots & \ddots & \mathbf{0} & \mathbf{0} \\ \mathbf{0} & \mathbf{0} & \mathbf{0} & \mathbf{0} & -\frac{{}^{n_L}\bar{p}_N - \bar{x}_N}{\|{}^{n_L}\bar{\mathbf{p}} - \bar{\mathbf{x}}_{EN}\|^2} & \frac{{}^{n_L}\bar{p}_E - \bar{x}_E}{\|{}^{n_L}\bar{\mathbf{p}} - \bar{\mathbf{x}}_{EN}\|^2} \end{bmatrix}.$$

APPENDIX D
ADDITIONAL STEPS IN THE DERIVATION OF THE MEASUREMENT
DIFFERENCING FILTER

As a result of the pseudo-measurement equation 3.6, the pseudo-measurement noise ${}^r \mathbf{v}_k$ and the process noise \mathbf{w}_k are correlated. This correlation can be eliminated using a pseudo-process equation:

$$\begin{aligned} \mathbf{x}_{k+1} &= \Phi \mathbf{x}_k + \mathbf{w}_k + \mathbf{D}_k \left({}^r \mathbf{z}_k - {}^r \mathbf{H}_k \mathbf{x}_k - {}^r \mathbf{v}_k \right) \\ &= \left(\Phi - \mathbf{D}_k {}^r \mathbf{H}_k \right) \mathbf{x}_k + \mathbf{D}_k {}^r \mathbf{z}_k + \mathbf{w}_k - \mathbf{D}_k {}^r \mathbf{v}_k \\ &= {}^r \Phi \mathbf{x}_k + \mathbf{D}_k {}^r \mathbf{z}_k + {}^r \mathbf{w}_k \end{aligned} \quad (\text{D.1})$$

where \mathbf{D}_k is an arbitrary $n \times m$ matrix, n being the number of states, and m the number of measurements. For state propagation between epochs k and $k+1$, ${}^r \mathbf{z}_k$ is considered a deterministic input. Equation D.1 is therefore written in the traditional form of a process equation 3.11. The pseudo-process matrix and noise vector are defined as follows:

$${}^r \Phi = \Phi - \mathbf{D}_k {}^r \mathbf{H}_k \quad \text{and} \quad {}^r \mathbf{w}_k = \mathbf{w}_k - \mathbf{D}_k {}^r \mathbf{v}_k.$$

In order for ${}^r \mathbf{v}_k$ and ${}^r \mathbf{w}_k$ to be uncorrelated, \mathbf{D}_k is chosen such that:

$$\mathbf{D}_k = \mathbf{W} \mathbf{H}_k^T {}^r \mathbf{V}^{-1}$$

where \mathbf{W} and ${}^r \mathbf{V}$ are the covariance matrices corresponding respectively to \mathbf{w} and ${}^r \mathbf{v}$. Bryson provides a detailed and elegant derivation of this result in [Bry02].

Equations 3.6 and D.1 constitute a state-space representation, whose state vector can be estimated using a KF (e.g. [Gel74]). Nevertheless, one crucial difference with traditional implementations is the interpretation of the filter's solution with respect either to the pseudo-measurement ${}^r \mathbf{z}$, or to the actual measurement \mathbf{z} , in which we are interested here.

If we use the notation ${}^r \hat{\mathbf{x}}_{k|k}$ to designate the best estimate of \mathbf{x}_k knowing ${}^r \mathbf{z}_k$, and $\hat{\mathbf{x}}_{k|k}$ for the best estimate of \mathbf{x}_k knowing \mathbf{z}_k , then according to equation 3.6, we can write

the equivalences:

$${}^r \hat{\mathbf{x}}_{k|k} \equiv \hat{\mathbf{x}}_{k|k+1} \quad \text{and} \quad {}^r \hat{\mathbf{x}}_{k+1|k} \equiv \hat{\mathbf{x}}_{k+1|k+1}.$$

Refer to [Bry68] for more details. As a result, the KF estimation equations are:

$$\hat{\mathbf{x}}_{k-1|k} = \hat{\mathbf{x}}_{k-1|k-1} + \mathbf{K}_k \left({}^r \mathbf{z}_k - {}^r \mathbf{H}_k \hat{\mathbf{x}}_{k-1|k-1} \right)$$

$$\hat{\mathbf{x}}_{k|k} = {}^r \Phi \hat{\mathbf{x}}_{k-1|k} + \mathbf{D}_k {}^r \mathbf{z}_k.$$

The Kalman filter gain $\mathbf{K}_k = \hat{\mathbf{P}}_k {}^r \mathbf{H}_k^T \left({}^r \mathbf{H}_k \hat{\mathbf{P}}_k {}^r \mathbf{H}_k^T + {}^r \mathbf{V} \right)^{-1}$ is computed using the state estimate covariance $\hat{\mathbf{P}}_{k|k}$. The actual prediction $\hat{\mathbf{x}}_{k+1|k}$ is obtained from

$$\hat{\mathbf{x}}_{k+1|k} = \Phi \hat{\mathbf{x}}_{k|k}, \quad \text{with covariance} \quad \hat{\mathbf{P}}_{k+1|k} = \Phi \hat{\mathbf{P}}_{k|k} \Phi^T + \mathbf{W}.$$

APPENDIX E
REDUCED-ORDER WEIGHTED LEAST SQUARES RESIDUAL EQUATION WITH
PRIOR KNOWLEDGE

The pseudo-measurement equation 5.3 can be incorporated to the batch observation equation 5.2 by augmentation:

$$\mathbf{z} = \begin{bmatrix} \mathbf{H}_B \\ \mathbf{H}_P \end{bmatrix} \mathbf{x} + \begin{bmatrix} \mathbf{v}_B \\ \mathbf{v}_P \end{bmatrix}, \quad (\text{E.1})$$

in order to get an equation of the same form as equation 5.4:

$$\mathbf{z} = \mathbf{H}\mathbf{x} + \mathbf{v}.$$

\mathbf{H}_P is subdivided to distinguish states with no prior knowledge (\mathbf{u} and \mathbf{N}) from the error states whose initial uncertainty can be bounded: $\mathbf{H}_P = [\mathbf{0}_{n_E \times (4n_K + n_S)} \quad \mathbf{I}_{n_E}]$. The same subdivision is performed on \mathbf{H}_B , so that $\mathbf{H}_B = [\mathbf{H}_{uN} \quad \mathbf{H}_E]$. The weighted least squares state covariance matrix is:

$$\mathbf{P}_x = (\mathbf{H}^T \mathbf{V}^{-1} \mathbf{H})^{-1}, \quad \text{where } \mathbf{V} = \begin{bmatrix} \mathbf{V}_B & \mathbf{0} \\ \mathbf{0} & \mathbf{V}_P \end{bmatrix}$$

$$\mathbf{P}_x = \begin{bmatrix} \mathbf{H}_{uN}^T \mathbf{V}_B^{-1} \mathbf{H}_{uN} & \mathbf{H}_{uN}^T \mathbf{V}_B^{-1} \mathbf{H}_E \\ \mathbf{H}_E^T \mathbf{V}_B^{-1} \mathbf{H}_{uN} & \mathbf{H}_E^T \mathbf{V}_B^{-1} \mathbf{H}_E + \mathbf{V}_P^{-1} \end{bmatrix}^{-1}$$

which can be written as
$$\mathbf{P}_x = \left(\begin{bmatrix} \mathbf{0} & \mathbf{0} \\ \mathbf{0} & \mathbf{V}_P^{-1} \end{bmatrix} + \mathbf{H}_B^T \mathbf{V}_B^{-1} \mathbf{H}_B \right)^{-1}. \quad (\text{E.2})$$

The last expression is actually a KF measurement update covariance equation, in which the first term of the addition is the information matrix at mission initialization, the inverse of which is referred to as the a-priori state estimate covariance matrix in [Cra04].

The following notation is then defined:

$$\mathbf{P}_x = \begin{bmatrix} \mathbf{P}_{uN} & \mathbf{P}_{uNE} \\ \mathbf{P}_{uNE}^T & \mathbf{P}_E \end{bmatrix}.$$

The augmented residual ($\mathbf{r} = [\mathbf{r}_B^T \quad \mathbf{r}_p^T]^T$) subject to a failure \mathbf{f} (with $\boldsymbol{\varepsilon} = \mathbf{f} + \mathbf{v}$) is:

$$\begin{bmatrix} \mathbf{r}_B \\ \mathbf{r}_p \end{bmatrix} = (\mathbf{I} - \mathbf{HS}) \begin{bmatrix} \boldsymbol{\varepsilon} \\ \mathbf{0} \end{bmatrix}.$$

With the above notations, \mathbf{HS} is subdivided into four blocks. Only the upper left-hand block is needed, since the residual \mathbf{r}_p of the conceptual pseudo-measurement is of no interest. Hence, based on equation 5.5 describing the matrix \mathbf{S} pseudo-inverse of \mathbf{H} weighted by \mathbf{V} , computation of \mathbf{r}_B results in:

$$\mathbf{r}_B = \boldsymbol{\varepsilon} - \left(\mathbf{H}_{uN} \mathbf{P}_{uN} \mathbf{H}_{uN}^T + \mathbf{H}_E \mathbf{P}_{uNE} \mathbf{H}_{uN}^T + \mathbf{H}_{uN} \mathbf{P}_{uNE} \mathbf{H}_E^T + \mathbf{H}_E \mathbf{P}_E \mathbf{H}_E^T \right) \mathbf{V}_B^{-1} \boldsymbol{\varepsilon}$$

which ultimately reduces to: $\mathbf{r}_B = \left(\mathbf{I} - \mathbf{H}_B \mathbf{P}_x \mathbf{H}_B^T \mathbf{V}_B^{-1} \right) \boldsymbol{\varepsilon}$. (E.3)

If equations E.2 and E.3 are implemented rather than the augmented system E.1, the dimension of the residual vector \mathbf{r}_B decreases by an average of 50 elements (for the nominal configuration) with respect to \mathbf{r} , and brings about substantial computational gain when determining $\|\mathbf{r}\|_w$.

APPENDIX F**EQUATION OF CHANGE IN CARRIER PHASE MEASUREMENT FOR RRAIM**

The expression of the RRAIM carrier phase measurement for satellite s at time t_j is identical to equation 4.3 with a new set of error parameters. In this instance, the terms are referenced to t_0 instead of the initial filtering epoch t_{k_0} . The reference time t_0 is an epoch at which the position and receiver clock deviation state vector \mathbf{u}_0 , and their covariance $\mathbf{P}_{\mathbf{u},0}$ have been estimated. The carrier phase measurement equations at t_0 and t_j do not need to be detailed, as only the relative change is of interest.

The subscript Δ in the next equations indicates a difference between parameters at times t_j and t_0 . The time interval T_{RRAIM} is defined in Section 5.3.2 as: $T_{RRAIM} = t_j - t_0$. The time-differential carrier phase measurement ${}^s\phi_{L,\Delta}$ is expressed as:

$${}^s\phi_{L,\Delta} = {}^s\phi_{L,j} - {}^s\phi_{L,0}$$

$${}^s\phi_{L,\Delta} = {}^s\mathbf{g}_j^T \mathbf{u}_j - {}^s\mathbf{g}_0^T \mathbf{u}_0 + {}^s\mathcal{E}_{\phi,\Delta},$$

where

$${}^s\mathcal{E}_{\phi,\Delta} = T_{RRAIM} \cdot {}^sECG + ({}^sob_{T,j} - {}^sob_{T,0}) \cdot ZTD + {}^sob_{T,j} c_{T,j} \cdot \Delta n \\ - ({}^sob_{I,j} - {}^sob_{I,0}) \cdot {}^sVIB - {}^sob_{I,j} {}^sd_{IPP,j} \cdot {}^sVIG + {}^s\mathcal{E}_{M-\phi,\Delta} + {}^s\mathbf{v}_{RN-\phi,\Delta}$$

Constant terms sN and sECB have cancelled out.

Finally, measurements for all n_Δ satellites (visible at t_0 and t_j) are stacked together in a vector $\boldsymbol{\phi}_\Delta$, so that:

$$\boldsymbol{\phi}_\Delta = [\dots \quad {}^s\phi_\Delta \quad \dots]^T, \quad \text{and} \quad \mathbf{v}_{\boldsymbol{\phi},\Delta} = [\dots \quad {}^s\mathcal{E}_{\phi,\Delta} \quad \dots]^T.$$

The covariance $\mathbf{V}_{\boldsymbol{\phi},\Delta}$ of the measurement noise $\mathbf{v}_{\boldsymbol{\phi},\Delta}$ is computed as:

$$\mathbf{V}_{\boldsymbol{\phi},\Delta} = \mathbf{I}_{n_\Delta} \sigma_{\phi,\Delta}^2$$

where,

$$\begin{aligned} \sigma_{\phi,\Delta}^2 = & (T_{RRAIM} \cdot \sigma_{ECG})^2 + ({}^s ob_{T,\Delta} \cdot \sigma_{ZTD})^2 + ({}^s ob_{T,k} \tilde{c}_{T,k} \cdot \sigma_{\Delta n})^2 \\ & + ({}^s ob_{I,\Delta} \cdot \sigma_{VIB})^2 + ({}^s ob_{I,k} {}^s d_{IPP,k} \cdot \sigma_{VIG})^2 + 2\sigma_{RN-\phi}^2 \cdot \\ & + 2(1 - e^{-2T_{RRAIM}/T_M}) \sigma_{M-\phi}^2 \end{aligned}$$

APPENDIX G**CURRENT-TIME STATE ESTIMATE ERROR COVARIANCE FOR RRAIM**

The covariance of the state estimate error $\delta\mathbf{u}_j$ can be expressed using the expected value operator $E\{\}$ (biases \mathbf{b}_0 and \mathbf{f}_Δ cancel out and are implicitly removed):

$$\begin{aligned}\mathbf{P}_{u,j} &= E\{\delta\mathbf{u}_j\delta\mathbf{u}_j^T\} \\ \mathbf{P}_{u,j} &= E\{(\delta\mathbf{u}_0 + \delta\mathbf{u}_\Delta)(\delta\mathbf{u}_0 + \delta\mathbf{u}_\Delta)^T\} \\ \mathbf{P}_{u,j} &= E\{\delta\mathbf{u}_0\delta\mathbf{u}_0^T + \delta\mathbf{u}_0\delta\mathbf{u}_\Delta^T + \delta\mathbf{u}_\Delta\delta\mathbf{u}_0^T + \delta\mathbf{u}_\Delta\delta\mathbf{u}_\Delta^T\}.\end{aligned}\quad (\text{G.1})$$

Equation G.1 is computed term by term:

- $$E\{\delta\mathbf{u}_0\delta\mathbf{u}_0^T\} = \mathbf{P}_{u,0}$$
- $$E\{\delta\mathbf{u}_0\delta\mathbf{u}_\Delta^T\} = E\left\{\delta\mathbf{u}_0\left(\mathbf{S}_\Delta\left(\mathbf{v}_{\varphi,\Delta} - \mathbf{G}_\Delta\delta\mathbf{u}_0\right)\right)^T\right\}$$

The term $\delta\mathbf{u}_0$ is derived from the batch measurement equation 5.4.

Computation of the correlation matrix $E\{\delta\mathbf{u}_0\mathbf{v}_{\varphi,\Delta}^T\}$ (which is non-zero due to carrier phase multipath) is challenging but can be avoided by imposing that the T_{RRAIM} period be larger than $2T_M$, in which case: $E\{\delta\mathbf{u}_0\mathbf{v}_{\varphi,\Delta}^T\} = \mathbf{0}$.

$$E\{\delta\mathbf{u}_0\delta\mathbf{u}_\Delta^T\} = -E\{\delta\mathbf{u}_0\delta\mathbf{u}_0^T\}\mathbf{G}_\Delta^T\mathbf{S}_\Delta^T$$

- Similarly:
$$E\{\delta\mathbf{u}_\Delta\delta\mathbf{u}_0^T\} = -\mathbf{S}_\Delta\mathbf{G}_\Delta E\{\delta\mathbf{u}_0\delta\mathbf{u}_0^T\}$$
- $$E\{\delta\mathbf{u}_\Delta\delta\mathbf{u}_\Delta^T\} = E\left\{\left(\mathbf{S}_\Delta\left(\mathbf{v}_{\varphi,\Delta} - \mathbf{G}_\Delta\delta\mathbf{u}_0\right)\right)\left(\mathbf{S}_\Delta\left(\mathbf{v}_{\varphi,\Delta} - \mathbf{G}_\Delta\delta\mathbf{u}_0\right)\right)^T\right\}$$

$$E\{\delta\mathbf{u}_\Delta\delta\mathbf{u}_\Delta^T\} = \mathbf{S}_\Delta E\left\{\mathbf{v}_{\varphi,\Delta}\mathbf{v}_{\varphi,\Delta}^T - \mathbf{v}_{\varphi,\Delta}\delta\mathbf{u}_0^T\mathbf{G}_\Delta^T - \mathbf{G}_\Delta\delta\mathbf{u}_0\mathbf{v}_{\varphi,\Delta}^T + \mathbf{G}_\Delta\delta\mathbf{u}_0\delta\mathbf{u}_0^T\mathbf{G}_\Delta^T\right\}\mathbf{S}_\Delta^T$$

which again, assuming that T_{RRAIM} is larger than $2T_M$, yields:

$$E\{\delta\mathbf{u}_\Delta\delta\mathbf{u}_\Delta^T\} = \mathbf{S}_\Delta E\left\{\mathbf{v}_{\varphi,\Delta}\mathbf{v}_{\varphi,\Delta}^T\right\}\mathbf{S}_\Delta^T + \mathbf{S}_\Delta\mathbf{G}_\Delta\mathbf{P}_{u,0}\mathbf{G}_\Delta^T\mathbf{S}_\Delta^T.$$

Finally, equation G.1 becomes:

$$\mathbf{P}_{\mathbf{u},j} = \mathbf{S}_{\Delta} \mathbf{V}_{\varphi,\Delta} \mathbf{S}_{\Delta}^T + (\mathbf{I}_4 - \mathbf{S}_{\Delta} \mathbf{G}_{\Delta}) \mathbf{P}_{\mathbf{u},0} (\mathbf{I}_4 - \mathbf{S}_{\Delta} \mathbf{G}_{\Delta})^T$$

where again, as expressed in equation 5.18,

$$\mathbf{S}_{\Delta} = (\mathbf{G}_j^T \mathbf{V}_{\Delta}^{-1} \mathbf{G}_j)^{-1} \mathbf{G}_j^T \mathbf{V}_{\Delta}^{-1}, \quad \text{with} \quad \mathbf{V}_{\Delta} = \mathbf{V}_{\varphi,\Delta} + \mathbf{G}_{\Delta} \mathbf{P}_{\mathbf{u},0} \mathbf{G}_{\Delta}^T.$$

BIBLIOGRAPHY

- [Ash88] Ashjaee, J. "On Precision of GPS C/A Code." *IEEE Aerospace Electronic Systems Magazine*. (1988).
- [Bae06] Bae, T. S. "Near-Real-Time Precise Orbit Determination of Low Earth Orbit Satellites Using an Optimal GPS Triple-Differencing Technique." *PhD Dissertation*. Columbus, OH: Ohio State University. (2006).
- [Bak99] Bakhache, B. "A Sequential RAIM Based on the Civil Aviation Requirements." *Proceedings of the 12th International Technical Meeting of the Institute of Navigation*. Nashville, TN. (1999): 1201-1210.
- [Bar88] Bar-Shalom, Y., and T. E. Fortmann. "Tracking and Data Association." *Mathematics in Science and Engineering*. San Diego, CA: Academic Press. 179 (1988).
- [Bat71] Bate, R., D. Mueller, and J. White. *Fundamentals of Astrodynamics*. New York, NY: Dover Publications, Inc. (1971).
- [Bay05] Bayoud, F. "Vision-Aided Inertial Navigation Using a Geomatics Approach." *Proceedings of the Institute of Navigation GNSS Conference*. Long Beach, CA. (2005).
- [Bel99] Bell, T. "Precision Robotic Control of Agricultural Vehicles on Realistic Farm Trajectories." *PhD Dissertation*. Stanford, CA: Stanford University. (1999).
- [Bis01] Bisnath, S., and R. Langley. "Precise Orbit Determination of Low Earth Orbiters with GPS Point Positioning." *Proceedings of the National Technical Meeting of the Institute of Navigation*. Long Beach, CA. (2001): 725-733.
- [Bla03] Blanch, J. "Using Kriging to Bound Satellite Ranging Errors Due to the Ionosphere." *PhD Dissertation*. Stanford, CA: Stanford University. (2003).
- [Bos04] Bossert, K. "Reclaiming Kaho'olawe." *Geospatial Solutions*. 14.9 (2004): 24-30.
- [Bro86] "GPS Failure Detection by Autonomous Means Within the Cockpit." *NAVIGATION: Journal of the Institute of Navigation*. 33.4 (1986): 335-353.
- [Bro92] Brown, R. "A Baseline RAIM Scheme and a Note on the Equivalence of Three RAIM Methods." *NAVIGATION: Journal of the Institute of Navigation*. 39.4 (1992): 127-137.
- [Bro96] Brown, R. "Receiver Autonomous Integrity Monitoring." *Global Positioning System: Theory and Applications Volume 2*. Washington, DC: AIAA Progress in Aeronautics and Astronautics Volume 163.(1996): 143-166.

- [Bry02] Bryson, A. E. *Applied Linear Optimal Control*. Cambridge, UK: Cambridge University Press. (2002): 310-312.
- [Bry68] Bryson, A. E., and L. J. Henrikson. "Estimation Using Sampled Data Containing Sequentially Correlated Noise." *AIAA Journal of Spacecraft*. 5.6 (1968): 662-665.
- [Cam06] Campbell, J., M. Miller, M. Uijt de Haag, D. Venable, and M. Smearcheck. "Flash-LADAR Inertial Navigator Aiding." *Proceedings of the IEEE/ION Position Location and Navigation Symposium*. San Diego, CA. (2006): 677-683.
- [Cha08] Chan, F. C. "A State Dynamics Method for Integrated GPS/INS Navigation and Its Application to Aircraft Precision Approach." *PhD Dissertation*. Chicago, IL: Illinois Institute of Technology. (2008).
- [Chr99] Christie, J., P. Ko, A. Hansen, D. Dai, S. Pullen, B. Pervan, and B. Parkinson. "The Effects of Local of Local Ionospheric Decorrelation on LAAS: Theory and Experimental Results." *Proceedings of the Institute of Navigation NTM*. San Diego, CA. (1999).
- [Clo06] Clot, A., C. Macabiau, I. Nikiforov, B. Roturier. "Sequential RAIM Designed to Detect Combined Step Ramp Pseudo-Range Errors." *Proceedings of the Institute of Navigation GNSS Conference*. Fort Worth, TX. (2006): 2621-2633.
- [Coh92] Cohen, C., B. Pervan, and B. Parkinson. "Estimation of Absolute Ionospheric Delay Exclusively through Single-Frequency GPS Measurements." *Proceedings of the Institute of Navigation GPS Conference*. Albuquerque, NM. (1992).
- [Coh95] Cohen, C., S. Cobb, D. Lawrence, B. Pervan, D. Powell, B. Parkinson, G. Aubrey, W. Loewe, D. Ormiston, D. McNally, D. Kaufmann, V. Wullschleger, and R. Swider. "Autoland a 737 Using GPS Integrity Beacons." *NAVIGATION: Journal of the Institute of Navigation*. 42.3 (1995): 467-486.
- [Cra04] Crassidis, J., and J. Junkins. *Optimal Estimation of Dynamic Systems*. Boca Raton, FL: Chapman & Hall/CRC. (2004).
- [Dal05] Dalley, J. "Cutting-Edge Technology: ION's Autonomous Lawn Mower Competition." *GPS World of August 2005*. (2005): 20-21.
- [Dan98] Danchik, R. "An Overview of Transit Development." *John Hopkins APL Technical Digest*. 19.1 (1998): 18-26.
- [Dat02] Datta-Barua, S., T. Walter, S. Pullen, M. Luo, J. Blanch, and P. Enge. "Using WAAS Ionospheric Data to Estimate LAAS Short Baseline Gradients." *Proceedings of the Institute of Navigation NTM*. San Diego, CA. (2002).

- [DeC00] DeCleene, B. "Defining Pseudorange Integrity - Overbounding." *Proceedings of the Institute of Navigation GPS Conference*. Salt Lake City, UT. (2000): 1916-1924.
- [Dis01] Dissanayake, G., P. Newman, S. Clark, H. Durrant-Whyte, and M. Csorba. "A Solution to the Simultaneous Localization and Map Building (SLAM) Problem." *IEEE Transactions on Robotics Automation*. 17.3 (2001): 229-241.
- [FAA02] Federal Aviation Administration. "Category I Local Area Augmentation System Ground Facility." *FAA-E-2937A*. (2002).
- [Far03] Farrell, J. A., H.-S. Tan, and Y. Yang. "Carrier Phase GPS-Aided INS-Based Vehicle Lateral Control." *ASME Journal of Dynamic Systems, Measurements and Control*. 125 (2003): 339-353.
- [Foe99] Foessel, A., S. Chheda, and D. Apsotolopoulos. "Short-Range Millimeter-Wave Radar Perception in a Polar Environment." *Proceedings of the Field and Service Robotics Conference*. (1999).
- [Fos98] Fossa, C., R. Raines, G. Gunsch, and M. Temple. "An Overview of the Iridium Low Earth Orbit (LEO) Satellite System." *Proceedings of the IEEE National Aerospace and Electronics Conference*. (1998): 152-159.
- [Gel74] Gelb, A. (editor). *Applied Optimal Estimation*. Cambridge, MA: The MIT Press. (1974) 102-155.
- [Gra03] Gratton, L. "Orbit Ephemeris Monitors for Category I Local Area Augmentation of GPS." *MS Thesis*. Chicago, IL: Illinois Institute of Technology. (2003).
- [Gra09] Gratton, L., M. Joerger, and B. Pervan. "Carrier Phase Relative RAIM Algorithms and Protection Level Derivation." *Proceedings of the Institute of Navigation International Technical Meeting*. Anaheim, CA. (2009).
- [Gre96] Greenspan, R. *The Global Positioning System: Theory and Applications*. Washington, DC: AIAA Progress in Aeronautics and Astronautics B. W. Parkinson, J. J. Spilker, Jr., P. Axelrad, P. Enge, editors. (1996): 187-218.
- [Gui98] Guier, W., and G. Weiffenbach. "Genesis of Satellite Navigation." *John Hopkins APL Technical Digest*. 19.1 (1998): 14-17.
- [Han00a] Hansen, A., J. Blanch, T. Walter, and P. Enge. "Ionospheric Correlation Analysis for WAAS: Quiet and Stormy." *Proceedings of the Institute of Navigation GPS Conference*. Salt Lake City, UT. (2000).
- [Han00b] Hansen, A., E. Peterson, T. Walter, and P. Enge. "Correlation Structure of Ionospheric Estimation and Correction for WAAS." *Proceedings of the Institute of Navigation NTM*. Anaheim, CA. (2000).

- [Hat94] Hatch, R., and H. J. Euler. "Comparison of Several AROF Techniques." *Proceedings of the Institute of Navigation GPS Conference*. Salt Lake City, UT. (1994): 363-370.
- [Heo04] Heo, M. B. "Robust Carrier Phase DGPS Navigation for Shipboard Landing of Aircraft." *PhD Dissertation*. Chicago, IL: Illinois Institute of Technology. (2004).
- [Hir04] Hirokawa, R., K. Nakakuki, K. Sato, and R. Ishihara. "Threading the Maze, GPS/INS, Landmark Sensing, and Obstacle Avoidance." *GPS World*. 15.11 (2004): 20-26.
- [Hua08] Huang, J., F. van Graas, and C. Cohenour. "Characterization of Tropospheric Spatial Decorrelation Errors Over a 5-km Baseline." *NAVIGATION: Journal of the Institute of Navigation*. 55.1 (2008): 39-53.
- [Hwa91] Hwang, P. "Kinematic GPS for Differential Positioning: Resolving Integer Ambiguities on the Fly." *NAVIGATION: Journal of the Institute of Navigation*. 38.1 (1991): 1-15.
- [Hwa06] Hwang, P., and R. Brown. "RAIM-FDE Revisited: A New Breakthrough In Availability Performance With NIOAIM (Novel Integrity-Optimized RAIM)." *NAVIGATION: Journal of the Institute of Navigation*. 53.1 (2006): 41-52.
- [ICA07] International Civil Aviation Organization (ICAO). "Manual for ICAO Aeronautical Mobile Satellite (Route) Service." *Part 2-Iridium, draft edition available online at <http://www.icao.int/anb/panels/acp/repository.cfm>*. (2007).
- [ICD93] "Interface Control Document (ICD) GPS-200." Revision C, available online at <http://www.navcen.uscg.gov/pubs/gps/icd200/icd200cw1234.pdf>. (1993).
- [Joe04] Joerger, M., J. Christ, R. Duncan, and B. Pervan. "Design of an AGV for Improved CDGPS-based Control Performance." *Proceedings of the Institute of Navigation ION GNSS*. Long Beach, CA. (2004).
- [Joe06a] Joerger, M., J. Christ, R. Duncan, and B. Pervan. "Integrated Design of an AGV for Improved GPS-based Path-Following Performance." *International Journal of Vehicle Design*. 42.3|4 (2006): 263-286.
- [Joe06b] Joerger, M., and B. Pervan. "Autonomous Ground Vehicle Navigation Using Integrated GPS and Laser-scanner Measurements." *Proceedings of the IEEE/ION Position Location and Navigation Symposium*. San Diego, CA. (2006): 988-997.
- [Kha08] Khanafseh, S. "GPS Navigation Algorithms for Autonomous Airborne Refueling of Unmanned Air Vehicles." *PhD Dissertation*. Chicago, IL: Illinois Institute of Technology. (2008).

- [Kid04] Kidder, S., and T. Vonder Haar. "A Satellite Constellation to Observe the Spectral Radiance Shell of Earth." *Proceedings of the Conference on Satellite Meteorology and Oceanography*. (2004): 1-5.
- [Kim04] Kim, J., and S. Sukkarieh. "SLAM aided GPS/INS Navigation in GPS Denied and Unknown Environments." *Proceedings of the 2004 International Symposium on GNSS/GPS*. Sydney, Australia. (2004): 1-5.
- [Klo87] Klobuchar, J. "Ionospheric Time-Delay Algorithm for Single-Frequency GPS Users." *IEEE Transactions on Aerospace Electronic Systems*. 23.3 (1987): 325-331.
- [Kol05] Kolb, P., X. Chen, and U. Vollath. "A New Method to Model the Ionosphere across Local Area Networks." *Proceedings of the Institute of Navigation GNSS Conference*. Long Beach, CA. (2005).
- [Law96] Lawrence, D. "Aircraft Landing Using GPS: Development and Evaluation of a Real Time System for Kinematic Position using the Global Positioning System." *PhD Dissertation*. Stanford, CA: Stanford University. (1996).
- [Lee06a] Lee, J., M. Luo, S. Pullen, Y. S. Park, P. Enge, and M. Brenner. "Position-Domain Geometry Screening to Maximize LAAS Availability in the Presence of Ionosphere Anomalies." *Proceedings of the Institute of Navigation GNSS Conference*. Fort Worth, TX. (2006).
- [Lee06b] Lee, J., S. Pullen, S. Datta-Barua, and P. Enge. "Assessment of Nominal Ionosphere Spatial Decorrelation for GPS-Based Aircraft Landing Systems." *Proceedings of the IEEE/ION Position Location and Navigation Symposium*. San Diego, CA. (2006).
- [Lee07] Lee, Y. C., S. "Two New RAIM Methods Based on the Optimally Weighted Average Solution (OWAS) Concept." *NAVIGATION: Journal of the Institute of Navigation*. 54.4 (2007): 333-345.
- [Leo92] Leonard, J., and H. Durrant-Whyte. *Directed Sonar Sensing for Mobile Robot Navigation*. Cambridge, MA: Kluwer Academic Publishers (1992): 129-138.
- [Leo00] Leonard, J., and H. J. Feder. "A Computationally Efficient Method for Large-Scale Concurrent Mapping and Localization." *Robotics Research: the Ninth International Symposium*. London, United Kingdom: John Hollerbach and Dan Koditschek (Eds), Springer-Verlag. (2000).
- [Mad02] Madhavan, R., H. Durrant-Whyte, and G. Dissanayake. "Natural Landmark-based Autonomous Navigation using Curvature Scale Space." *Proceedings of the IEEE-ICRA*. 4 (2002): 3936-3941.

- [Mak95] Maksarov, D., and H. Durrant-Whyte. "Mobile Vehicle Navigation in Unknown environments: a multiple hypothesis approach." *IEEE Proceedings on Control Theory Applications*. 142.4 (1995): 385-400.
- [MAS04] RTCA Special Committee 159. "Minimum Aviation System Performance Standards for the Local Area Augmentation System (LAAS)." *Document No. RTCA/DO-245*. Washington, DC. (2004).
- [McG00] McGraw, G., T. Murphy, M. Brenner, S. Pullen, and A. Van Dierendonck. "Development of the LAAS Accuracy Models." *Proceedings of the Institute of Navigation GPS Conference*. Salt Lake City, UT. (2000): 1212-1223.
- [Mit06] Mitelman, A., P. L. Normark, M. Reidevall, J. Thor., O. Grönqvist, and L. Magnusson. "The Nordnav Indoor GNSS Reference Receiver." *Proceedings of the Institute of Navigation GNSS Conference*. Fort Worth, TX. (2006): 2494-2502.
- [Mis06] Misra, P., and P. Enge. *Global Positioning System: Signals, Measurements, and Performance, Second Edition*. Lincoln, MA: Ganga-Jamuna Press. (2006).
- [MOP01] RTCA Special Committee 159. "Minimum Operational Performance Standards for Global Positioning System/Wide Area Augmentation System Airborne Equipment." *Document No. RTCA/DO-229C*. Washington, DC. (2001).
- [NST99] NSTB/WAAS T&E Team, William J. Hughes Technical Center. "Global Positioning System (GPS) Standard Positioning Service (SPS) Performance Analysis Report." *available online at <http://www.nstb.tc.faa.gov/DisplayArchive.htm>*. Atlantic City, NJ: Reports No. 26-62. (1999-2008).
- [NST03] NSTB/WAAS T&E Team, William J. Hughes Technical Center. "Wide-Area Augmentation System Performance Analysis Report." *available online at <http://www.nstb.tc.faa.gov/DisplayArchive.htm>*. Atlantic City, NJ: Reports No. 5-23. (2003-2008).
- [OCo97] O'Connor, M. "Carrier-Phase Differential GPS for Automatic Control of Land Vehicles." *PhD Dissertation*. Stanford, CA: Stanford University. (1997).
- [Oly02] Olynik, M., M. G. Petovello, M. E. Cannon, and G. Lachapelle. "Temporal Variability of GPS Error Sources and Their Effect on Relative Positioning Accuracy." *Proceedings of the Institute of Navigation NTM 2002*. San Diego, CA. (2002).
- [Ops00] Opshaug, G., and P. Enge. "Robotic Snow Cat." *Proceedings of the Institute of Navigation ION GPS 2000*. Salt Lake City, UT. (2000): 1016-1023.
- [Pai93] Paielli, R., B. D. McNally, R. Bach, and D. N. Warner. "Carrier Phase Differential GPS for Approach and Landing: Algorithms and Preliminary

- Results.” *Proceedings of the Institute of Navigation GPS Conference*. Salt Lake City, UT. (1993).
- [Par96] Parkinson, B., and J. Spilker. *Global Positioning System: Theory and Applications Volume 1*. Washington, DC: AIAA Progress in Aeronautics and Astronautics Volume 163. (1996).
- [Per96] Pervan, B. “Navigation Integrity for Aircraft Precision Landing Using the Global Positioning System.” *PhD Dissertation*. Stanford, CA: Stanford University. (1996).
- [Per97] Pervan, B., and B. Parkinson. “Cycle Ambiguity Estimation for Aircraft Precision Landing Using the Global Positioning System.” *AIAA Journal of Guidance, Controls, and Dynamics*. 20.4 (1997): 681-689.
- [Per03] Pervan, B., F. C. Chan, D. Gebre-Egziabher, S. Pullen, P. Enge, and G. Colby. “Performance Analysis of Carrier-Phase DGPS Navigation for Shipboard Landing of Aircraft.” *NAVIGATION: Journal of the Institute of Navigation*. 50.3 (2003): 181-191.
- [Pul04] Pullen, S., and P. Enge. “Satellite Integrity Monitoring Concepts for GPS/Galileo Augmentation Systems.” *Proceedings of the Institute of Navigation GNSS Conference*. Long Beach, CA. (2004): 1674-1682.
- [Rab98] Rabinowitz, M., B. Parkinson, C. Cohen, M. O’Connor, and D. Lawrence. “A System Using LEO Telecommunication Satellites for Rapid Acquisition of Integer Cycle Ambiguities.” *Proceedings of ION/IEEE Position Location and Navigation Symposium*. Palm Springs, CA. (1998): 137-145.
- [Rab00] Rabinowitz, M. “A Differential Carrier-Phase Navigation System Combining GPS with Low Earth Orbit Satellites for Rapid Resolution of Integer Cycle Ambiguities.” *PhD Dissertation*. Stanford, CA: Stanford University. (2000).
- [Rem90] Remondi B. “Pseudo-Kinematic GPS Results Using the Ambiguity Function Method.” *Proceedings of the 46th Annual Meeting of the Institute of Navigation*. Atlantic City, NJ. (1990): 41-49.
- [Rem93] Remondi B. “On-The-Fly Kinematic GPS Results Using Full-Wavelength Dual-Frequency Carrier Ranges.” *Proceedings of the 49th Annual Meeting of the Institute of Navigation*. Cambridge, MA. (1993): 505-518.
- [SIC06] SICK AG (laser scanner manufacturer) “LMS200/211/221/291 Laser Measurement Systems.” *Technical Description*. 8008970/Q172/2006-12 (2006).
- [Sol07] Soloviev, A., D. Bates, and F. van Graas. “Tight Coupling of Laser Scanner and Inertial Measurements for a Fully Autonomous Relative Navigation

- Solution.” *NAVIGATION: Journal of the Institute of Navigation*. 54.3 (2007): 189-205.
- [SPS01] Assistant Secretary of Defense for Command, Control, Communications and Intelligence. “Global Positioning System Standard Positioning Service Performance Standard.” *available online at <http://www.navcen.uscg.gov/GPS/geninfo/2001SPSPerformanceStandardFINAL.pdf>*. Washington, DC. (2001).
- [Stu88] Sturza, M. “Navigation System Integrity Monitoring Using Redundant Measurements.” *NAVIGATION: Journal of the Institute of Navigation*. 35.4 (1988): 69-87.
- [Tan04] Tang, F., M. Adams, J. Ibanez-Guzman, and W. Wijesoma. “Pose Invariant, Robust Feature extraction From Range Data With a Modified Scale Space Approach.” *Proceedings of the IEEE-ICRA*. 3.26 (2004): 3173-3179.
- [Ten01] Tena Ruiz, I., Y. Petillot, D. M. Lane, and C. Salson. “Feature Extraction and Data Association for AUV Concurrent Mapping and Localization.” *Proceedings of the IEEE-ICRA*. 3 (2001): 2785-2790.
- [Teu98] Teunissen, P., D. Odijk, and P. Joosten. “A Probabilistic Evaluation of Correct GPS Ambiguity Resolution.” *Proceedings of the 11th International Technical Meeting of the Satellite Division of the Institute of Navigation*. Nashville, TN. (1998).
- [Thr03] Thrun, S. “Robotic Mapping: A Survey.” *Exploring Artificial Intelligence in the New Millenium*. San Fransisco, CA: Morgan Kaufmann Publishers Inc. (2003): 1-35.
- [Thr06] Thrun, S., M. Montemerlo, H. Dahlkamp, D. Stavens, A. Aron, J. Diebel, P. Fong, J. Gale, M. Halpenny, G. Hoffmann, K. Lau, C. Oakley, M. Palatucci, V. Pratt, P. Stang, S. Strohband, C. Dupont, L. E. Jendrossek, C. Koelen, C. Markey, C. Rummel, J. van Niekerk, E. Jensen, P. Alessandrini, G. Bradski, B. Davies, S. Ettinger, A. Kaehler, and A. Nefian. “Stanley: The Robot that Won the DARPA Grand Challenge.” *Journal of Field Robotics*. London, United Kingdom: Wiley Periodicals, Inc. 23.9 (2006): 661-692.
- [VDi05] Van Dierendonck, A. J. “GNSS User Assessment of the Plans and the Benefits of GNSS Modernized Signals and Services.” *Proceedings of the Institute of Navigation 61st Annual Meeting*. Cambridge, MA. (2005): 201-209.
- [vGr93] van Graas, F., D. Diggle, and R. Hueschen. “Interferometric GPS Flight Reference/Autoland System.” *Proceedings of the 6th International Technical Meeting of the Institute of Navigation*. Salt Lake City, UT. (1993): 855-877.
- [vGr04] van Graas, F., B. Pervan, L. O’Rear, J. Morton, M. Miller, and J. Raquet. “Just Keep Rolling a Lawn.” *GPS World of September 2004*. (2004): 14-20.

- [vGr07] van Graas, F. *personal communication*. (2007).
- [Wal95] Walter, T., and P. Enge. "Weighted RAIM for Precision Approach." *Proceedings of the Institute of Navigation GPS Conference*. Palm Springs, CA. (1995).
- [Wal00] Walter, T., A. Hansen, J. Blanch, P. Enge, T. Mannucci, X. Pi, L. Sparks, B. Iijima, B. El-Arini, R. Lejeune, M. Hagen, E. Altshuler, R. Fries, and A. Chu. "Robust Detection of Ionospheric Irregularities." *Proceedings of the Institute of Navigation GPS Conference*. Salt Lake City, UT. (2000).
- [War03] Warren, D., and J. Raquet. "Broadcast vs. Precise GPS Ephemerides: a Historical Perspective." *GPS Solutions*. Springer Berlin / Heidelberg. 7.3 (2003): 151-156.
- [Woo99] Woo, K. T. "Optimum Semi-Codeless Carrier Phase Tracking of L2." *Proceedings of the 12th International Technical Meeting of the Institute of Navigation*. Nashville, TN. (1999).
- [Ye02] Ye, C., and J. Borenstein. "Characterization of a 2-D Laser Scanner for Mobile Robot Obstacle Negotiation." *Proceedings of the IEEE-ICRA*. (2002): 2512-2418.
- [Yio98] Yionoulis, S. "The Transit Satellite Geodesy Program." *John Hopkins APL Technical Digest*. 19.1 (1998): 36-42.